

BROADBAND BEAMFORMING AND DIRECTION FINDING
USING CONCENTRIC RING ARRAY

A Dissertation
presented to
the Faculty of the Graduate School
University of Missouri-Columbia

In Partial Fulfillment
of the Requirements for the Degree
Doctor of Philosophy

by
Yunhong Li
Dr. Dominic K. C. Ho, Dissertation Supervisor
July 2005

The undersigned, appointed by the Dean of the Graduate School, have examined the dissertation entitled

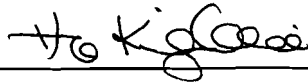
BROADBAND BEAMFORMING AND DIRECTION FINDING
USING CONCENTRIC RING ARRAY

Presented by Yunhong Li

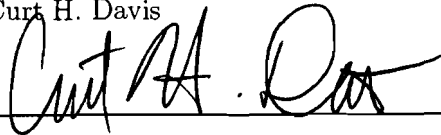
A candidate for the degree of Doctor of Philosophy

And hereby certify that in their opinion it is worthy of acceptance.

Dr. Dominic K. C. Ho



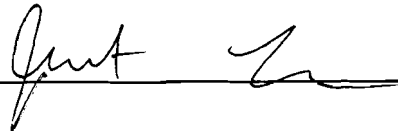
Dr. Curt H. Davis



Dr. Chengshan Xiao



Dr. Justin Legarsky



Dr. Yunxin Zhao



To my parents

and to

my wife.

ACKNOWLEDGMENTS

I would like to sincerely thank my advisor, Dr. Dominic K. C. Ho, for his intellectual guidance and generous encouragement. I would also like to express my gratitude to Dr. Curt Davis, Dr. Chengshan Xiao, Dr. Justin Legarsky, and Yunxin Zhao for their time and consideration in reading my dissertation, and for their help in defining and completing my research.

I would like to thank students and colleagues in the Signal Processing and Communications Lab, La-or Kovavisaruch, Xiaoning Lu, San-Yick Leong, Min Wu, Jingxian Wu and Yahong Zheng, for their kind help both in my research and daily life.

Finally, I would like to thank my family for all their love and support.

ABSTRACT

Sensor arrays have been used widely in applications including radar, sonar, seismology, biomedicine, communications, geophysical exploration, astronomy, and imaging. A very popular type of sensor array is circular array. It has several advantages such as the fact that it can perform 360° scan around its center very conveniently and during the scan the array pattern can be kept almost invariant. In our research, we consider beamformer design and DOA estimation for a wideband source using concentric ring array(CRA) that contains many concentric rings of different radii. Such structure yields several advantages including the flexibility in array pattern synthesis and adaptive array design. Previous works on controlling the array pattern of CRA only address narrowband scenario. The research on CRA conducted here is aimed for broadband beamforming applications.

The design of deterministic broadband beamformer, adaptive broadband beamformer and broadband direction of arrival(DOA) estimation using CRA are addressed in this research. The proposed deterministic as well as adaptive broadband beamformer designs use the novel idea of decomposing the weights of the array into two sets: inter-ring weights and intra-ring weights, and they are chosen separately using different criteria. The deterministic broadband beamformer design is based on the sidelobe level control method proposed by Stearns and Stewart for 2-D narrowband beamforming using continuous ring antennas. We propose three methods to design inter-ring weights to achieve desirable sidelobe and/or mainlobe in the array pattern at a range of frequencies. Method I uses an interpolation technique to derive the inter-ring weights at a range of frequencies that can yield the desired sidelobe level. Method II uses MMSE optimization to find the inter-ring weights that can reduce the pattern synthesis error when array elements are not enough. Method III improves on previous methods by selecting appropriate desirable prototype array pattern at different frequencies to achieve

frequency invariant array pattern. The proposed deterministic beamformer designs are suitable for broadband beamformer implemented in the frequency domain.

In the development of the adaptive CRA, we propose an element space partially adaptive CRA that accommodates arbitrary partition schemes. We then derive the analytical form of the steady state residual interference and noise power and use it as an evaluation criterion for different partition structures. Simulation have verified the advantages of the proposed design.

Finally, based on Lee's work [1] we propose a broadband DOA estimator for CRA, which significantly improves the estimation accuracy and greatly reduces computational complexity comparing to conventional incoherent broadband DOA estimators. The advantages of the proposed DOA estimator is corroborated by simulations.

TABLE OF CONTENTS

ACKNOWLEDGMENTS	ii
ABSTRACT	iii
LIST OF TABLES	x
LIST OF FIGURES	xi
1 Introduction	1
1.1 Background and Motivation	1
1.2 Previous Works on Circular Array Beampattern Synthesis	3
1.2.1 Array Pattern Synthesis Using Circular Array	3
1.2.2 Field Synthesis Method	4
1.2.3 Minimax Method	5
1.2.4 Transform Domain Method	7
1.2.5 Space-time Method	8
1.2.6 Other Array Pattern Synthesis Techniques	8
1.3 Main Contributions of the Research	9
1.4 Content Organization	10
2 Introduction to Beamforming	11
2.1 Array Processing Basics	11
2.1.1 Coordinate System	11
2.1.2 Signals in Space and Time	13
2.1.3 Array Processing Signal Model	14

2.1.4	Near-field and Far-field Assumption	15
2.2	Beamforming Techniques	16
2.2.1	Conventional Beamforming Techniques	17
2.2.2	Modern Beamforming Techniques	20
2.3	Array with Different Geometry	23
2.3.1	1-D Array	23
2.3.2	2-D Array	25
2.3.3	3-D Array	26
2.4	Circular Array	26
2.5	Summary	28
3	Deterministic Beamforming Using Concentric Ring Array	30
3.1	Beamforming Using CRA	31
3.1.1	CRA Structure	31
3.1.2	Design of the CRA Weights	32
3.2	Stearns and Stewart's Method	34
3.3	Proposed 3-D Array Pattern Synthesis Method	35
3.3.1	Requirement on Number of Array Elements	38
3.4	Proposed Inter-ring Weights Design Methods	40
3.4.1	Method I: Inter-ring Weights Interpolation	40
3.4.2	Method II: Inter-ring Weights Design Using MMSE Criterion	44
3.4.3	Method III: Inter-ring Weights Design with Frequency Invariant Property	48
3.4.4	Comparison of Method I, II, III	52
3.5	Broadband Beamforming Implementation	52
3.5.1	Frequency Domain Broadband Beamformer	52
3.5.2	Nested Array Design	54

3.5.3	Linear Constrained Beamformer with Desired Beampattern	54
3.6	Experimental Results	57
3.6.1	Method I	57
3.6.2	Method II	62
3.6.3	Method III	64
3.7	Summary	67
4	Design of Adaptive Concentric Ring Array	70
4.1	Fully Adaptive CRA	71
4.1.1	Adaptive Approaches	73
4.1.2	Broadband Adaptive Beamforming	76
4.1.3	Summary on Fully Adaptive CRA	77
4.2	Partially Adaptive CRA	77
4.2.1	Introduction to Partially Adaptive Array Design	77
4.2.2	Proposed Partially Adaptive CRA	79
4.2.3	Adaptive Algorithms	82
4.2.4	Comparison Between the Fully and Partially Adaptive CRA	84
4.3	Analysis of Partially Adaptive CRA	85
4.3.1	Convergence Rate	86
4.3.2	Steady State Performance	86
4.4	Experimental Results	87
4.4.1	Adaptation Performance	89
4.4.2	Comparison of Partitioning Schemes	91
4.4.3	Broadband Beamforming	92
4.5	Summary	94
5	DOA Estimation Using Concentric Ring Array	95
5.1	Introduction to DOA Estimation	96

5.1.1	Narrowband DOA Estimation	96
5.1.2	Broadband DOA Estimation	97
5.1.3	DOA Estimation Using Circular Arrays	97
5.2	Proposed Broadband DOA Estimation Method Using CRA	98
5.2.1	Signal Model	99
5.2.2	Focusing Matrices Design Using Frequency Invariant CRA	101
5.3	Statistical Performance Analysis	105
5.3.1	Cramer-Rao Lower Bound Analysis	106
5.4	Experimental Results	108
5.4.1	Narrowband Beamspace	108
5.4.2	Proposed Broadband Beamspace Method	109
5.4.3	Correlated Sources	112
5.5	Summary	112
6	Application of Concentric Ring Array in Bird Monitoring	115
6.1	Overall System Description	116
6.2	Experimental Results	117
6.2.1	Array Configuration	117
6.2.2	Simulation Results	118
6.2.3	Field Data Testing Results	120
6.3	Summary	121
7	Conclusion and Future Work	126
7.1	Completed Research	126
7.1.1	Deterministic CRA Design	126
7.1.2	Adaptive CRA Design	128
7.1.3	Broadband DOA Estimation	129
7.1.4	Bird Monitoring Application	130

7.2 Future Work	130
Bibliography	131
VITA	147

LIST OF TABLES

Table	Page
4.1	Number of required complex multiplications. 85
4.2	Interference and noise power at some iteration numbers. 90
4.3	Steady state residual interference and noise power. 92
4.4	Configuration of CRA in the nested array design. 92
4.5	Desired signal and interferences. 93
6.1	Radii of each ring and array elements distribution. 118
6.2	Grouping of subarrays and their configuration, numbers in round bracket indicates the array elements are shared with other subarrays. 118
6.3	Classification results before beamforming. 121
6.4	Classification results after beamforming. 121

LIST OF FIGURES

Figure	Page
2.1 The Cartesian and spherical coordinate systems.	12
2.2 (a) Near-Field and (b) Far-Field scenarios.	15
2.3 The beampattern of a linear array. The linear array consists of 15 equally spaced array elements, spacing between adjacent elements is half of the wavelength.	17
2.4 The delay-and-sum beamformer.	18
2.5 The beampattern of a tapered linear array. The value of the tapers are generated using a $-20db$ Chebyshev function. The linear array has the same configuration as in Fig. 2.3	19
2.6 The beampattern of an optimum linear array. The linear array has the same configuration as in Fig. 2.3	21
2.7 General sidelobe canceller.	22
2.8 Uniform linear array.	24
2.9 The ambiguity DOAs of a linear array	24
2.10 2-D arrays. (a) cross array (b) rectangular array (c) L-shape array (d) right triangle array (e) octagon array (f) circular array.	25
2.11 Bessel functions $J_0(s)$, $s \in [-20, 20]$	29
3.1 Geometry of a CRA.	31
3.2 Interpolation of $(R_m/\lambda, B_m)$, $m = 1, \dots, 5$	36
3.3 Mapping between (ϕ, θ) and φ , φ is represented by z -axis. The look direction is $(\phi_0 = 90^\circ, \theta = 45^\circ)$	38

3.4	Bessel functions: $J_0(s)$ (solid line), $J_4(s)$ (dashed line) and $J_8(s)$ (dotted line).	39
3.5	Interpolation curve of $(\delta_m/(4\pi), B_m)$, $m = 1, \dots, 15$, obtained by using a $-30dB$ sidelobe level Chebyshev function as the desired array pattern.	41
3.6	Relationship between P and (f/f_0) for $M = 4, 6, 8, 10$	43
3.7	Beampattern of a discrete ring: array pattern generated using only J_0 term (solid line), actual array pattern (dashed line).	45
3.8	Array pattern $F_{f_0}(\phi, \theta)$ and $F_F(\phi, \theta)$, where $\varphi = \rho/2$. a and b denote the first zero crossing points of $F_{f_0}(\phi, \theta)$ and $F_F(\phi, \theta)$ respectively, $b = af_0/f$	50
3.9	Frequency domain broadband beamformer based on FFT.	53
3.10	CRA using nested array structure. $R_m, m = 1, \dots, 6$ normalized with respect to R_1 is: $[1 \ 2 \ 3 \ 4 \ 6 \ 8]$	55
3.11	2-D Beampatterns in the 2nd subarray: curves starting from the outside one are beampatterns at frequencies: $600Hz$, $800Hz$, $1000Hz$, $1200Hz$, $1400Hz$ and $1600Hz$ respectively. The main look direction in this 2-D array pattern is $\phi = 45^\circ$	58
3.12	3D Beampattern at $1600Hz$ in the 2nd subarray, the main look direction is $(\phi_0 = 45^\circ, \theta_0 = 60^\circ)$	59
3.13	Processing results for scenario 1: (a) Desired signal $s(t)$; (b) Received noisy signal in one channel; (c) Beamformer output $z_1(t)$; (d) Error signal: $e_1(t) = z_1(t) - s(t)$	60
3.14	Processing results for scenario 2: (a) Desired signal $s(t)$; (b) Received noisy signal in one channel; (c) Beamformer output $z_2(t)$; (d) Error signal: $e_2(t) = z_2(t) - s(t)$	61
3.15	2-D array pattern obtained at $700Hz$	62

3.16	Processing results for scenario 3: (a) Desired signal $s(t)$; (b) Received noisy signal in one channel; (c) Beamformer output $z_3(t)$; (d) Error signal: $e_3(t) = z_3(t) - s(t)$	63
3.17	The Desired and synthesized array pattern: Desired (dashed line), synthesized (solid line). The main look direction is $\phi = 45^\circ$	64
3.18	Method I (dashed line) vs. Method II (solid line). The main look direction is $\phi = 45^\circ$	65
3.19	3D array pattern at $2000Hz$, the look direction is $(45^\circ, 45^\circ)$	66
3.20	3-D view of 2-D beampatterns from $900Hz$ to $2000Hz$, sampled at every $100Hz$	67
3.21	Overlapped beampatterns from $900Hz$ to $2000Hz$, sampled at every $100Hz$	68
3.22	The relative MSE from $600Hz$ to $2000Hz$	69
4.1	General sidelobe canceller.	72
4.2	General sidelobe canceller.	82
4.3	Partition schemes of partially adaptive arrays: Type 1 (a), Type 2 (b), Type 3 (c) and Type 4 (d). Only two adjacent rings are shown, where the array elements in the same subarray are represented by the same symbols.	88
4.4	Interference and noise power in array outputs. Vertical axis: Normalized interference and noise power in dB, horizontal axis: number of iterations.	90
4.5	Processing results. (a) Desired signal. (b)-(f) Residual interference and noise in fully adaptive array and Type 1-4 partially adaptive array.	94
5.1	Configuration of a CRA.	99
5.2	Narrowband beamspace estimator: RMSEs in degrees vs. SNR.	109
5.3	Coherent broadband estimator: RMSEs in degrees vs. SNR.	110
5.4	Incoherent broadband estimator: RMSEs in degrees vs. SNR.	111
5.5	Narrowband estimator: MUSIC spectrum of two correlated sources.	113

5.6	Proposed coherent broadband estimator: MUSIC spectrum of two correlated sources.	114
6.1	Proposed automated bird monitoring and recognition system.	116
6.2	Spectrum of some bird species. Spectrum computed using 256 point FFT.	117
6.3	2-D Beampatterns in the 2nd subarray: curves starting from the outside one are beampatterns at frequencies: $900Hz$, $1100Hz$, $1300Hz$, $1500Hz$ and $1700Hz$ respectively. The main look direction in this 2-D beampattern is $\theta = 45^\circ$	119
6.4	Processing results for scenario 1: (a) Desired signal $s(t)$; (b) Received noisy signal in one channel; (c) Beamformer output $z_1(t)$; (d) Error signal: $e_1(t) = z_1(t) - s(t)$	123
6.5	Processing results for scenario 2: (a) Desired signal $s(t)$; (b) Received noisy signal in one channel; (c) Beamformer output $z_1(t)$; (d) Error signal: $e_1(t) = z_1(t) - s(t)$	123
6.6	Implemented microphone array.	124
6.7	Processing results for the first set of field data: (a) Received noisy signal in one channel; (b) Beamformer output. Horizontal axis represents the number of samples.	125
6.8	Processing results for the second set of field data: (a) Received noisy signal in one channel; (b) Beamformer output. Horizontal axis represents the number of samples.	125

Chapter 1

Introduction

1.1 Background and Motivation

Signal parameter estimation problem is important in many applications, thus it has received great research interest. The signal of interest is first picked up by one or more sensors. However, the received signal of interest is almost always contaminated by other propagating signals and noise that coexist in the space. In many cases, the signal of interest is too weak among other signals so that solely temporal processing is unable to yield satisfactory estimation results and additional processing gain needs to be sought from spatial processing. Moreover, with the rise of new applications, parameter estimation is no longer limited to temporal parameters. Estimation of spatial parameters becomes necessary in many application such as source localization and source tracking etc. Traditional methods based on temporal processing of the signal received in a single sensor are incapable to estimate those spatial parameters.

Sensors with continuous aperture, such as parabolic dish used in radar system, have directional characteristics. Thus they can be used to extract temporal as well as spatial parameters of a signal. However, such sensors have several drawbacks [2]. First, the directivity pattern is determined by the physical structure of the sensor. The antenna has to be physically rotated to steer to a new direction. Second, the aperture of such

sensor is usually designed to enhance signal in one particular direction. Thus it is unable to track multiple signals at the same time. Third, the operating frequency and bandwidth of such sensor are also fixed by its aperture. Physical adjustments are needed to receive signals in other frequency range.

Comparing with the single sensor, sensor array has all the advantages of spatial processing while without the drawbacks of those single sensors with continuous aperture. Sensor array spatially samples the signal and uses the collected spatial information to enhance signals in certain directions while attenuating the others. The directivity pattern of sensor array can be adjusted by modifying array processing algorithm and tracking of multiple signals simultaneously can be easily programmed in the algorithm.

Sensor arrays are found in a wide range of applications, including radar [3–5], sonar [6, 7], seismology [8, 9], biomedicine [10–12], communications [13, 14], geophysical exploration [15], astronomy [16, 17], and imaging [18–20]. The design of a sensor array mainly includes two aspects, i.e., the hardware design and software design. The hardware design usually refers to deciding an array’s geometry, size, number of sensors and other physical characteristics of the array. The software algorithms typically perform source localization, source tracking, signal detection, signal enhancement and other parameter estimation tasks. Generally speaking, the design process is largely determined by the particular application and the software algorithms may need to be optimized towards the hardware structure.

Among various sensor arrays, a very popular type is the circular array, which is being used in many applications [21–26]. Circular array can be implemented in symmetric form that brings several advantages, such as performing 360° scan around its center by simply adjusting the weights of the array and the beam pattern can be kept almost invariant during the scan. However, the design of circular array is difficult in that the array geometry is non-linear and many conventional array design methods developed for

linear array cannot be applied to a circular array to control its gain in different directions. In our research, we are particularly interested in sensor array that has several concentric circular rings. The reason we prefer such array geometry is that by using the inherent concentric ring structure, the array's gain in different directions can be effectively controlled. It also yields flexibility in developing adaptive processing algorithms. Circular array is also favored in direction finding applications since it provides almost invariant azimuth angle coverage. These advantages and the methodologies to achieve them are the topics of this dissertation, and they will be described in details in the following chapters. Here we first present a review of the previous works on the circular arrays.

1.2 Previous Works on Circular Array Beampattern Synthesis

1.2.1 Array Pattern Synthesis Using Circular Array

The research in circular array dates back to early the last century. H. Stenzel [27] made early theoretical investigations of circular array in 1920s. During 1950s, more theoretical studies on circular array were made by LePage [28], DuHamel [29], Knudsen [30], Wait and Householder [31], and Neff and Tillman [32]. The review of those early works is omitted here because of limited space. In the following we will review some more recent research works related to circular array beampattern synthesis and beamforming methods. Review of the direction finding techniques using circular arrays can be found in Chapter 5.

The circular array beampattern synthesis methods can be categorized as (1) Field

synthesis method; (2) Minimax method; (3) Transform domain method and (4) Space-time method and (5) Other methods. We will review the previous works by their categories.

1.2.2 Field Synthesis Method

The beampattern of the circular array can be expressed in terms of Bessel functions, as will be discussed in detail in Chapter 2. Field synthesis method emerges based on the knowledge that the beampattern can be expressed in an explicit mathematical form and thus analytical solution can be developed.

Stearns and Stewart [33] discuss the application of several concentric circular ring antennas to reduce the sidelobe level of the beampattern. In their method, the beampattern of the whole array is formed as a weighted sum of the beampattern from each ring. The weights for the beampatterns from different rings are then optimized through Fourier-Bessel series expansion so that a desirable sidelobe level can be achieved. In [34], Goto and Cheng also consider the beampattern synthesis using concentric ring array. Their method is different from Stearns and Stewart's method in that the weights for the beampattern from each ring are selected according to a Taylor distribution for circular aperture antennas [35]. Desirable sidelobe can be achieved using their method with the requirement that the inter-ring spacing must be less than a quarter of the wavelength of the operating frequency.

In [36], Vu adopts a different field-synthesis technique to achieve low sidelobes in a circular ring array. When the main look direction of the circular array is vertical to the plane where the array resides in, the beampattern of the circular array can be expressed as an n -th order Bessel function of the first kind, where the order n can be an arbitrary non-negative integer by choosing appropriate weights of the array elements. Vu noticed that an appropriate linear combination of the zero and second order Bessel functions can result in a pattern with small sidelobes. Thus by generating the beampatterns

corresponding to the zero and second order Bessel functions and combining them in phase, low sidelobe level can be achieved. However, this method requires the ring array to have composite array elements that can generate outputs with different phases, which may not be achievable in some applications. Moreover, its application is limited by the requirement that the main look direction must be vertical to the plane of the array.

In [37], Chu investigated the relationship between the number of array elements on a circular ring array and the variation in the azimuthal pattern as the radius of the circular array varies. The purpose is to develop the condition under which a good omnidirectional pattern can be obtained. Sinnott and Harrington [38] use matrix method to analyze and design the circular antenna arrays which can achieve economies of computation by exploiting the array symmetries. Several works [39, 40] look at pattern synthesis problem of circular arrays with directive elements. Other related research works under this category can be found in [41–47].

1.2.3 Minimax Method

The minimax method seeks to find the optimum array weights that minimize the difference between the actual and the desired beam pattern. Different from the field synthesis method, the minimax method obtains the solution by some numerical searching algorithm, and the optimum weights are usually determined iteratively.

Goto and Tsunoda [48] use an optimization technique for uniformly excited arrays requiring only phase adjustments [49] to reduce the sidelobe level of a circular array. The optimization problem can be described as finding a set of phases that maximizes the gain at a main look direction while keeping the gains at sidelobes below a chosen constant. The optimization problem is non-linear. By using a perturbation procedure, Goto and Tsunoda reduce the nonlinear optimization problem to a linear one. They then use iterative method and linear programming to find the solution. The resulting beam pattern has equal-ripple sidelobes similar to a Chebyshev pattern. Watanabe *et*

al. [50,51] extended Goto and Tsunoda's work to take into account the mutual coupling between the array elements and the current distribution of each element. A drawback of their methods is that there is no guarantee that the method can achieve a low sidelobe level. Notice that to avoid high computational complexity, only a limited number of sidelobe locations can be constrained to have a low gain. Thus it's possible that after some iterations, the sidelobes are still high and appear at different locations. Another similar work presented by Coleman [52] also reduces the sidelobe level of the beam pattern using iterative technique.

Prasad and Charan [53] consider the constrained synthesis of beam patterns with applications to circular and arc arrays. Their method is to find the optimum weights that minimize the mean square error between the synthesized and the desired beam pattern. By solving the optimization problem using least-squares method, linear constraints can be specified in the optimization process. However, the least squares solution may yield several high sidelobes. Thus, they use a perturbation and search algorithm to minimize the maximum sidelobe value through iterations. The resulting beam pattern has almost equal sidelobe level and nulls can be formed through linear constraints.

Vescovo [54] approaches the pattern synthesis problem in a way similar to Prasad and Charan's method. In Vescovo's method, the weights are determined by minimizing the mean square distance between the synthesized and the desired beam pattern. Vescovo first examines the unconstrained optimization problem and obtains a closed form solution. He then considers the case where each weight is constrained to belong to a prescribed set of complex numbers. An iterative technique is then proposed to solve the constrained optimization problem. It's shown that if the constraint sets are closed and convex, the weights obtained through the iterations will converge to yield the global minimum of the mean square distance. When the constraint sets are non-convex, a good approximation of the globally optimum solution can be obtained. Vescovo also considers pattern synthesis for near-field beamforming in [55] using similar technique.

In [56], Kumar and Branner propose a design of low sidelobe concentric ring array (CRA) by element radius optimization. They notice that the peak sidelobe level of the designed array is a function of the space between adjacent rings. An iterative technique is used to find the optimum radii for the concentric rings so that the sidelobe level can be reduced.

1.2.4 Transform Domain Method

The transform domain method emerges only recently. Generally speaking, the transform domain method pre-processes the array data by transforming them to other domain to gain some advantages that are not available in conventional methods.

In [57], Lau and Leung proposed an innovate method to synthesize the beam pattern of circular array. Their method employs a transformation technique that is first proposed by Davies [58]. Using the technique, the array element space is transformed to a mode space, in which the array response vector has the Vandermonde form similar to that of a Uniform Linear Array (ULA). The Dolph-Chebyshev method for ULA can then be applied in the mode space to design the beam pattern of the circular array. The resulting beam pattern can reach a desired sidelobe level. Although the desired Chebyshev pattern yields the narrowest mainlobe width at a given sidelobe level, the actual beam pattern obtained using their proposed method may not achieve the desired narrowest mainlobe. This is because during the transformation to the mode space, approximation is involved and the accuracy of the approximation is dependent on the array configuration and the beamforming scenario.

Chan and Pun [59] proposed a method to design broadband circular array with frequency invariant beam pattern. Their basic idea is to transform the received array data to the phase mode by an Inverse Discrete Fourier Transform (IDFT). The frequency dependency of the phase modes is then removed by digital filtering. Finally, a set of weights is chosen to linearly combine the processed phase modes to obtain the desired

frequency invariant beampatterns. Conventional one dimensional beampattern synthesis method can be used to choose the weights. The resulting beampattern can have desired sidelobe level and the mainlobe width is approximately frequency invariant. An extension of the method to concentric circular rings is reported in [60].

1.2.5 Space-time Method

Space-time method is carried out by simultaneously performing two-dimensional filtering on array signal, i.e., the spatial and time domain processing. The array signal contains not only spatially sampled signal but also temporally sampled signal obtained at time delay taps following each array element. The advantage is that by adding the time domain processing, the beamformer can have a certain operating frequency range and thus it is no longer restricted to narrowband beamforming.

In [61], Sarkar and Adve propose a method to perform space-time adaptive processing using circular arrays. In their method, a direct data-domain least-squares space-time adaptive-processing approach is adopted to enhance signals in a non-homogeneous environment of jammers, clutter, and thermal noise. However, their method involves high computational complexity. This is because the number of time-delay taps in each array element is large (several hundreds) and consequently the number of adaptive weights is large. Some other space-time processing techniques for circular array can be found in [62–66].

1.2.6 Other Array Pattern Synthesis Techniques

Several works on the null-control for circular array [67–71] are available. The methods used in those works are extensions of some of the methods above, so they will not be described here. As will be pointed out in Section 3.5.3 of Chapter 3, there is a unified method to perform null control in the beampattern design.

1.3 Main Contributions of the Research

From the preceding review of pattern synthesis and beamforming techniques for circular array, it can be seen that most of the methods are only suitable for narrowband beamforming. Space-time methods has the ability to process signal with certain band-width, however, its computational complexity is high. In our research we are more interested in developing a pattern synthesis method, which generally has much lower computational complexity comparing to the space-time methods. Among the previously reviewed pattern synthesis methods, Chan and Pun's method [59] is developed for broadband beamforming. Different from Chan and Pun's approach which uses only a single ring array, our research of broadband beamforming employs an array structure that consists of many concentric circular rings. The multiple ring structure has the following advantages over a single ring array: 1) It is suitable for nested array design, which can greatly expand the operating frequency range whilst keeping an efficient use of array elements, 2) It increases the flexibility in array design especially in adaptive beamforming as will be shown Chapter 4. Chan and Chen have extended their method to multiple circular arrays in a recent work [60]. However, the design we present in this dissertation takes a different approach from theirs and has its own merit. The contribution of the research presented in this dissertation includes three aspects: 1) The design of a deterministic broadband beamformer using CRA, 2) The development of the partially adaptive CRA, and 3) A broadband angle of arrival(DOA) estimator for CRA.

The proposed deterministic broadband beamformer design is based on Stearns and Stewart's work [33] that considers 2-D narrowband beamforming derived for continuous concentric ring antennas. We first decompose the CRA's weights into inter-ring and intra-ring weights and then propose three methods to design inter-ring weights to achieve desirable sidelobe and/or mainlobe in the array pattern at a range of frequencies. The proposed design is suitable for broadband beamforming in 3-D space.

Secondly, we develop the adaptive form of the CRA. Adaptive beamforming is necessary if the incoming signals are non-stationary. The CRA usually consists of a large number of array elements, which can result in high computational complexity and slow convergence rate in the adaptive algorithm. Partially adaptive array can effectively reduce computation and increase the convergence rate. Therefore we propose a generalized partially adaptive CRA that accommodates arbitrary partitioning schemes. Two typical adaptive algorithms for the proposed design have been derived. Analysis of partially adaptive CRA's steady state performance and convergence rate is also presented.

Finally, we proposed a broadband DOA estimation technique based on Lee's method [1]. The proposed technique greatly reduces computation by operating in beamspace. Furthermore, the proposed technique is capable of estimating the DOAs of broadband signals by using the frequency invariant design we proposed for deterministic CRA. Comparing to conventional incoherent broadband estimation technique, our proposed method achieves significantly better estimation accuracy, requires much less computation and is able to estimate the DOAs for correlated signals.

1.4 Content Organization

The rest of the dissertation is organized as the following. Chapter 2 prepares the fundamentals and the theoretical background of array processing and beamforming. Chapter 3 presents the design of deterministic broadband CRA. The development of the partially adaptive CRA is discussed in Chapter 4. A broadband DOA estimator for CRA is proposed in Chapter 5. Chapter 6 presents the application of CRA to bird monitoring. Chapter 7 summarizes this dissertation and discusses the future research topics.

Chapter 2

Introduction to Beamforming

In this chapter, we introduce the terminologies and fundamentals in array processing and beamforming. The purpose is to provide the theoretical foundation of our research.

The organization of this chapter is as the follows. In Section 2.1, we introduce array processing basics including coordinate systems, description of spatial signal, and the signal model for array processing. In section 2.2, we review the beamforming techniques by their categories: the conventional techniques and modern techniques. The various array geometries and their characteristics are introduced in Section 2.3 followed by a more detailed discussion on circular array in Section 2.4. Section 2.5 is the summary.

2.1 Array Processing Basics

2.1.1 Coordinate System

Two types of three-dimensional (3-D) coordinate systems are usually used to describe a spatial signal: the Cartesian coordinate system and the spherical coordinate system.

The Cartesian coordinate system uses x , y and z as the spatial variables to specify any point in a right-handed orthogonal coordinate system as shown in Fig. 2.1. In some applications, the spherical coordinate system is more appropriate to use. The spherical coordinate system denotes any point in the 3-D space by its distance r from the origin,

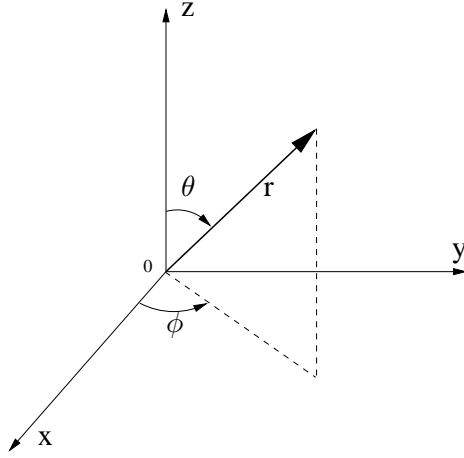


Figure 2.1: The Cartesian and spherical coordinate systems.

the azimuth angle ϕ with respect to the x -axis and the elevation angle θ with respect to the z -axis as shown in Fig. 2.1. The coordinates in the two coordinate systems are related by

$$x = r \sin \theta \cos \phi$$

$$y = r \sin \theta \sin \phi$$

$$z = r \cos \theta$$

With time being the fourth dimension, a space-time signal in 3-D space can be denoted as $s(x, y, z, t)$ in the Cartesian coordinate system, or $s(r, \phi, \theta, t)$ in the spherical coordinate system. For simplicity, vector representation is also used. Define the three unit vectors in the Cartesian coordinate axes as \vec{l}_x , \vec{l}_y and \vec{l}_z . They have the following properties

$$\vec{l}_x \cdot \vec{l}_x = \vec{l}_y \cdot \vec{l}_y = \vec{l}_z \cdot \vec{l}_z = 1$$

$$\vec{l}_x \cdot \vec{l}_y = \vec{l}_y \cdot \vec{l}_z = \vec{l}_z \cdot \vec{l}_x = 0$$

$$\vec{l}_x \times \vec{l}_y = \vec{l}_z$$

Using the vector representation, $s(x, y, z, t)$ is written as $s(\vec{x}, t)$, where \vec{x} is $x\vec{l}_x + y\vec{l}_y + z\vec{l}_z$.

2.1.2 Signals in Space and Time

The propagation of any space-time signal $s(\vec{x}, t)$ obeys the wave equation given by [2]

$$\frac{\partial^2 s}{\partial x^2} + \frac{\partial^2 s}{\partial y^2} + \frac{\partial^2 s}{\partial z^2} = \frac{1}{c^2} \frac{\partial^2 s}{\partial t^2} \quad (2.1)$$

where c is the propagation speed of the signal. We assume that the signal is propagating in the same media and c is always a constant. For example, the speed of acoustic wave in dry air under normal temperature is approximately $343m/s$.

Assuming $s(\vec{x}, t)$ is a monochromatic plane wave having the form of a complex exponential

$$s(\vec{x}, t) = Ae^{j(\omega t - \vec{k} \cdot \vec{x})} \quad (2.2)$$

where $j = \sqrt{-1}$ and ω is the angular frequency of the signal and \vec{k} is a vector termed as the wavenumber vector and has an amplitude of $|k| = 2\pi/\lambda$. Putting (2.2) into (2.1) yields

$$k_x x + k_y y + k_z z = C \quad (2.3)$$

where C is a constant. Thus as long as (2.3) is satisfied, a signal with the form given in (2.2) is a solution to the wave equation. Equation (2.3) defines a plane of constant phase. At any point on the plane, the signal $s(\vec{x}, t)$ has the same phase delay given by $\vec{k} \cdot \vec{x}$. By defining $\vec{\alpha} = \vec{k}/\omega$, (2.2) can also be written as

$$s(\vec{x}, t) = Ae^{j\omega(t - \vec{\alpha} \cdot \vec{x})}, \quad (2.4)$$

and $\vec{\alpha} \cdot \vec{x}$ corresponds to the delay in time.

Since the wave equation (2.1) is a linear equation and an arbitrary signal can be represented by an integral of complex exponentials using Fourier theory, it can be concluded that an arbitrary signal

$$\begin{aligned} s(\vec{x}, t) &= \frac{1}{2\pi} \int_{-\infty}^{\infty} S(\omega) e^{j(\omega t - \vec{k} \cdot \vec{x})} d\omega \\ &= \frac{1}{2\pi} \int_{-\infty}^{\infty} S(\omega) e^{j\omega(t - \vec{\alpha} \cdot \vec{x})} d\omega \end{aligned} \quad (2.5)$$

satisfying (2.3) is also a solution to the wave equation. Here $S(\omega)$ is the Fourier spectrum of the signal. Notice that $|\alpha| = |\vec{k}/\omega| = 1/c$, thus the time delay $\vec{\alpha} \cdot \vec{x}$ is independent of the angular frequency ω , which implies that all frequency components have the same amount of time delay at any particular position. This is a very important property of a propagating wave, since it ensures that the temporal shape of the propagating signal is preserved and recovery of the signal is possible.

2.1.3 Array Processing Signal Model

Similar to (2.2), we can write a narrow band signal in the complex exponential form as

$$s(\vec{x}, t) = s(t)e^{j(\omega t - \vec{k} \cdot \vec{x})} \quad (2.6)$$

where $s(t)$ is a slowly time-varying signal comparing with its carrier $e^{j\omega t}$, i.e., the bandwidth of $s(t)$ is much less than the center frequency ω .

The received array signal is usually converted to base-band for further processing. Thus the carrier term $e^{j\omega t}$ in (2.6) can be dropped and the received base-band signal at the n th array element is

$$x_n(t) = s(t)e^{-j\vec{k}_n \cdot \vec{x}_n} = a_n s(t) \quad (2.7)$$

where \vec{x}_n denotes the position vector of the n th array element, \vec{k}_n is the wavenumber vector associated with that element, and $a_n = e^{-j\vec{k}_n \cdot \vec{x}_n}$.

For an array of N elements, the received array signal vector can be written in matrix form as

$$\mathbf{x}(t) = \mathbf{a}s(t)$$

where $\mathbf{a} = [a_1, a_2, \dots, a_N]^T$ is named as the steering vector.

When a number of Q , $Q < N$, signals impinge on the array, the received array signal

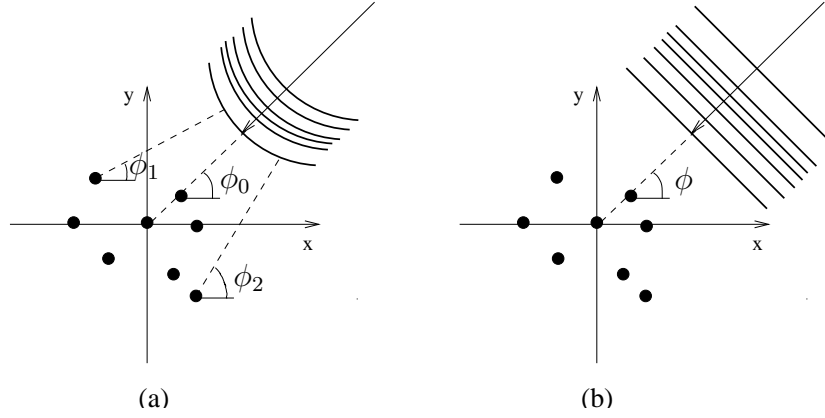


Figure 2.2: (a) Near-Field and (b) Far-Field scenarios.

vector becomes

$$\begin{aligned}\mathbf{x}(t) &= \sum_{q=1}^Q \mathbf{a}_q s_q(t) \\ &= \mathbf{A} \mathbf{s}(t)\end{aligned}$$

where $s_q(t)$ denotes the q -th incoming signal and \mathbf{a}_q is its steering vector. $\mathbf{A} = [\mathbf{a}_1, \mathbf{a}_2, \dots, \mathbf{a}_Q]$ is the steering matrix and $\mathbf{s}(t) = [s_1(t), s_2(t), \dots, s_Q(t)]^T$ is the signal vector. Here the superscript (T) denotes transpose.

In the presence of additive noise, the received array signal becomes

$$\mathbf{x}(t) = \mathbf{A} \mathbf{s}(t) + \mathbf{n}(t) \quad (2.8)$$

The array output $y(t)$ is formed as a weighted sum of all the received signals

$$y(t) = \mathbf{w}^H \mathbf{x}(t) \quad (2.9)$$

where the superscript (H) denotes conjugate transpose and $\mathbf{w} = [w_1, w_2, \dots, w_N]$ is a $N \times 1$ weighting vector.

2.1.4 Near-field and Far-field Assumption

Whether the signal source is located in the near field or far field of the array affects the modeling of the received signal. When the source is close to the array so that

the wavefront of the propagating signal appears to be curved to the array, the source is considered as a near field source. The directions of the propagation measured at different array elements may be different as shown in Fig. 2.2 (a).

If the source is far from the array and the wavefront of the propagating signal, when examined in a dimension comparable to the array size, is perceived as a plane, the source is considered as a far field source. The direction of propagation at different array elements is considered the same as shown in Fig. 2.2 (b). This results in a simplification of modelling of the received signal in (2.7), where all the wavenumber vectors are the same, i.e., $\vec{k}_n = \vec{k}$.

2.2 Beamforming Techniques

Choosing different \mathbf{w} in (2.9) to form the array output results in different spatial response of the array. The spatial response of a given array as a function of the spatial angles is called the beam pattern. The 2-D beam pattern of a linear array as a function of azimuth angle θ , with the array lying in the x -axis, is shown in Fig. 2.3. The beam pattern has a mainlobe and many sidelobes. A desirable beam pattern should have its mainlobe centered around the Direction Of Arrival (DOA) of the desired signal and low sidelobe level in other directions. Given an array geometry, how to achieve a desirable beam pattern is the central task of various beamforming techniques.

Beamforming is a term generally used to refer to various spatial filtering techniques used in array processing. Beamforming technique dates back to the World War II and has been an active research area ever since. Over more than half a century, beamforming techniques have evolved greatly. Based on the time of their emergence, they are usually classified as the conventional beamforming techniques or the modern beamforming techniques [72]. Conventional beamforming techniques include: delay-and-sum beamforming and tapered beamforming. Modern techniques include: statistically optimum

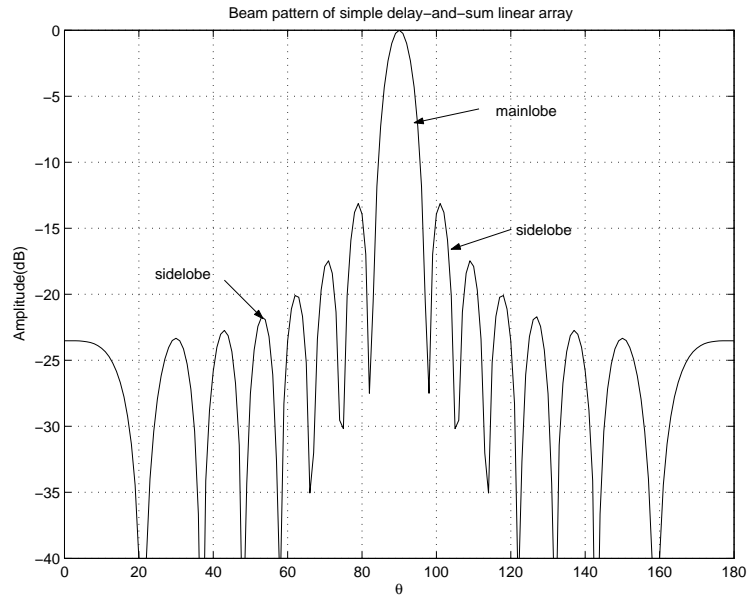


Figure 2.3: The beam pattern of a linear array. The linear array consists of 15 equally spaced array elements, spacing between adjacent elements is half of the wavelength.

beamforming, adaptive beamforming, and sub-spaced method. In the following, we will briefly review those techniques.

2.2.1 Conventional Beamforming Techniques

(1) Delay-and-sum Beamforming

The idea of delay-and-sum beamforming is very simple. The interested propagating signal received at the array elements are associated with a time delay determined by the locations of the array elements and propagation direction. By introducing extra amount of delay in the received signals so that the desired signal in every array element has the same amount of delay with respect to a reference point, the addition of the delayed signals will reinforce the aligned desired signal. Signals and noise in other directions are not aligned and are attenuated relatively. The implementation of such a delay-and-sum beamformer is shown in Fig. 2.4. The output $y(t)$ of a delay-and-sum beamformer with

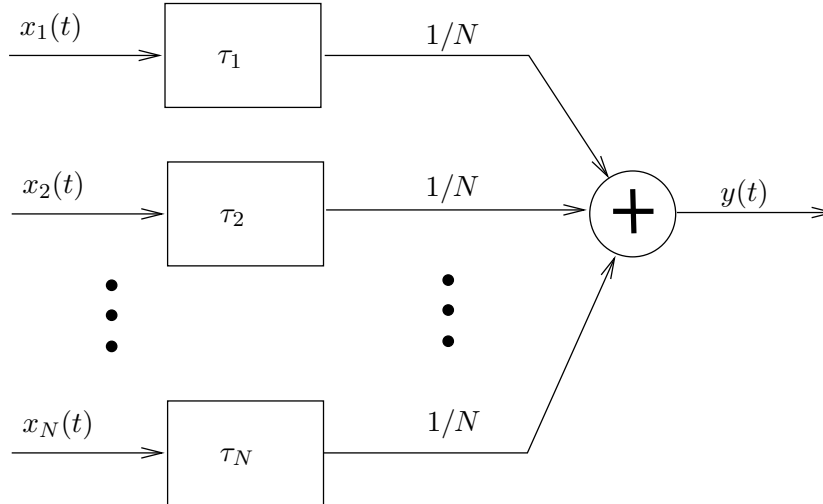


Figure 2.4: The delay-and-sum beamformer.

N array elements has the form

$$y(t) = \frac{1}{N} \sum_{n=1}^N x_n(t - \tau_n) \quad (2.10)$$

where τ_n is the delay introduced for the n th received signal. The improvement in Signal-to-Noise Ratio (SNR) of such a delay-and-sum beamformer is proportional to the number of array elements.

The delay-and-sum beamformer can be extended by combining temporal filtering at the beginning, results in the filter-and-sum beamformer. The filtering only lets through the part of spectrum that is supposed to contain the desired signal, thus noise and interference reside in other spectral ranges are filtered out. The filter-and-sum beamforming is most effective when the desired signal has very distinctive spectral characteristics as to that of the interferences and noise.

The delay-and-sum beamforming also has its frequency domain counterpart. Since the delay in time domain corresponds to linear phase shift in the frequency domain, by transforming to the frequency domain using Fast Fourier Transform (FFT), the desired signal can be aligned by appropriate phase shift and therefore reinforced after addition.

(2) Tapered Beamforming

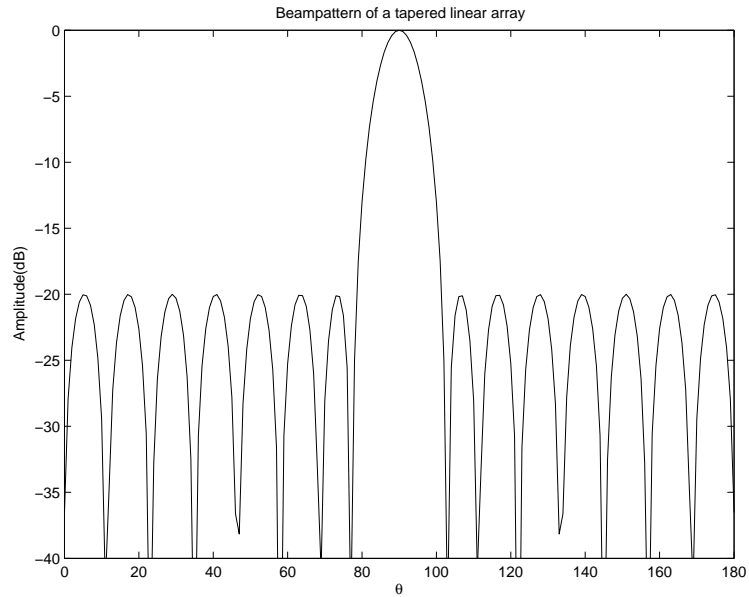


Figure 2.5: The beam pattern of a tapered linear array. The value of the tapers are generated using a -20dB Chebyshev function. The linear array has the same configuration as in Fig. 2.3

The delay-and-sum beamforming usually yields high sidelobe level around the mainlobe. When there are strong interferences coming through those high sidelobe regions, the beamformer output will be degraded. The need to reduce sidelobe level or even to specify the entire beam pattern gives rise to a type of beamforming method called tapered beamforming. Unlike the delay-and-sum beamforming where the weights of each array element only differ in phase but have the same amplitude, the tapered beamforming introduces a tapering to the amplitude of the weights. To achieve a desired beam pattern, the values of the tapers can be designed using conventional filter design algorithms. Many such algorithms are available, among them the most known one is the Dolph-Chebyshev method. The Dolph-Chebyshev method is able to generate the lowest sidelobe level for a specified mainlobe width, or a narrowest mainlobe width for a specified sidelobe level. Fig. 2.5 shows a beam pattern obtained through a tapered beamformer. An equal sidelobe level of -20dB is achieved in this example.

2.2.2 Modern Beamforming Techniques

(1) Statistically Optimum Beamforming

In the conventional beamforming technique, the beampattern is fixed. When there are strong interferences, the sidelobe level may not be low enough to cancel them out. On the other hand, setting the sidelobe level to a very low value will unnecessarily increase the mainlobe width and therefore increase the noise taken in through the mainlobe. In optimum beamforming techniques, the weights are chosen based on the *a priori* knowledge of the received data. Several optimization criteria can be used to derive the weights, they are: 1) maximization of the signal-to-interference-plus-noise ratio; 2) minimization of the interference and noise power with respect to some constraints; 3) minimization of the output power with respect to some constraints. Among them, the last one is the most general formulation of the statistically optimum beamforming problem and it is described in more detail below.

Denote the spatial covariance matrix of the array data by \mathbf{R} , i.e., $\mathbf{R} = E[\mathbf{x}(t)\mathbf{x}(t)^H]$, where $\mathbf{x}(t)$ is given in (2.8). The optimum weights \mathbf{w}_{opt} is obtained through

$$\mathbf{w}_{opt} = \min_{\mathbf{w}} \mathbf{w}^H \mathbf{R} \mathbf{w} \quad \text{subject to} \quad \mathbf{C}^H \mathbf{w} = \mathbf{b}$$

where \mathbf{C} is the constraint matrix and \mathbf{b} is the constraint value vector. Beamformer obtained using this method is known as Linear Constrained Minimum-Variance (LCMV) beamformer. The optimum solution is found to be [2]

$$\mathbf{w}_{opt} = \mathbf{R}^{-1} \mathbf{C} (\mathbf{C}^H \mathbf{R}^{-1} \mathbf{C})^{-1} \mathbf{b}. \quad (2.11)$$

A special case for the solution occurs when the signal's spatial covariance matrix is a proportion of an identity matrix, and only spatially white noise exists. The solution then becomes

$$\mathbf{w}_q = \mathbf{C} (\mathbf{C}^H \mathbf{C})^{-1} \mathbf{b}. \quad (2.12)$$

It is termed the quiescent solution, which is determined by the linear constraints only.

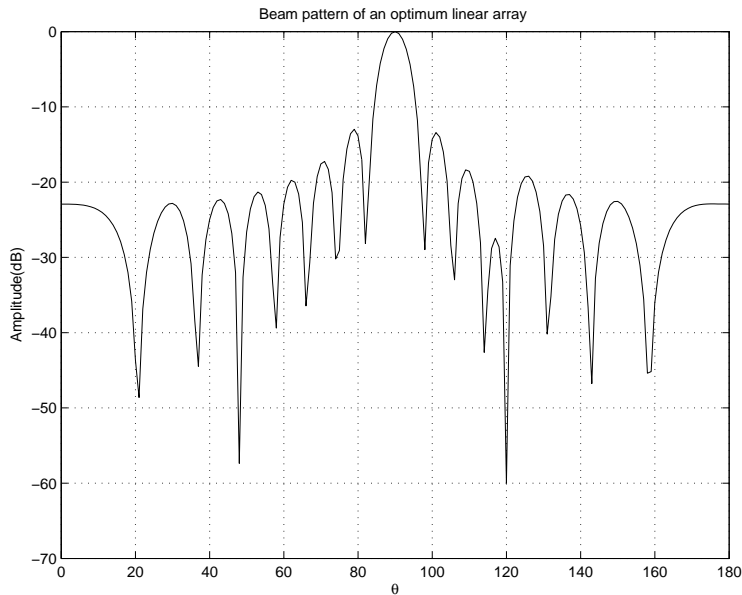


Figure 2.6: The beam pattern of an optimum linear array. The linear array has the same configuration as in Fig. 2.3

Fig. 2.6 shows the beam pattern of a uniform linear array obtained using a LCMV solution in (2.12). Two linear constraints are used, one is the unit gain constraint at the main look direction $\theta = 90^\circ$, the other constraint puts a $-60dB$ null at $\theta = 120^\circ$, where a strong interference is supposed to exist. Notice that the sidelobe is almost maintained in the same level as that in the beam pattern of a delay-and-sum beamformer in Fig. 2.3.

LCMV beamformer can be implemented directly using (2.11). An alternative way to implement a LCMV is using the so called General Sidelobe Canceller (GSC) [73] shown in Fig. 2.7. In a GSC, the upper branch is non-adaptive and its output is $y_q(t) = \mathbf{w}_q^H \mathbf{x}(t)$, where \mathbf{w}_q is the quiescent solution given in (2.12).

In the lower branch, \mathbf{B} is a blocking matrix satisfying $\mathbf{C}^H \mathbf{B} = \mathbf{0}$, so that the desired signal specified in \mathbf{C} will not be leaked into the lower branch. The lower branch performs an unconstrained optimization problem in which the weighting vector \mathbf{w}_a is chosen to minimize the mean square error between the outputs of the lower branch $y_a(t)$ and upper

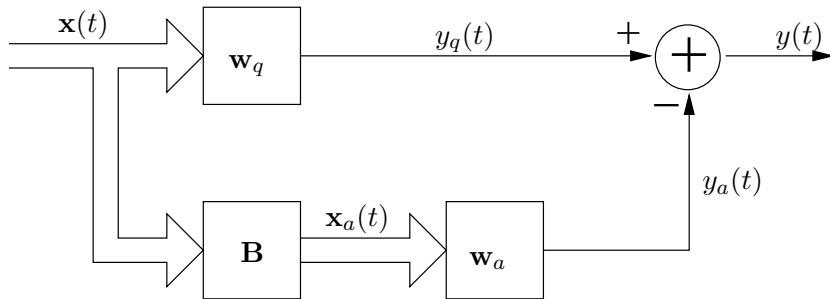


Figure 2.7: General sidelobe canceller.

branch $y_q(t)$. The optimum solution of \mathbf{w}_a is given by the Wiener-Hopf equation [72]

$$\mathbf{w}_{a,opt} = \mathbf{R}_{x_a x_a}^{-1} \mathbf{r}_{x_a y_q} \quad (2.13)$$

where $\mathbf{R}_{x_a x_a} = E[\mathbf{x}_a(t)\mathbf{x}_a^H(t)]$ is the lower branch covariance matrix and $\mathbf{r}_{x_a y_q} = E[\mathbf{x}_a(t)y_q^*(t)]$ is the cross-correlation vector between $\mathbf{x}_a(t)$ and $y_q(t)$. Here the superscript (*) denotes complex conjugate.

The GSC is equivalent to the original LCMV beamformer implementation, it can be perceived as estimating the interference in the upper branch and then subtracting them from the quiescent output.

(2) Adaptive Beamforming

When developing the statistically optimum beamformer, if the weights are set only with *a priori* knowledge of the statistics of the array signal, the resulting beamformer is a non-adaptive one. The design result is good only if the signal environment is stationary, i.e., the signal and interferences characteristics as well as their DOAs are fixed. Statistically optimum beamformer can also be implemented as adaptive beamformer by updating the weights using current statistics of the array signal. This is usually required in non-stationary signal environment, where adaptive beamformers are able to track the changes in the signal characteristics. We examine the adaptive implementation of some of the statistically optimum beamformers below.

The most known statistically optimum beamformers include the LCMV beamformer, Multiple Sidelobe Canceller (MSC), and beamformers based on maximization of SNR

or SINR [74]. When implemented in adaptive form, the last two types of beamformers have a common limitation that they can only update their weights when the desired signal is absent to avoid cancellation of it. The LCMV beamformer can overcome this limitation by putting linear constraints on its weights. Thus LCMV, together with its alternative form the GSC, are the most widely used adaptive beamformers. We leave the more detailed discussion on this topic to Chapter 4.

(3) Subspace Methods

Subspace method explores the eigen-structure of the spatial covariance matrix \mathbf{R} of the array signal. Through eigen-decomposition of \mathbf{R} , the space containing both the desired signal and noise is decomposed into two subspaces: the noise subspace and the desired signal plus noise subspace. Several works [75–78] discuss the techniques that can be used to extract the desired signal from the signal plus noise subspace. Subspace methods are also widely used in DOA estimation, this topic will be discussed in Chapter 7.

2.3 Array with Different Geometry

The placement of array elements in the space corresponds to the spatial sampling pattern of the signal field. Usually, the choice of a certain array geometry is the outcome of consideration of several factors, namely the application requirements, physical constraints, algorithm complexity and cost in deployment etc. Array geometry is best classified by the number of dimensions that the array spans, i.e., 1-D array, 2-D array or 3-D array.

2.3.1 1-D Array

1-D array is also called linear array. Depending on the array element spacing, linear arrays can be further classified into: equally spaced linear array or unequally spaced linear array. The former is also known as the Uniform Linear Array (ULA) in literature.

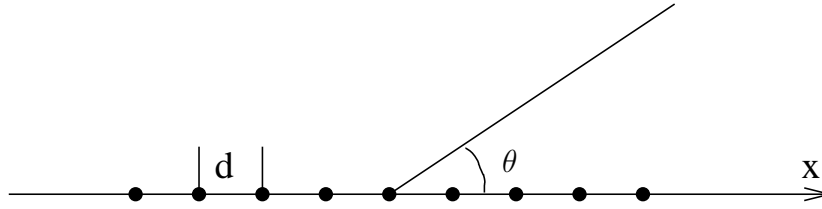


Figure 2.8: Uniform linear array.

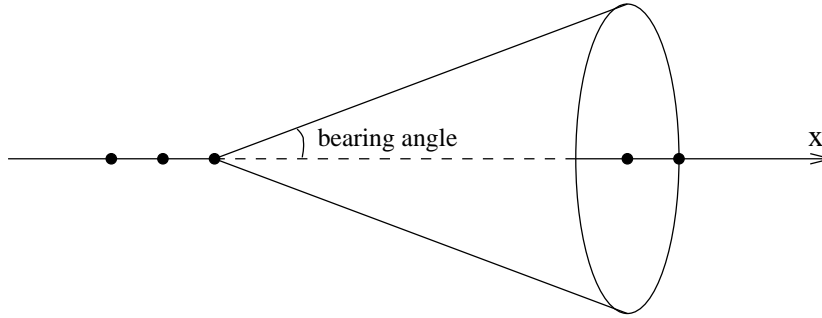


Figure 2.9: The ambiguity DOAs of a linear array

ULA is the most widely used array geometry due to its simple and regular physical form and efficiency in its array algorithms. Fig. 2.8 shows a ULA, where d is the spacing between two adjacent elements. A usually followed rule of setting d is $d \leq \lambda_{min}/2$, where λ is the wavelength of the highest operating frequency of the ULA. When this requirement on d is not satisfied, grating lobes, or in other words, false mainlobes will appear in the beampattern. When d is fixed, the size of an N element ULA is $(N - 1)d$. The larger the size is the array, the narrower will be the mainlobe width.

Array lengths of several hundreds of λ or higher is quite common in many practical applications. Because of the requirement that $d \leq \lambda_{min}/2$ in ULA, a large number of array elements are necessary in those large arrays. Unequally spaced linear array is developed mainly to reduce the number of array elements of a ULA while keeping a comparable performance. Design of unequally spaced linear array is discussed in [79–81].

Although linear array is appealing for its simple form, it has an inherent limitation regarding source localization. As long as the bearing angle between the incoming signal and the linear array is the same, it appears to a linear array that the incoming signal

is always from the same direction. The ambiguity directions form a cone wrapping around the linear array as shown in Fig. 2.9. All the coming signals through this cone is reinforced by the linear array, no matter they are the desired signal, interference or noise. Since the DOA of the incoming signal has infinite possibility, source localization within this cone is impossible.

2.3.2 2-D Array

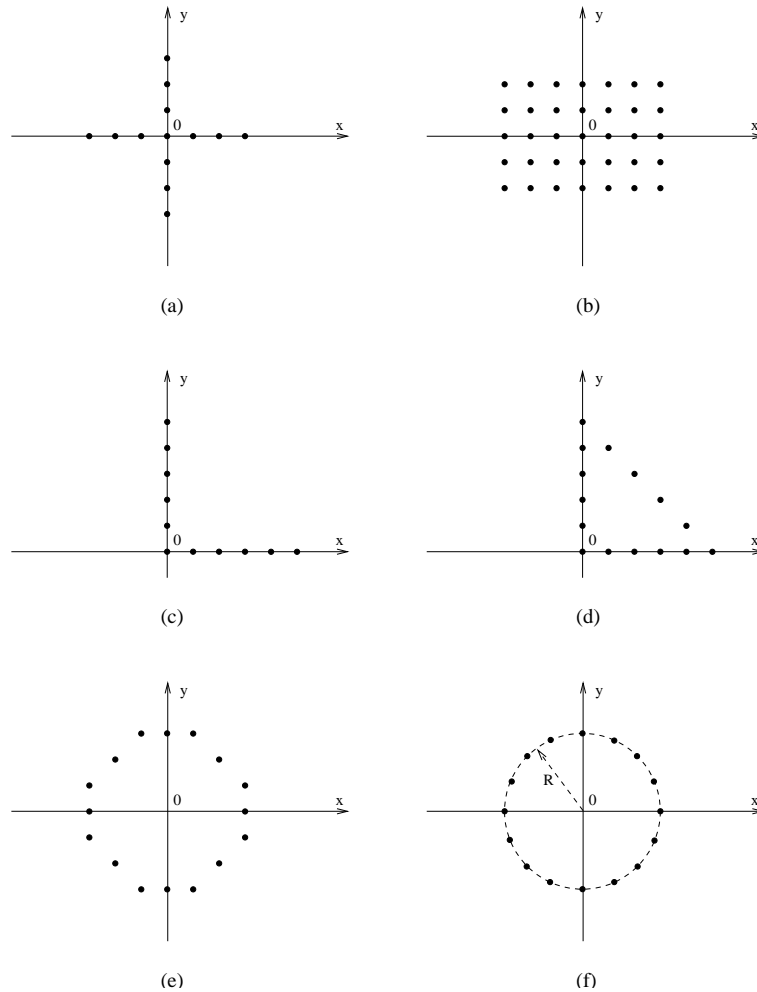


Figure 2.10: 2-D arrays. (a) cross array (b) rectangular array (c) L-shape array (d) right triangle array (e) octagon array (f) circular array.

2-D array can take a regular geometry form or irregular geometry form. Shown in Fig. 2.10 are some of the most frequently used regular 2-D arrays [82]. Irregular 2-D

array takes an arbitrary geometry which does not fit into any of those regular shapes.

Comparing to 1-D array, 2-D array has the advantage that the DOA ambiguity is reduced to two DOAs, which are symmetric with respect to the plane where the 2-D array lies in. This greatly increases the source localization accuracy. In fact, in a lot of practical source localization problems, one of the ambiguity DOAs can be easily eliminated using some *a priori* knowledge. The reduction of ambiguity DOAs also reduces the amount of interference and noise coming through the ambiguity DOAs.

We will introduce the basic concepts and properties of circular array in Section 2.4, since it is the focus of our work. Studies on other regular 2-D arrays can be found in [82–84]. Irregular arrays are not studied separately, modern beamforming techniques which can be applied to array with arbitrary geometry are available for them.

2.3.3 3-D Array

Some of the commonly used 3-D arrays are cylinder array, sphere array and 3-D arrays formed by adding one dimension to those regular 2-D arrays. Irregular 3-D arrays are seldom. 3-D array totally eliminates the ambiguity of DOA. Studies on 3-D array can be found in [85, 86].

2.4 Circular Array

Circular array, also termed as ring array, has all its array elements placed on the circumference of a circle. Comparing to other 2-D arrays, circular array has received considerable interest because it provides almost uniform beampattern for 360° azimuthal coverage. When the array elements are equally spaced, the array is entitled as Uniformly Circular Array (UCA). Because of the symmetrical structure of the UCA, the steering direction can be easily changed in the azimuth angle by simply shifting weights among array elements. Unequally spaced circular array are not common. In our work, we only

consider UCAs. We also assume the signal source is located in the far-field.

A UCA with $N(N = 16)$ array elements is shown in Fig. 2.10 (f). Using the vector representation defined in Section 2.1.1, the position vector of the n -th array element is

$$\vec{r}_n = \vec{l}_x R \cos \gamma_n + \vec{l}_y R \sin \gamma_n, \quad n = 1, 2, \dots, N$$

where R is the radius and $\gamma_n = 2\pi(n - 1)/N$ is the azimuth angle of the n -th element.

The 3-D array pattern of the UCA as a function of the azimuth angle ϕ and elevation angle θ is

$$f(\phi, \theta) = \sum_{n=1}^N w_n^* e^{j\vec{k} \cdot \vec{r}_m} \quad (2.14)$$

where w_m is the weights for the m -th element and \vec{k} is an arbitrary wavenumber vector given by

$$\vec{k} = \vec{l}_x k \sin \theta \cos \phi + \vec{l}_y k \sin \theta \sin \phi + \vec{l}_z k \cos \theta.$$

where $k = 2\pi/\lambda$ with λ being the wavelength of the operating frequency.

Considering the design of a delay-and-sum beamformer whose main look direction is (ϕ_0, θ_0) , the delay-and-sum weight is found to be [87]

$$w_m = \frac{1}{N} e^{j\vec{k}_0 \cdot \vec{r}_m} \quad (2.15)$$

where \vec{k}_0 is the wavenumber vector associated with the look direction and is equal to

$$\vec{k}_0 = \vec{l}_x k \sin \theta_0 \cos \phi_0 + \vec{l}_y k \sin \theta_0 \sin \phi_0 + \vec{l}_z k \cos \theta_0.$$

Putting (2.15) into (2.14) yields the delay-and-sum beampattern of a UCA

$$\begin{aligned} f(\phi, \theta) &= \frac{1}{N} \sum_{n=1}^N e^{j(\vec{k} - \vec{k}_0) \cdot \vec{r}_m} \\ &= \frac{1}{N} \sum_{n=1}^N e^{-jkR[\sin \theta_0 \cos(\phi_0 - \gamma_n) - \sin \theta \cos(\phi - \gamma_n)]} \end{aligned} \quad (2.16)$$

By defining

$$\xi = \arccos \frac{\sin \theta \cos \phi - \sin \theta_0 \cos \phi_0}{\rho}, \quad (2.17)$$

$$\rho = \sqrt{(\sin \theta \cos \phi - \sin \theta_0 \cos \phi_0)^2 + (\sin \theta \sin \phi - \sin \theta_0 \sin \phi_0)^2}, \quad (2.18)$$

equation (2.16) can be written in a simpler form as [87]

$$f(\phi, \theta) = \frac{1}{N} \sum_{n=1}^N e^{-jkR\rho \cos(\xi - \gamma_n)} \quad (2.19)$$

The delay-and-sum beampattern of a UCA in (2.19) can be further expressed as the sum of various Bessel functions of different orders [87],

$$f(\phi, \theta) = J_0(kR\rho) + 2 \sum_{q=1}^{\infty} j^{Nq} J_{Nq}(kR\rho) \cos(Nq\xi) \quad (2.20)$$

where $J_m(\cdot)$ is the m -th order Bessel function of the first kind.

Comparing (2.20) with the beampattern of a continuous circular ring antenna [87]

$$f(\phi, \theta) = J_0(kR\rho), \quad (2.21)$$

it is seen that they only differ in the second term which contains the high order Bessel functions. It will be shown in Chapter 3, when the number of array elements N in the UCA is large enough, the second term in (2.20) will be negligible and the beampattern of a UCA can be represented by (2.21).

We assume N is large enough and examine the beampattern of a UCA represented by the $J_0(\cdot)$ function. Fig. 2.11 shows the plot of $J_0(s)$, $s \in [-20, 20]$. The $J_0(s)$ function contains sidelobes as high as $-7dB$. Such high sidelobe level in the beampattern is unacceptable in most applications, thus how to reduce the sidelobe level for a UCA becomes an important task. This topic will be dealt in Chapter 3.

2.5 Summary

By introducing some of the terminologies and basic theory in array processing and beamforming, this chapter serves as a preparation for topics in the remaining chapters. In reviewing of those basics, we put more emphasis on those topics closely related to

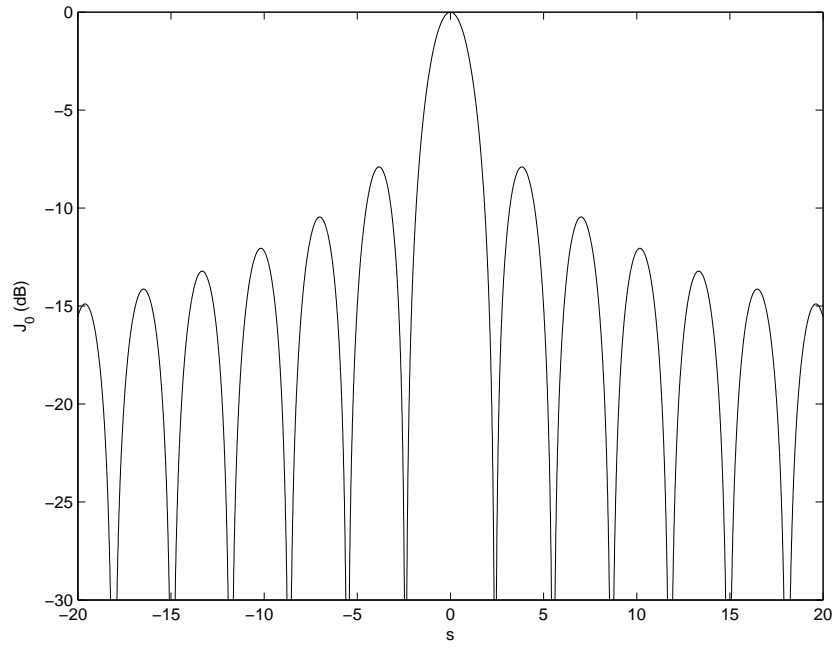


Figure 2.11: Bessel functions $J_0(s)$, $s \in [-20, 20]$.

our research work. Some of the sections will be referenced through out the remaining chapters.

Chapter 3

Deterministic Beamforming Using Concentric Ring Array

In this chapter we first introduce the structure of the concentric ring array(CRA). The weights of the array is decomposed into two parts: the intra-ring weights for array elements on each ring and the inter-ring weights representing the contribution to the array pattern from each ring. Our proposed design is based on a previous work by Stearns and Stewart [33] that addressed concentric ring antenna design for continuous rings, narrowband input and 2-D scenario only. We first generalize their method to 3-D beamforming and then propose three methods to obtain inter-ring weights at different frequencies that can control sidelobe and/or mainlobe. The proposed methods can be applied in frequency domain based broadband beamformer. A nested array design is proposed to further extend the operating frequency range. We also show that our deterministic design can be incorporated into the Linear Constrained Minimum-Variance (LCMV) [88] to generate nulls in the array pattern to cancel strong interferences.

The rest of the chapter is organized as follows. Section 3.1 introduces the structure of a CRA and presents the decomposition of CRA weights. In Section 3.2, we briefly review Stearns and Stewart's work. We generalize their work to 3-D beamforming in Section 3.3. The proposed methods to derive inter-ring weights are described in Section

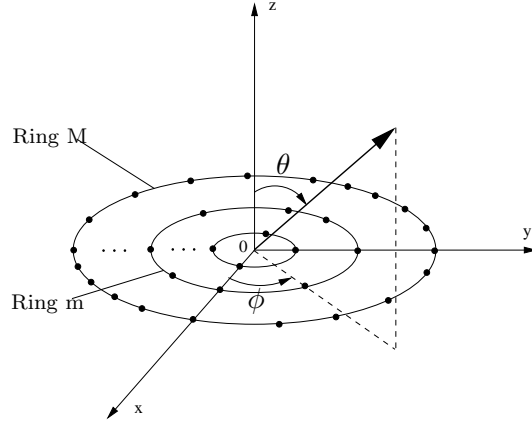


Figure 3.1: Geometry of a CRA.

3.4. In Section 3.5, we discuss the implementation of a broadband beamformer using proposed methods. Section 3.6 presents examples and simulations and Section 3.7 is a summary.

3.1 Beamforming Using CRA

3.1.1 CRA Structure

The CRA considered is shown in Fig. 3.1.1, where ϕ and θ denote the azimuth angle and the elevation angle with respect to the z -axis. The array consists of M rings. The numbering of the rings starts from the inner most one so that the inner most ring is called the *1st* ring and the outer most ring is the *M-th* ring. The *m-th*, $m = 1 \dots M$ ring has N_m equally spaced array elements and its radius is denoted by R_m . The total number of array elements is $K = \sum_{m=1}^M N_m$.

For a narrow-band signal impinging on the CRA, the beamformer output at time instant n is

$$z(n) = \sum_{m=1}^M \sum_{i=1}^{N_m} v_{mi}^* x_{mi}(n) = \mathbf{v}^H \mathbf{x}(n) \quad (3.1)$$

where $x_{mi}(n)$ is the received signal from the *i-th* element on the *m-th* ring, v_{mi} is the

corresponding weight. $\mathbf{x}(n)$ and \mathbf{v} are the received data vector and weight vector respectively, both are of size $K \times 1$. By choosing the weights v_{mi} properly, the array can enhance a directional signal and reduce interferences and noise.

3.1.2 Design of the CRA Weights

Our proposed method does not obtain \mathbf{v} directly, but rather decomposes \mathbf{v} into two different sets of weights that will be chosen differently. The reason is because each ring in the CRA can be viewed as a stand alone array with the output

$$y_m(n) = \mathbf{h}_m^H \mathbf{x}_m(n), \quad (3.2)$$

where $\mathbf{x}_m(n) = [x_{m1}(n), x_{m2}(n), \dots, x_{mN_m}(n)]^T$ is a $N_m \times 1$ vector containing the data received by the elements on the m -th ring and \mathbf{h}_m denotes the corresponding weight vector. The final output $z(n)$ of the CRA can then be formed as a weighted sum of the output from each ring:

$$z(n) = \mathbf{w}^H \mathbf{y}(n), \quad (3.3)$$

where $\mathbf{y}(n) = [y_1(n), y_2(n), \dots, y_M(n)]^T$ and $\mathbf{w} = [w_1, w_2, \dots, w_M]^T$ is the weight vector that governs the contribution of the individual rings to the final output.

Putting (3.2) into (3.3) yields

$$z(n) = \mathbf{u}^H \mathbf{x}(n) \quad (3.4)$$

where $\mathbf{x}(n) = [\mathbf{x}_1^T(n), \mathbf{x}_2^T(n), \dots, \mathbf{x}_M^T(n)]^T$ is the same array data vector defined in (3.1), and

$$\mathbf{u} = [w_1 \mathbf{h}_1^T, w_2 \mathbf{h}_2^T, \dots, w_M \mathbf{h}_M^T]^T. \quad (3.5)$$

Comparing (3.4) and (3.1) reveals that \mathbf{u} is a partitioned form of \mathbf{v} and there are a total number of $(K + M)$ weighting parameters in \mathbf{u} .

Among these $(K + M)$ weights, we can set \mathbf{h}_i to be the delay-and-sum weights computed based on the *a priori* knowledge of the desired signal's DOA. The delay-and-sum weight for a circular ring array is developed in Section 2.4 as given in equation (2.16). Similar to (2.16), when a narrow-band signal of wavelength λ is impinging on the array in the direction of (ϕ_0, θ_0) , the delay-and-sum weight of the i th element on the m -th ring is obtained as

$$h_{mi} = \frac{1}{N_m} e^{jkR_m[\sin \theta_0 \cos(\phi_0 - \gamma_{mi})]}, \quad i = 1, 2, \dots, N_m \quad (3.6)$$

where $\gamma_{mi} = 2\pi(i - 1)/N_m$ is the azimuth angle of this element and $k = 2\pi/\lambda$. The delay-and-sum weights allows a maximum reduction of ambient noise when it is spatially white.

When setting h_{mi} to the delay-and-sum weight given in (3.6), the array pattern of the m -th ring becomes the delay-and-sum array pattern of a UCA as given in Section 2.4. As pointed out earlier, if there are sufficient number of elements on a ring, the array pattern of the m -th ring equals the array pattern of a continuous ring that has the zero order Bessel function term only, which is

$$F_m(\phi, \theta) = J_0(kR_m\rho). \quad (3.7)$$

The condition to make this valid will be discussed in Subsection 3.3.1. With this assumption, we can write the array pattern of the CRA with M rings as

$$\begin{aligned} F(\phi, \theta) &= \sum_{m=1}^M w_m F_m(\phi, \theta) \\ &\approx \sum_{m=1}^M w_m J_0(kR_m\rho) \end{aligned} \quad (3.8)$$

where w_m represents the weight for the array pattern of the m -th ring. The weighted sum of the beam patterns from different rings can result in lower sidelobe level and rejecting directional interference if the weights are chosen carefully. Thus w_m plays a central role in the synthetic array pattern for CRA.

3.2 Stearns and Stewart's Method

In [33], Stearns and Stewart examined the sidelobe control problem of a continuous concentric ring antennas. They developed their method for the special case of 2-D beamforming in the x-y plane. In such case, $\theta = \pi/2$, $\theta_0 = \pi/2$ and ρ in (2.18) becomes

$$\rho = 2 \left| \sin\left(\frac{\phi - \phi_0}{2}\right) \right|, \quad \phi \in [0, 2\pi] \quad (3.9)$$

Putting the above equation into (3.8) yields the 2-D array pattern

$$F(\phi) = \sum_{m=1}^M w_m J_0(2kR_m \left| \sin\left(\frac{\phi - \phi_0}{2}\right) \right|). \quad (3.10)$$

The weight w_m is then obtained through the infinite Fourier-Bessel series expansion as explained below.

For any continuous function $g(\varphi)$ defined in $[0, 1]$, it can be expanded as an infinite Fourier-Bessel series as [33]

$$g(\varphi) = \sum_{m=1}^{\infty} A_m J_0(\delta_m \varphi), \quad \varphi \in [0, 1], \quad (3.11)$$

where δ_m is the m -th zero of $J_0(\cdot)$ arranged in ascending order. The coefficients A_m are given by [33]

$$A_m = \frac{2}{J_1^2(\delta_m)} \int_0^1 \tau g(\tau) J_0(\delta_m \tau) d\tau. \quad (3.12)$$

Comparison of (3.10) and (3.11) shows that the first M terms in (3.10) can be mapped to the first M terms in (3.11) by establish the following mapping relationship

$$\varphi = \left| \sin\left(\frac{\phi - \phi_0}{2}\right) \right|, \quad (3.13)$$

$$R_m = \delta_m / (2k), \quad (3.14)$$

$$w_m = A_m. \quad (3.15)$$

After the mapping, $F(\phi)$ becomes a truncated Fourier-Bessel series with M terms. If M is large enough then any $g(\varphi)$ expressed as a infinite Fourier-Bessel series can be approximated by $F(\phi)$.

(3.14) indicates that the first M zeros of J_0 function determines the radii of the M rings and this may be inconvenient in practice. An interpolation technique is used by Stearns and Stewart to overcome this restriction. First, the accumulative value of A_m is obtained

$$B_m = \sum_{j=1}^m A_j, \quad m = 1, \dots, M.$$

A set of points $(R_m/\lambda, B_m), m = 1, \dots, M$ is interpolated as shown in Fig. 3.2, where $\lambda = c/f$ and f is the desired operating frequency. If it's desirable to have M equally spaced rings, the curve is resampled at M equally spaced points in the interval of $[0, R_M/\lambda]$. Denoting the new sampling points by $(\tilde{R}_m/\lambda, B'_m), m = 1, \dots, M$, then a new set of weights is obtained by:

$$\begin{aligned} w'_1 &= B'_1 \\ w'_m &= B'_m - B'_{m-1}, \quad m = 2, \dots, M \end{aligned}$$

w'_m now corresponds to the weight of the m -th ring whose radius is given by $\tilde{R}_m = m\tilde{R}_M/M$. Notice that the radius of the M -th ring is kept unchanged with the value of

$$\tilde{R}_M = \delta_M/(2k).$$

This is to ensure that the array dimension remains to be the same. It's shown by Stearns and Stewart that this resampling technique has negligible effect on the resultant array pattern.

3.3 Proposed 3-D Array Pattern Synthesis Method

Stearns and Stewart's pattern synthesis method is only suitable for 2-D beamforming in the x-y plane. In this subsection, we generalize their method to 3-D array pattern synthesis.

Comparison of (3.8) and (3.11) shows that to map the 3-D array pattern given in (3.8) to a truncated Fourier-Bessel series, we only need to modify the mapping in (3.13)

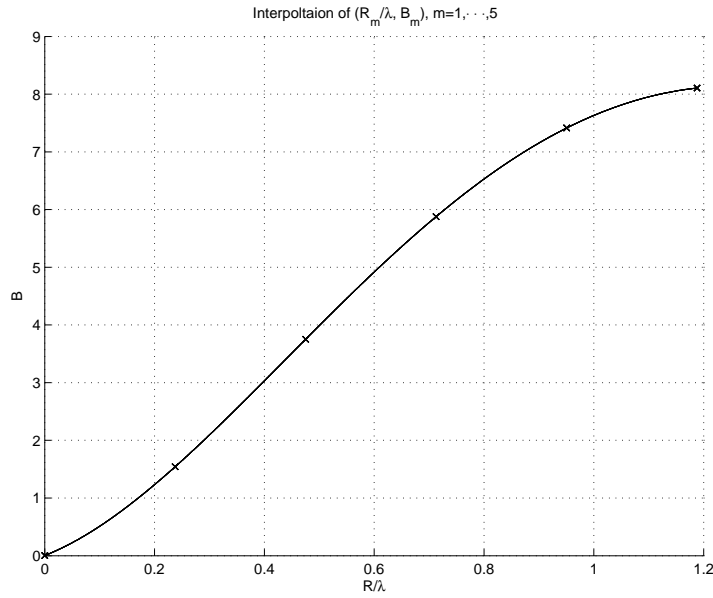


Figure 3.2: Interpolation of $(R_m/\lambda, B_m)$, $m = 1, \dots, 5$

to

$$\rho = 2\varphi, \quad \varphi \in \left[0, \frac{1 + \sin \theta_0}{2}\right] \quad (3.16)$$

and keep the other two mappings specified in (3.14) and (3.15) unchanged, ρ in (3.16) is given in (2.18). The new mapping in (3.16) is examined in more details below.

The desired array pattern function $g(\varphi)$, $\varphi \in [0, 1]$ has the property that $g(0) = 1$ and $g(\varphi) < 1$ when $\varphi > 0$. Thus $\varphi = 0$ corresponds to the main look direction and those relatively large values of φ form the sidelobe region.

The definition of ρ in (2.18) is relisted here as

$$\rho = \sqrt{(\sin \theta \cos \phi - \sin \theta_0 \cos \phi_0)^2 + (\sin \theta \sin \phi - \sin \theta_0 \sin \phi_0)^2}. \quad (3.17)$$

Note that ρ is a function of the azimuth and elevation angle pair (ϕ, θ) , thus through the mapping in (3.16), (ϕ, θ) is mapped to φ , i.e. any point in the 3-D array pattern is mapped to a point in the desired 2-D array pattern. A mapping is considered to be effective if it is able to map the mainlobe region in 3-D array pattern to the mainlobe region in the 2-D array pattern $g(\varphi)$ and the sidelobe region in 3-D array pattern to

the sidelobe region in the 2-D array pattern $g(\varphi)$. An effective mapping can successfully transform the sidelobe control from the 2-D array pattern to the 3-D array pattern.

By rewriting (3.17) as

$$\rho = \sqrt{(\sin \theta - \sin \theta_0)^2 + 2 \sin \theta \sin \theta_0 [1 - \cos(\phi - \phi_0)]},$$

it is easy to see that ρ has a minimum value of 0 when $\phi = \phi_0$ and $\theta = \theta_0$, which is the main look direction. ρ reaches a maximum value of $(1 + \sin \theta_0)$ when $\phi = \phi_0 \pm \pi$ and $\theta = \pi/2$.

Notice that the values of ρ and 2φ in the mapping $\rho = 2\varphi$ may have different ranges depending on the elevation angle θ_0 . The effect of θ_0 on the mapping is examined below by looking at two boundary cases.

(1) When $\theta_0 = \pi/2$, ρ is between 0 and 2 and through the mapping in (3.16), φ is between 0 and 1. Hence the mapping is effective in that sidelobe region in 3-D array pattern is mapped to sidelobe region in 2-D array pattern.

(2) When θ_0 is close to 0, the maximum of ρ is close to 1 and through the mapping in (3.16), the maximum of φ is close to 0.5. This indicates that the whole 3-D array pattern is mapped to the region between 0 and 0.5 in the 2-D array pattern $g(\varphi)$. This suggests that when the elevation angle is close to 0, compression of the desired array pattern function $g(\varphi)$ in φ -axis is necessary to maintain relatively the same mainlobe width and sidelobe level. The exact amount of compression is a parameter to be adjusted in practice.

The 3-D array pattern is symmetric with respect to the x-y plane. It is obvious from (3.17) that $\rho(\phi, \theta) = \rho(\phi, \pi - \theta)$. Hence both points (ϕ, θ) and $(\phi, \pi - \theta)$ will be mapped to the same φ through (3.16) so that $F(\phi, \theta) = F(\phi, \pi - \theta)$. Note that the two mainlobes at (ϕ_0, θ_0) and $(\phi_0, \pi - \theta_0)$ may overlap when θ_0 is close to $\pi/2$.

As an example, Fig. 3.3 shows the relationship between φ and (ϕ, θ) when the look direction is $(\phi_0 = 90^\circ, \theta = 45^\circ)$. In the figure, φ reaches the minimum 0 at

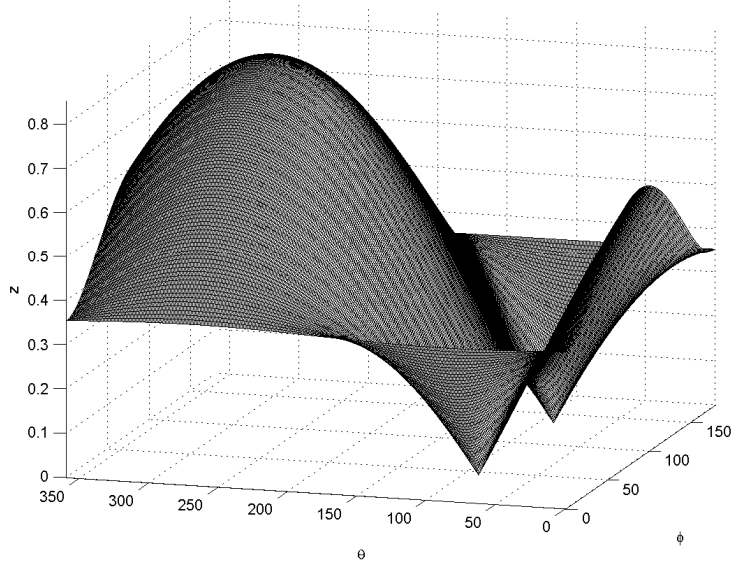


Figure 3.3: Mapping between (ϕ, θ) and φ , φ is represented by z -axis. The look direction is $(\phi_0 = 90^\circ, \theta = 45^\circ)$.

$(\phi_0 = 90^\circ, \theta = 45^\circ)$ and $(\phi_0 = 90^\circ, \theta = 135^\circ)$ corresponding to the look direction and its ambiguity direction. It can be seen that except the small regions surrounding the 2 minima, (ϕ, θ) is mapped to relatively large value of φ , which corresponds to sidelobe region in the desired array pattern $g(\varphi)$.

3.3.1 Requirement on Number of Array Elements

The design of w_m presented above assumes that the discrete CRA has sufficient array elements so that the higher order Bessel function terms in (2.20) can be ignored. Otherwise, the array pattern of a single discrete ring cannot be expanded as Fourier-Bessel series as defined in (3.11) and the performance of the proposed design will degrade. We shall establish the requirement on number of array elements to fulfill the assumption.

From the properties of Bessel function, $J_0(s)$ has a mainlobe at $s = 0$ and decreasing sidelobes toward $s = \infty$. Higher order Bessel functions only have sidelobes and the distances between the origin $s = 0$ and their first sidelobes increase with the order. Fig.

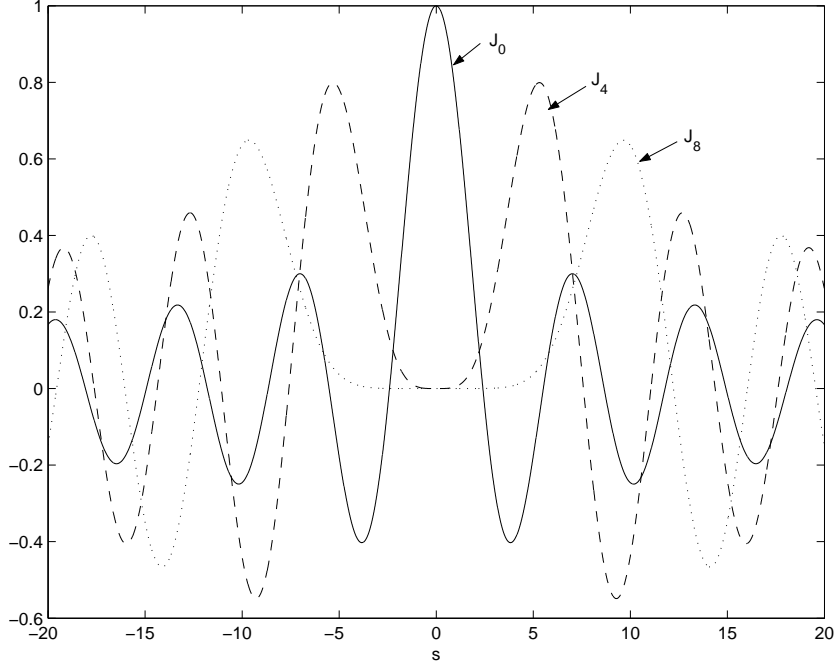


Figure 3.4: Bessel functions: $J_0(s)$ (solid line), $J_4(s)$ (dashed line) and $J_8(s)$ (dotted line).

3.4 shows the plot of $J_0(s)$, $J_4(s)$ and $J_8(s)$; the sidelobes of $J_4(s)$ is more close to the origin $s = 0$ than the sidelobes of $J_8(s)$.

Since ρ has a range of $[0, 1 + \sin \theta_0]$, only portions of the Bessel function terms $J_0(kR_m\rho)$ and $J_{N_m q}(kR_m\rho)$ within this range contribute to the synthesized array pattern. Suppose the location of the first sidelobe of the Bessel function $J_{N_m}(s)$ in (2.20) is at $s = \pm S_{N_m}$. From the property of the Bessel function, S_{N_m} increase with N_m , thus by choosing N_m large enough so that

$$S_{N_m} > kR_m(1 + \sin \theta_0), \quad (3.18)$$

$J_{N_m}(s)$ will hardly affect the sidelobe level of the array pattern. Other higher order Bessel functions $J_{N_m q}(s)$, $q > 1$ will have even less effect on the array pattern.

In summary, the procedure to achieve the desirable prototype array pattern $g(\varphi)$ at an operating frequency f is as follows:

- (1) Set the radius of the m -th ring as in (3.14), and the number of equally spaced

array elements in the ring is chosen large enough to fulfill (3.18),

- (2) Choose the weights within the m -th ring as (3.6),
- (3) Set the weights among different rings according to (3.12) and (3.15),
- (4) Determine the number of rings M so that the relative truncation error

$$\epsilon = \int_0^1 |g(\varphi) - \sum_{m=1}^M A_m J_0(\delta_m \varphi)|^2 d\varphi / \int_0^1 |g(\varphi)|^2 d\varphi \quad (3.19)$$

is within a certain tolerable limit.

3.4 Proposed Inter-ring Weights Design Methods

Suppose a CRA operating at frequency f_0 has been obtained using the method described in Section 3.3. When the incoming frequency deviates from f_0 , the desirable array pattern can no longer be achieved. Usually, the obtained array pattern's mainlobe width varies and the sidelobe level raises. In this section, we derive three methods to design the inter-ring weights at different frequencies that are able to maintain the sidelobe level or/and mainlobe width of the desirable array pattern. These methods use the same array structure within the design frequency range, and can be incorporated into a frequency domain based broadband beamformer.

3.4.1 Method I: Inter-ring Weights Interpolation

In this subsection, a method to design inter-ring weights at different frequencies using interpolation technique is described. The aim of this approach is to achieve similar maximum sidelobe level over a certain input frequency range.

The CRA consists of M rings. An interpolation technique is used by Stearns and Stewart [33] so that the radii can be equally distributed as: $\tilde{R}_m = m\tilde{R}_M/M$, where $\tilde{R}_M = \delta_M/(2k)$. Here we will show that the interpolation technique can be used from a different perspective to offer some flexibility of the beamformer's operating frequency.

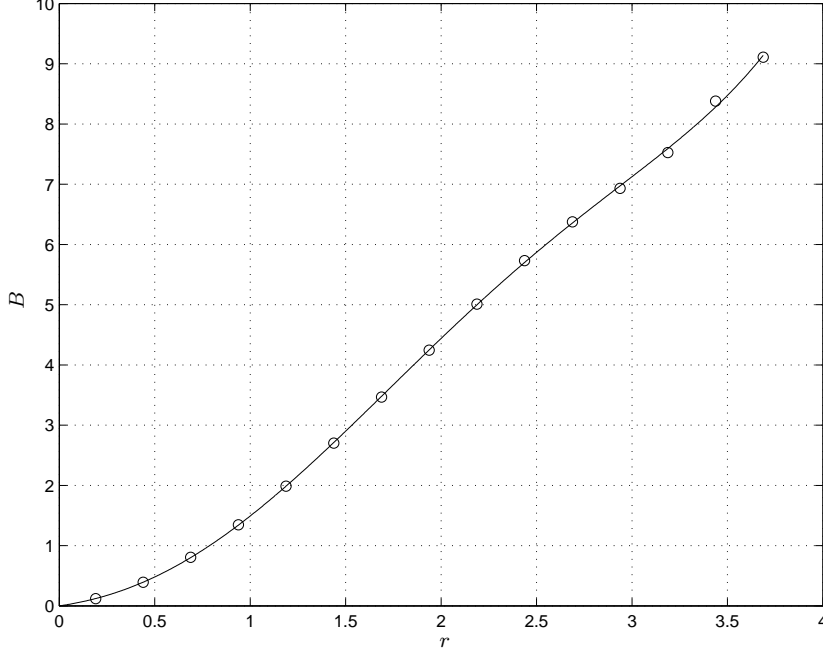


Figure 3.5: Interpolation curve of $(\delta_m/(4\pi), B_m)$, $m = 1, \dots, 15$, obtained by using a $-30dB$ sidelobe level Chebyshev function as the desired array pattern.

First, suppose that up to T coefficients A_m , $m = 1, \dots, T$ are obtained using (3.12), where T is a sufficiently large number, say 15. Note that A_m depends on m through δ_m . The accumulative value of A_m is

$$B_m = \sum_{j=1}^m A_j, \quad m = 1, \dots, T. \quad (3.20)$$

We therefore have T discrete points $(\delta_m/(4\pi), B_m)$, $m = 1, \dots, T$. Interpolating them through B-spline yields a continuous curve as shown in Fig. 3.5.

Putting $k = 2\pi/\lambda_0$ into (3.14) and rearranging it yields $R_m/\lambda_0 = \delta_m/(4\pi)$. Hence the x -coordinate $\delta_m/(4\pi)$ has the physical meaning of the radius R_m normalized by the wavelength λ_0 . If we denote the interpolated continuous curve by $B(r)$, $r \in [0, \delta_T/(4\pi)]$, then r corresponds to an arbitrary radius R normalized by an arbitrary wavelength λ , i.e. $r = R/\lambda$.

Given a certain wavelength λ and radii \tilde{R}_m , $m = 1, \dots, M$, we can sample $B(r)$ at

$$r_{m,\lambda} = \frac{\tilde{R}_m}{\lambda}. \quad (3.21)$$

Then a new set of weights w_m that operates at λ can be obtained through

$$\begin{aligned} w_{1,\lambda} &= B(r_{1,\lambda}) \\ w_{m,\lambda} &= B(r_{m,\lambda}) - B(r_{m-1,\lambda}), \quad m = 2, \dots, M \end{aligned} \quad (3.22)$$

In this process to determine $w_{m,\lambda}$, \tilde{R}_m are always fixed and only λ varies. Note that we have a different set of $w_{m,\lambda}$ for different λ 's. In the following analysis, we will show that within some range of λ , $w_{m,\lambda}$ obtained through resampling $B(r)$ can achieve desired sidelobe level at the corresponding frequency f .

From (3.21), it can be seen that for a given λ the resampling process uses only a portion of the curve, specifically, the curve in the range $[0, \tilde{R}_M/\lambda]$. If an integer P is defined as

$$P = \arg \min_{m=1,2,\dots} \left| \frac{\tilde{R}_M}{\lambda} - \frac{\delta_m}{4\pi} \right| \quad (3.23)$$

then P roughly equals the number of terms we kept in the Fourier-Bessel series expansion in (3.11). Since $\tilde{R}_M/\lambda_0 = \delta_M/(4\pi)$ and $f/f_0 = \lambda_0/\lambda$, (3.23) can be simplified to

$$P = \arg \min_{m=1,2,\dots} \left| \delta_M \frac{f}{f_0} - \delta_m \right|. \quad (3.24)$$

As an example, Fig. 3.6 shows the relationship between P and the frequency ratio f/f_0 for $M = 4, 6, 8, 10$. At $f/f_0 = 1$, $P = M$. Generally speaking, when $f < f_0$, $P \leq M$ and when $f > f_0$, $P \geq M$.

When the operating frequency decreases, i.e., $f < f_0$, the number of terms kept in the Fourier-Bessel expansion (3.11) P is less than M and the truncation error increases. It is expected that there is a lower limit of P , denoted by P_L , at which the truncation error is no longer acceptable. The corresponding frequency of keeping P_L terms is roughly equal to $f_0 \delta_{P_L} / \delta_M$ from (3.24). On the other hand, when $f > f_0$, the number of terms we kept in the Fourier-Bessel expansion should be greater than M . However there are only M rings and we are only able to sample the curve at M locations, which results in distortion in the array pattern through not keeping enough terms in (3.11). Hence

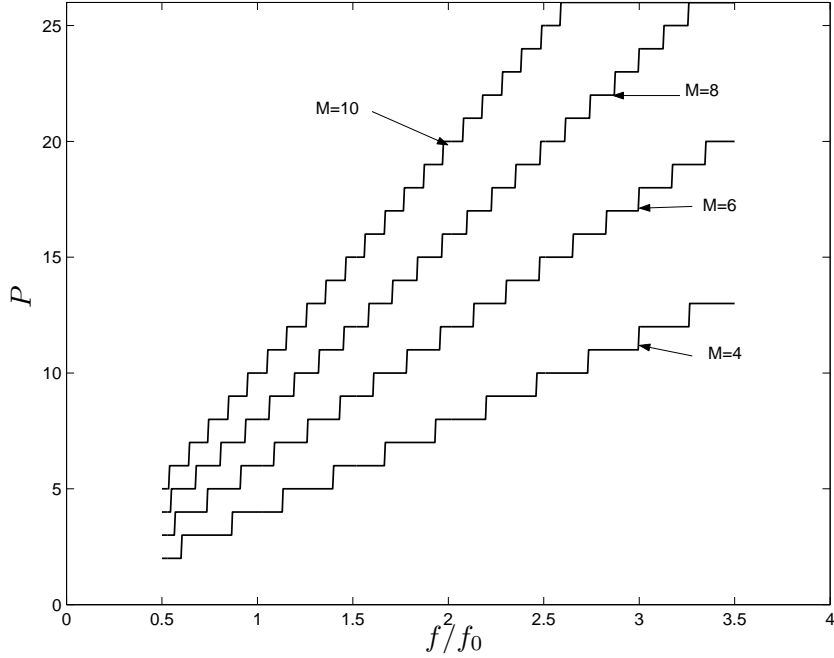


Figure 3.6: Relationship between P and (f/f_0) for $M = 4, 6, 8, 10$.

there is an upper limit of P , denoted by P_U , at which the distortion introduced by not keeping enough terms is no longer acceptable. The corresponding frequency of keeping P_U terms, from (3.24), is roughly equal to $f_0 \delta_{P_U} / \delta_M$. Thus the range of the operating frequency is given by

$$f \in \left[\frac{\delta_{P_L}}{\delta_M} f_0, \frac{\delta_{P_U}}{\delta_M} f_0 \right]. \quad (3.25)$$

Within this frequency range, using the weights $w_{m,\lambda}$ obtained through (3.22) can achieve the desired sidelobe level in the array pattern, as will be demonstrated in Section 3.6. The exact values of P_L and P_U depend on the configuration of the array and the acceptable sidelobe level.

In Section 3.3.1, we derived the requirement on the number of array elements on a ring. In Method I, this requirement needs to be modified to accommodate the broadened frequency range.

The derivation of (3.18) assumes that the m -th ring is associated with the m -th term in the Fourier-Bessel series. However, this may no longer be the case after applying

Method I. Denote the broadened frequency range centered at f_0 by $[f_1, f_2]$, which can also be expressed equivalently by their wavelength as $[\lambda_2, \lambda_1]$. For an operating frequency with wavelength $\lambda \in [\lambda_2, \lambda_1]$, the m -th ring is roughly associated with the P_m th term in the Fourier-Bessel series, where P_m is determined by

$$P_m = \arg \min_{p=1,2,\dots} \left| \frac{\tilde{R}_m}{\lambda} - \frac{\delta_p}{4\pi} \right|. \quad (3.26)$$

P_m is dependent on λ . A larger value of P_m implies that the m -th ring is associated with a term of higher order in the Fourier-Bessel series and resultantly more array elements are required on the m -th ring as indicated by (3.18). By setting $\lambda = \lambda_2$, the maximum value of P_m is obtained

$$P_{m,max} = \arg \min_{p=1,2,\dots} \left| \frac{\tilde{R}_m}{\lambda_2} - \frac{\delta_p}{4\pi} \right|. \quad (3.27)$$

Thus when the number of array elements N_m on the m -th ring satisfies

$$S_{N_m} > \delta_{P_{m,max}}, \quad (3.28)$$

the discrete array pattern can be well approximated by $J_0(s)$ over the broadened frequency range $[f_1, f_2]$ and the proposed design method can be applied.

3.4.2 Method II: Inter-ring Weights Design Using MMSE Criterion

Method I involves two types of approximations in the process of synthesizing the array pattern. First, the desired array pattern is expressed as an infinite Fourier-Bessel series in (3.11), while the synthesized array pattern is a truncated Fourier-Bessel series of M terms corresponding to M rings. Thus there is a truncation error between the desired and synthesized array pattern. The truncation error is negligible when M is large. When M is small, the truncation error will be reflected in the array pattern, resulting in raised sidelobe level.

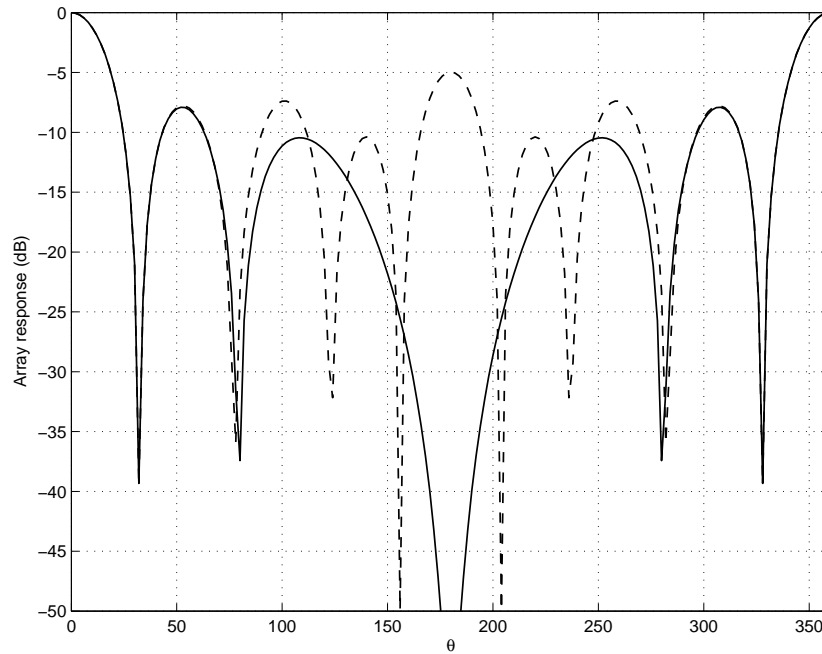


Figure 3.7: Beam pattern of a discrete ring: array pattern generated using only J_0 term (solid line), actual array pattern (dashed line).

Second, when deriving the weights w_m for the discrete circular ring array, we assume that there are enough array elements on a ring so that the discrete array pattern in (2.20) can be approximated by only the J_0 term. If the number of array elements is less than required, then the higher order Bessel function terms cannot be ignored and they will increase the sidelobe level. Fig.3.7 shows the actual array pattern for a discrete ring array composed of less than required number of array elements, together with the array pattern approximated by only the J_0 term. The difference between them is obvious and significant. In such case, using the previous method will generate some unwanted high sidelobe in the synthesized array pattern.

The degradation accompanying the two types of approximations can be mitigated by maintaining the number of rings and the number of array elements on each ring above some minimum values. In some applications, the required number of array elements can be large, which is costly not only in deployment but also in real-time data

processing. Thus reducing the elements without degrading the array pattern is a desirable design goal. However, this is difficult to achieve using the previous proposed design method since the approximation error is simply ignored and left uncontrolled in the design process.

In this section, we present a pattern synthesis method based on the MMSE criterion, which takes the two kinds of degradation into account and offers some error control over different spatial regions of a array pattern. The new method can serve as an alternative design method for applications where the number of array elements is a constraint.

Denote the desired array pattern as $g(\varphi), \varphi \in [0, (1 + \sin \theta_0)/2]$, where ϕ_0 is the elevation angle of the main look direction. The array pattern of the m -th ring is $F_m(\phi, \theta) = F_m(\varphi), \varphi \in [0, (1 + \sin \theta_0)/2]$, where the pair (ϕ, θ) is converted to φ through (2.18) and (3.16). The synthesized pattern $\hat{g}(\varphi)$ is formed as a weighted sum of the array pattern of each ring:

$$\hat{g}(\varphi) = \sum_{m=1}^M w_m F_m(\varphi), \varphi \in [0, (1 + \sin \theta_0)/2]. \quad (3.29)$$

To simplify the design procedure, the array pattern of each ring is evaluated at D locations, where D is sufficiently large, within $[0, (1 + \sin \theta_0)/2]$ that are denoted by $\varphi_d, d = 1 \dots D$. This process results in D linear equations

$$\hat{g}(\varphi_d) = \sum_{m=1}^M w_m F_m(\varphi_d), d = 1 \dots D. \quad (3.30)$$

The D linear equations can be expressed in matrix form as

$$\hat{\mathbf{G}} = \mathbf{F}\mathbf{w} \quad (3.31)$$

where $\hat{\mathbf{G}} = [\hat{g}(\varphi_1), \hat{g}(\varphi_2), \dots, \hat{g}(\varphi_D)]^T$, $\mathbf{F} = [\mathbf{f}_1, \mathbf{f}_2, \dots, \mathbf{f}_M]$ with $\mathbf{f}_m = [F_m(\varphi_1), F_m(\varphi_2), \dots, F_m(\varphi_D)]^T$, and $\mathbf{w} = [w_1, w_2, \dots, w_M]^T$ is the unknown weight vector.

The error vector between desired pattern \mathbf{G} and synthesized pattern $\hat{\mathbf{G}}$ is

$$\mathbf{e} = \mathbf{G} - \hat{\mathbf{G}} = \mathbf{G} - \mathbf{F}\mathbf{w}, \quad (3.32)$$

and the weighted energy of the error is formed as

$$E = \mathbf{e}^H \mathbf{K} \mathbf{e} = (\mathbf{G} - \mathbf{F}\mathbf{w})^H \mathbf{K} (\mathbf{G} - \mathbf{F}\mathbf{w}) \quad (3.33)$$

where \mathbf{K} is a positive definite and Hermitian $D \times D$ weighting matrix that emphasizes error in certain spatial regions. A typical choice of \mathbf{K} is a diagonal matrix as

$$\mathbf{K} = \begin{bmatrix} k_{11} & 0 & \dots & 0 \\ 0 & k_{22} & \dots & 0 \\ \vdots & \vdots & \ddots & \vdots \\ 0 & \dots & 0 & k_{DD} \end{bmatrix}.$$

where $k_{dd} > 0, d = 1, \dots, D$. If the diagonal elements in the upper left-hand corner has larger values than the others, then the synthesis error in the mainlobe region will receive more emphasis and therefore more reduction. If the goal is to reduce mainly the synthesis error in the sidelobe region, the diagonal elements in the lower right-hand corner should be set to larger values.

To make the design more general, linear constraints can be imposed in finding \mathbf{w} . The optimum weight vector \mathbf{w} in the MMSE sense is then chosen by minimizing error energy E while at the same time satisfying a set of Q linear constraints in the form of $\bar{\mathbf{C}}^H \mathbf{w} = \mathbf{b}$, where $\bar{\mathbf{C}}$ is a $M \times Q$ constraint matrix and \mathbf{b} is a $Q \times 1$ vector of the constraint values. If M weights are available, up to $M - 1$ constraints can be specified. A commonly used constraint is the unit gain constraint at the look direction of the desired signal.

The optimization problem can be described as

$$\mathbf{w}_{opt} = \arg \min E \quad \text{subject to } \bar{\mathbf{C}}^H \mathbf{w} = \mathbf{b}.$$

By formulating the pattern synthesis problem this way, the degradation described previously can be assimilated into the synthesis error. This is because (3.29) explicitly uses M rings and $F_m(\varphi)$ contains not only the J_0 term but also higher order Bessel function terms in (2.20).

This constrained optimization problem can be solved by using the method of *Lagrange multipliers*. The *Lagrangian* of this problem is

$$\mathcal{L}(\mathbf{w}, \boldsymbol{\beta}) = (\mathbf{G} - \mathbf{F}\mathbf{w})^H \mathbf{K}(\mathbf{G} - \mathbf{F}\mathbf{w}) + (\mathbf{b}^H - \mathbf{w}^H \bar{\mathbf{C}}) \boldsymbol{\beta} \quad (3.34)$$

where $\boldsymbol{\beta} = [\beta_1, \beta_2, \dots, \beta_Q]^T$ is the *Lagrange multiplier* vector. Setting $\partial \mathcal{L}(\mathbf{w}, \boldsymbol{\beta}) / \partial \mathbf{w}^* = 0$ and solving \mathbf{w} gives

$$\mathbf{w}_{opt} = (\mathbf{F}^H \mathbf{K} \mathbf{F})^{-1} \mathbf{F}^H \mathbf{K} \mathbf{G} + (\mathbf{F}^H \mathbf{K} \mathbf{F})^{-1} \bar{\mathbf{C}} \boldsymbol{\beta}. \quad (3.35)$$

Using $\bar{\mathbf{C}}^H \mathbf{w} = \mathbf{b}$, $\boldsymbol{\beta}$ is obtained to be

$$\boldsymbol{\beta} = [\bar{\mathbf{C}}^H (\mathbf{F}^H \mathbf{K} \mathbf{F})^{-1} \bar{\mathbf{C}}]^{-1} [\mathbf{b} - \bar{\mathbf{C}}^H (\mathbf{F}^H \mathbf{K} \mathbf{F})^{-1} \mathbf{F}^H \mathbf{K} \mathbf{G}]. \quad (3.36)$$

Note that the solution (3.35) and (3.36) is at a given frequency since \mathbf{F} is dependent on frequency. Hence \mathbf{w}_{opt} is different at different operating frequencies.

3.4.3 Method III: Inter-ring Weights Design with Frequency Invariant Property

Frequency invariant(FI) array pattern design is desirable for broadband signal acquisition and it has also been used in high resolution broadband signal DOA estimation [1,89,90]. FI design based on linear array has been studied in [90–93]. The technique in [90] relies on the beamspace and the Jacobi-Anger expansion of the array pattern for wideband range and bearings estimation. [91] and [93] use a technique similar to [59] where a fixed filter is applied to compensate for the frequency dependence to create FI beampatterns for linear arrays. In the case of an arbitrary array, Ward *et al.* [92,94] adjust the sensor positions to achieve FI array pattern. For a single ring uniform circular array, Chan and Pun [59] utilize phase mode processing and filtering to obtain FI design. We take a different approach by using multiple concentric rings together with a careful choice of the ring radii to achieve the FI property. The FI design is based on the

deterministic CRA method described in Section 3.3, and improves significantly in terms of FI property of the array pattern.

Suppose a narrowband CRA beamformer having a desirable array pattern at frequency f_0 has been obtained using the method from Section 3.3. At another operating frequency f different from f_0 , the synthesized array pattern degrades. One could re-design the inter-ring weights at the new operating frequency to achieve the same desirable array pattern. However, since the ring radii in the CRA are determined by $R_m = \delta_m/(2k) = \delta_m c/(4\pi f)$, where c is the signal propagation speed, they are dependent on the frequency. Hence the new set of weights for f will require rings of different radii than the one that operates at f_0 . Having a completely different CRA at different frequencies is neither practical nor cost effective. In the following, we shall derive a technique to maintain FI array pattern over a range of frequencies for the given array structure designed at f_0 .

By design with operating frequency at f_0 , the radii are $R_m = \delta_m c/(4\pi f_0)$ and the inter-ring weights are $w_{m,f_0} = A_m$ given in (3.12). The array pattern $F_{f_0}(\phi, \theta)$ thus approximates the desirable array pattern $g(\varphi)$, i.e,

$$F_{f_0}(\phi, \theta) |_{\rho=2\varphi} = \tilde{g}(\varphi) = \sum_{m=1}^M A_m J_0(\delta_m \varphi). \quad (3.37)$$

where $\tilde{g}(\varphi)$ denotes the truncated Fourier-Bessel series.

At a different operating frequency f , where $f < f_0$, the array pattern from the same array structure R_m and inter-ring weights w_{m,f_0} is, from (3.8),

$$F_F(\phi, \theta) = \sum_{m=1}^M w_{m,f_0} J_0\left(\frac{2\pi R_m}{\lambda} \rho\right) = \sum_{m=1}^M A_m J_0\left(\delta_m \frac{f}{f_0} \varphi\right) \quad (3.38)$$

where (3.16) and (3.14) have been used.

Comparing (3.38) with (3.37) indicates that

$$F_F(\phi, \theta) |_{\rho=2\varphi} = \tilde{g}\left(\frac{f}{f_0} \varphi\right) \quad (3.39)$$

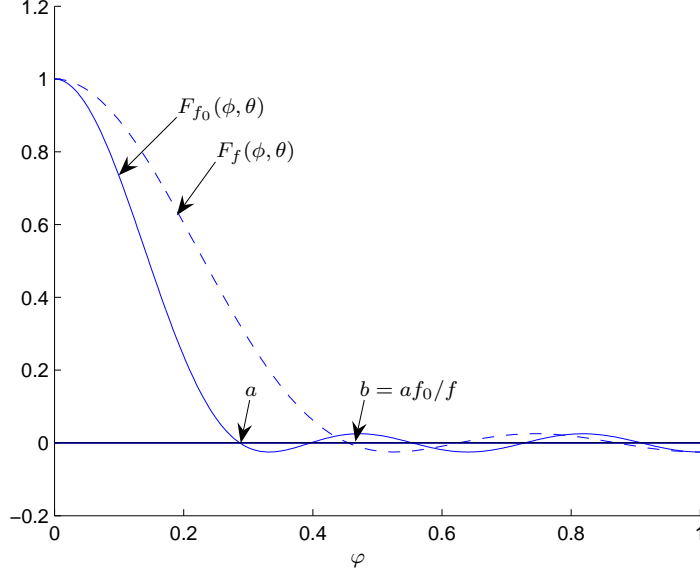


Figure 3.8: Array pattern $F_{f_0}(\phi, \theta)$ and $F_f(\phi, \theta)$, where $\varphi = \rho/2$. a and b denote the first zero crossing points of $F_{f_0}(\phi, \theta)$ and $F_f(\phi, \theta)$ respectively, $b = af_0/f$.

Since $\tilde{g}(\varphi)$ is defined in the range $[0, 1]$, (3.39) indicates that the array pattern at frequency $f < f_0$ is a stretched version of $\tilde{g}(\varphi)$ and therefore creates undesired widening of the mainlobe. An example is shown in Fig. 3.8 to illustrate this stretching effect.

In order to achieve the same desirable array pattern at a lower frequency, we create a pre-compressed desirable array pattern, i.e. $g_f(\varphi) = g(C_f\varphi)$, where $C_f = f_0/f$, and use $g_f(\varphi)$ instead of $g(\varphi)$ to obtain the inter-ring weights through (3.12). Note that in order to obtain $g_f(\varphi)$ in the range of $\varphi \in [0, 1]$, additional definition of $g(\varphi)$, $\varphi \in (1, C_f]$ is necessary. In practice, $g(\varphi)$, $\varphi \in (1, C_f]$ can be set to a desirable sidelobe level. As a result, we have from (3.39)

$$F_F(\phi, \theta) |_{\rho=2\varphi} = \tilde{g}_f\left(\frac{f}{f_0}\varphi\right) = \tilde{g}\left(C_f\frac{f}{f_0}\varphi\right) = \tilde{g}(\varphi) \quad (3.40)$$

and therefore the same array pattern can be maintained.

The above method cannot maintain the desirable array pattern at arbitrarily low frequencies. When the frequency decreases, the prototype array pattern $g(\varphi)$ needs to be compressed more and it becomes shaper in shape. Hence the coefficients of expansion

A_m in (3.12) become larger in amplitude for larger m . Note that we only keep the first M terms in the Fourier-Bessel series to approximate the desirable array pattern. Keep compressing $g(\varphi)$ will eventually increase $|A_m|$, for $m > M$, such that the truncation error will no longer be negligible. Thus there is a lower frequency limit that can achieve the same array pattern using the fixed array structure. It is determined by the number of rings we use in the CRA.

Throughout the derivation, we assume f_0 is the highest frequency that the CRA operates. The highest frequency is actually determined by the number of array elements on the rings. Rearranging (3.18) yields

$$f_0 < \frac{cS_{N_m}}{4\pi R_m}, \quad (3.41)$$

where $\theta_0 = \pi/2$ is assumed to obtain the least upper bound of f_0 . The highest frequency must satisfy this condition to avoid the distortion introduced by those higher order Bessel function terms in (2.20), S_{N_m} is the location of the first maximum of $J_{N_m}(s)$. The more the array elements on each ring the larger S_{N_m} becomes, and from (3.41) the higher the frequency can be. However, there is a practical limit on the highest frequency in which the proposed method can achieve. This is because the ring radius and the coupling effect limit the number of array elements that can be allocated to a ring.

If the frequency band broadening technique developed here does not provide enough frequency range coverage, the compound ring structure method can be utilized on top of the proposed band broadening technique to extend the coverage of frequency range [95].

The proposed beamformer operates on broadband signal as follow:

- (i) separate the signals received at each sensor elements into segments using a window,
- (ii) perform FFT on the data segments,
- (iii) pass each FFT components through the proposed narrowband beamformers designed to have the same array pattern,
- (iv) apply inverse FFT to the outputs of the narrowband beamformers to obtain the

beamformed signal in time-domain. Note that the size of FFT is equal to the length of the tapped-delay line for each array element.

3.4.4 Comparison of Method I, II, III

Method I and II are similar in that they aim to control the sidelobe level but not the mainlobe within a frequency range. Comparing these two, Method II has better sidelobe level control performance at the price of higher computational complexity. This is because in Method II, the MMSE solution for \mathbf{w} is more complex and it needs to be computed at all operating frequencies during the design stage, while in Method I all the weights in one subband can be obtained through sampling the same interpolated curve. Thus Method II is more favorable for applications where there are a limited number of array elements and the control of sidelobe is more important than the design complexity.

Method III yields the best performance among the three in terms of sidelobe level and mainlobe control. However, it requires more number of rings in order maintain tolerable truncation error in the Fourier-Bessel series.

3.5 Broadband Beamforming Implementation

3.5.1 Frequency Domain Broadband Beamformer

The proposed method assumes the incoming signals are narrow-band. For broadband beamforming, the incoming signals can be decomposed into many narrow-bands and processed by narrow-band beamformers respectively. The final output is formed by combining outputs from those narrow-band beamformers.

A commonly used method in broadband beamforming is to transform the broadband

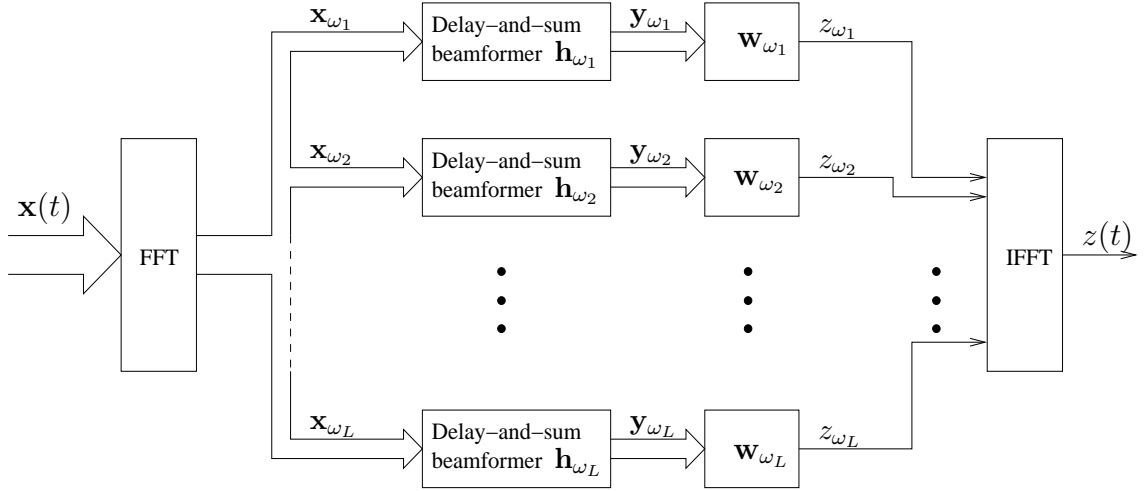


Figure 3.9: Frequency domain broadband beamformer based on FFT.

signal to frequency domain using FFT, the frequency domain data are then processed using narrow-band beamforming techniques. Such processing requires the design of narrow-band beamformers at all the frequency bins. Using our proposed band-broadening technique, we can derive weights to achieve desired sidelobe level at arbitrary frequency by sampling a prescribed curve, which makes it convenient to design a frequency domain broadband beamformer based on FFT. Fig. 3.9 shows the diagram of such a broadband beamformer. The received signal $\mathbf{x}(t)$ is first transformed to frequency domain using FFT. Denote the received signal vector in frequency domain by \mathbf{x}_{ω_l} , where ω_l is the angular frequency at the l th frequency bin. At a particular frequency ω_l , the received data \mathbf{x}_{ω_l} is first processed by a narrow-band delay-and-sum beamformer \mathbf{h}_{ω_l} to form the intermediate output \mathbf{y}_{ω_l} , which is a $M \times 1$ vector containing the outputs from each ring. Using the inter-ring weights \mathbf{w}_{ω_l} , the outputs from each ring are combined to yield the output z_{ω_l} . Finally, the frequency domain output is transformed to time domain using IFFT.

3.5.2 Nested Array Design

The frequency range provided by the previous three methods may not be wide enough to cover the entire frequency range of interest in some applications. To further extend the frequency range of the array, we assimilate the nested array [96] design used for linear array.

The nested CRA is composed of many concentric rings grouped into different subarrays, each of which is dedicated to a subband of the entire frequency range. The proposed methods will be used in each subarray to cover a corresponding subband. By properly grouping, rings can be reused among different subarrays to improve efficiency. This is illustrated by an example in Fig. 3.10, in which only the radii of the rings are shown. The exemplary array has 6 rings in total. It consists of 2 subarrays as indicated by the grouping of the radii in the figure. Each subarray has 4 rings. The size of the *2nd* subarray is 2 times that of the *1st* one, so that the center frequency of the *2nd* subarray is half of that of the *1st* subarray. Ring 2 and Ring 4 are shared by the two subarrays. Only half of the elements in these two rings are used in the *2nd* subarray.

Nested array design requires the rings in each subband have equally spaced ring radii. Note that Method I and II are derived for CRAs possess such structure, while Method III is not. However, Method III can also be extended to equally spaced ring structure using Stearns and Stewart's interpolation technique described in 3.2, the details are omitted here.

3.5.3 Linear Constrained Beamformer with Desired Beampattern

In Section 3.4, we derived three methods to control the sidelobe or/and mainlobe in the array pattern of a CRA. Such beamformer is expected to have satisfactory performance

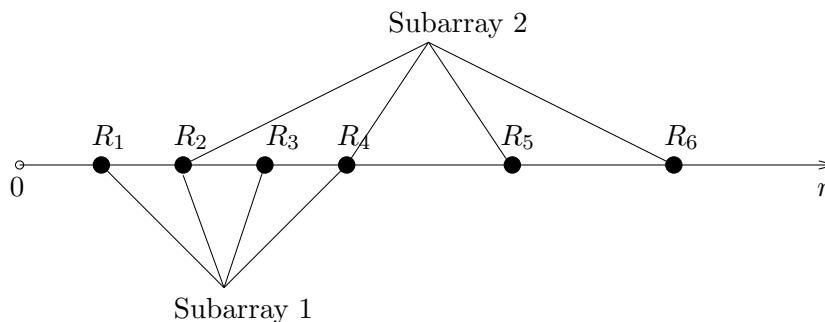


Figure 3.10: CRA using nested array structure. $R_m, m = 1, \dots, 6$ normalized with respect to R_1 is: $[1 \ 2 \ 3 \ 4 \ 6 \ 8]$.

when noise and interference is at moderate level. However, when there are strong interferences, the fixed sidelobe level may not achieve enough attenuation of the interferences and resultantly the remaining interferences are still at a hazardous level. Decreasing the overall sidelobe level to a sufficiently low value to cancel the strong interference is not a practical solution since the mainlobe will be widened accordingly, not mentioning that sometimes there are physical constraints to do so.

In the review of modern beamforming techniques in Section 2.2.2, we introduced the Linear Constrained Minimum-Variance (LCMV) beamforming technique. LCMV beamformer is known to be very effective in removing strong interference. When the DOA of an interference is known, the LCMV beamformer can add a linear constraint to explicitly specify the gain at the direction of the interference to be zero or other sufficiently small value. The obtained LCMV solution will generate a deep null in the array pattern to remove the interference while the sidelobe level surrounding the null is only slightly raised.

Although LCMV is effective in removing interference, it cannot replace conventional methods that can specify the array pattern to a desired one. Theoretically, for an N -element array, it is possible to use as many as N linear constraints to specify the whole array pattern, but it would be very computationally inefficient to implement a LCMV in this way if N is large because the inverse of large size matrices are involved. In most

cases, the LCMV contains only a few constraints to specify the gains and the main look direction, directions at interferences and other linear constraints to increase the robustness of the LCMV beamformer. In such case, most of the sidelobe region is not explicitly specified in the LCMV, which results in relatively high sidelobe level in the array pattern, especially in those regions close to the mainlobe.

In [88], Griffiths and Buckley proposed a method to control the quiescent pattern in linearly constrained adaptive arrays. Their method can be used to incorporate our deterministic design of the weights of a CRA into the framework of the LCMV beamformer. The result is a deterministic beamformer that has desired overall sidelobe level and deep nulls only in directions of the interferences. The advantage in combining the LCMV design with our design is obvious, it eliminates some of the inherent limitations in both designs we discussed earlier and therefore opens up more applications. The combined design method is briefly summarized below.

We first describe the LCMV form of the K -element CRA. The linear constraints are specified as $\mathbf{C}^H \mathbf{v} = \mathbf{b}$, where \mathbf{C} is a $K \times Q$ constraint matrix, \mathbf{v} is the $K \times 1$ weight vector for array elements, and \mathbf{b} is the $Q \times 1$ constraint value vector. The solution to the LCMV optimization problem is given in (2.11) in Section 2.2.2.

Using our proposed methods in Section 3.4, the inter-ring weights \mathbf{w} is obtained. Combining \mathbf{w} with the intra-ring delay-and-sum weights \mathbf{h} in the manner given in (3.5) yields the weights for each array element \mathbf{v}_0 . \mathbf{v}_0 obtained this way may not satisfy the linear constraints of the LCMV. A vector $\bar{\mathbf{v}}_0$ that is the closest to \mathbf{v}_0 in the least-squares sense and also satisfies the linear constraints is found through solving the following linearly constrained minimization problem [88]:

$$\bar{\mathbf{v}}_0 = \min_{\bar{\mathbf{v}}_0} \{(\bar{\mathbf{v}}_0 - \mathbf{v}_0)^H (\bar{\mathbf{v}}_0 - \mathbf{v}_0)\} \quad \text{subject to } \mathbf{C}^H \bar{\mathbf{v}}_0 = \mathbf{b}$$

The solution is

$$\bar{\mathbf{v}}_0 = [\mathbf{I} - \mathbf{C}(\mathbf{C}^H \mathbf{C})^{-1} \mathbf{C}^H] \mathbf{v}_0 + \mathbf{v}_q \quad (3.42)$$

where \mathbf{I} is a $K \times K$ identity matrix and \mathbf{v}_q is the quiescent solution given by $\mathbf{v}_q = \mathbf{C}(\mathbf{C}^H\mathbf{C})^{-1}\mathbf{b}$.

Finally, the constrained matrix \mathbf{C} and constrained value vector are modified respectively to [88]

$$\bar{\mathbf{C}} = [\mathbf{C}, \bar{\mathbf{v}}_s] \quad (3.43)$$

$$\bar{\mathbf{b}} = \begin{bmatrix} \mathbf{b} \\ \bar{\mathbf{v}}_0^H \bar{\mathbf{v}}_s \end{bmatrix} \quad (3.44)$$

where $\bar{\mathbf{v}}_s = \bar{\mathbf{v}}_0 - \mathbf{v}_q$.

The quiescent solution obtained under the modified linear constraints can generate a array pattern similar to the one obtained using our proposed methods, which has the desired sidelobe level. Notice that only one additional linear constraint needs to be added to yield the desired array pattern in the LCMV beamformer. Nulls can be added in the array pattern through other linear constraints.

3.6 Experimental Results

The proposed methods can be applied for electromagnetic and acoustic applications. In this section, we consider the design of a CRA for acoustic signal acquisition [95, 97] to demonstrate Method I, II, III respectively.

3.6.1 Method I

An exemplary CRA of 9 equally spaced rings, grouped into 2 subarrays, are used to cover an input frequency range from $500Hz$ to $4kHz$. The radii of the 9 rings normalized with respect to the first one are: [1, 2, 3, 4, 5, 6, 8, 10, 12] and the radius of the largest ring is $0.475m$. The *1st* subarray consists of ring 1 to ring 6. The *2nd* subarray consists of rings 2, 4, 6 from the *1st* subarray and rings 7, 8, 9. The *1st* and *2nd* subarrays originally

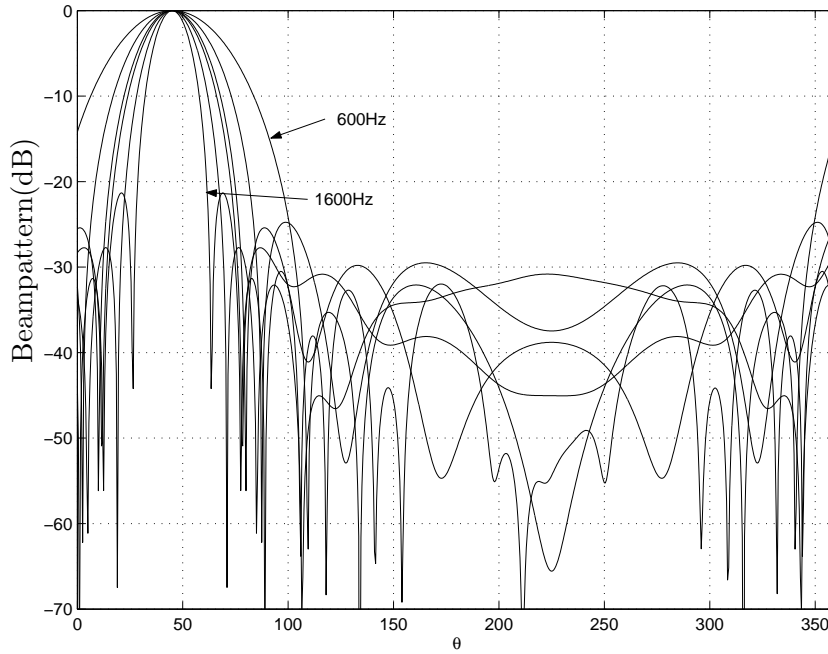


Figure 3.11: 2-D Beampatterns in the 2nd subarray: curves starting from the outside one are beampatterns at frequencies: $600Hz$, $800Hz$, $1000Hz$, $1200Hz$, $1400Hz$ and $1600Hz$ respectively. The main look direction in this 2-D array pattern is $\phi = 45^\circ$

operate at $2000Hz$ and $1000Hz$, and intend to cover a frequency range of $500 - 1800Hz$ and $1800 - 4000Hz$ respectively after band-broadening.

A Chebyshev function with $-30dB$ sidelobe level is used as the desired array pattern. Using (3.28), the number of elements on the 6 rings of the 1st subarray is found to be : $[7, 14, 19, 24, 30, 36]$. Some redundancy of elements are allowed on rings 2, 4, 6 for the purpose of reusing them in the 2nd subarray. Specifically, only every other elements on rings 2, 4, 6 are reused in the 2nd subarray. This is to ensure the two subarrays have roughly the same amount of elements. The number of elements in 2nd subarray is distributed as: $[7, 12, 18, 24, 28, 32]$. The total number of elements is 214, among which 130 are in the 1st subarray, 121 are in the 2nd subarray.

Assume that the arriving direction of the signal is $(\phi_0 = 45^\circ, \theta_0 = 60^\circ)$. For the purpose of illustration, the surface $\theta = 60^\circ$ cutting through the look direction is presented as a sample of the 3-D array pattern. The beampatterns for some sampled frequencies in

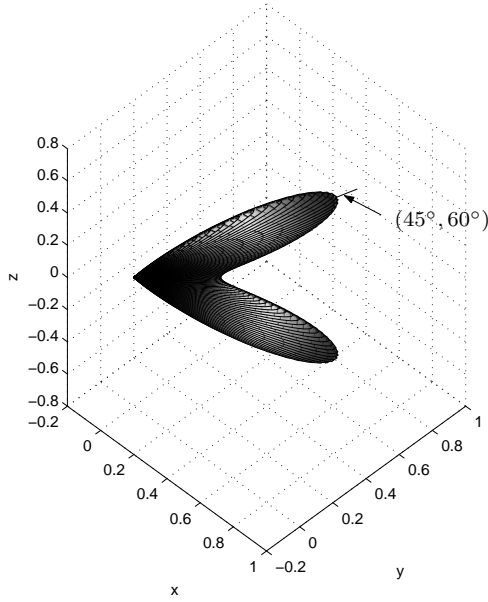


Figure 3.12: 3D Beampattern at $1600Hz$ in the 2nd subarray, the main look direction is $(\phi_0 = 45^\circ, \theta_0 = 60^\circ)$.

the 2nd subarray are shown in Fig. 3.11, where the curves, starting from the outside one, are beampatterns at $600Hz$, $800Hz$, $1000Hz$, $1200Hz$, $1400Hz$ and $1600Hz$ respectively. The beampatterns for another subarray are nearly identical. As can be seen from the figure, the beampatterns fulfill the design objective of $-30dB$ sidelobe level. In the experiment, similar sidelobe level is observed in the 3-D array pattern except the region between the 2 ambiguity DOAs, where the sidelobe is raised due to the overlapping of the mainlobes at the two ambiguity DOAs. An exemplary 3-D array pattern at frequency $1600Hz$ is also shown in Fig. 3.12.

We then use computer simulated received array signal to test the performance of the beamformer obtained above. Two signal scenarios are assumed to generate the received array signal. In the first scenario, the received array signal contains a desired speech signal from the direction $(\phi_0 = 45^\circ, \theta_0 = 60^\circ)$ and ambient noise in the background. The signal-to-noise ratio (SNR) is $-5dB$. The noise starts to appear at about $t = 0.4s$. The processing results are shown in Fig. 3.13. From the figure, it can be seen the ambient noise level in the beamformer output is greatly reduced.

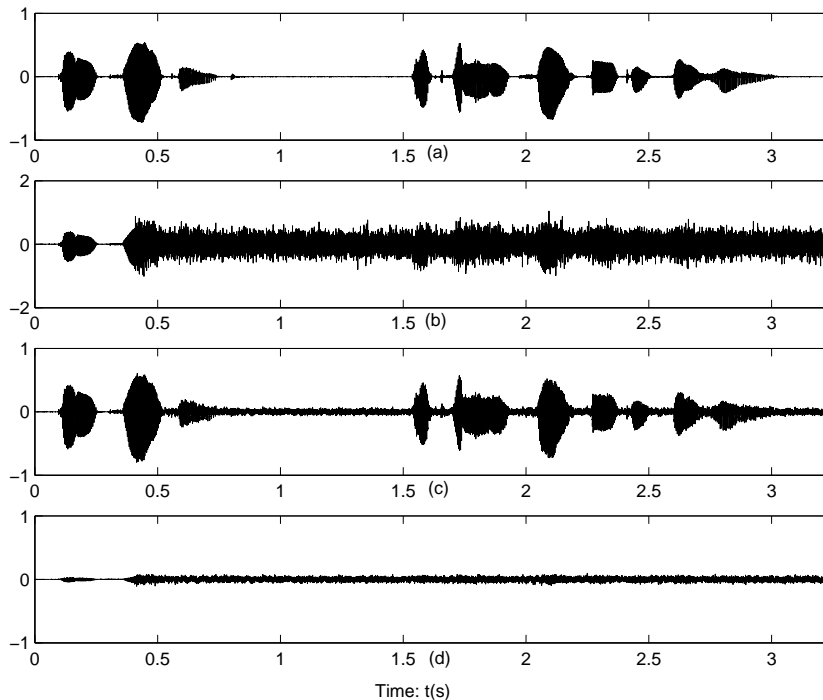


Figure 3.13: Processing results for scenario 1: (a) Desired signal $s(t)$; (b) Received noisy signal in one channel; (c) Beamformer output $z_1(t)$; (d) Error signal: $e_1(t) = z_1(t) - s(t)$.

In the second scenario, the received array signal contains a desired speech signal from the direction $(\phi_0 = 45^\circ, \theta_0 = 60^\circ)$, two narrow-band interferences and ambient noise in the background. The first interference is a narrow-band signal with central frequency $1000Hz$ from the direction $(\phi_0 = 180^\circ, \theta_0 = 60^\circ)$ and the signal-to-interference ratio (SIR) is $-30dB$. The second interference is a narrow-band signal with central frequency $2400Hz$ from the direction $(\phi_0 = 135^\circ, \theta_0 = 80^\circ)$ and SIR is $-25dB$. The SNR is $0dB$. The interferences and noise start to appear at about $t = 0.4s$. The processing results are shown in Fig. 3.14. The beamformer output in (c) shows the two interferences and ambient noise has been effectively removed, which is as expected since the sidelobe level is designed to be $-30dB$.

Finally, to demonstrate the performance of the combined design in Section 3.5.3, we compose a third scenario, in which the received array signal contains a desired speech signal from the direction $(\phi_0 = 45^\circ, \theta_0 = 60^\circ)$, a interference speech signal for the

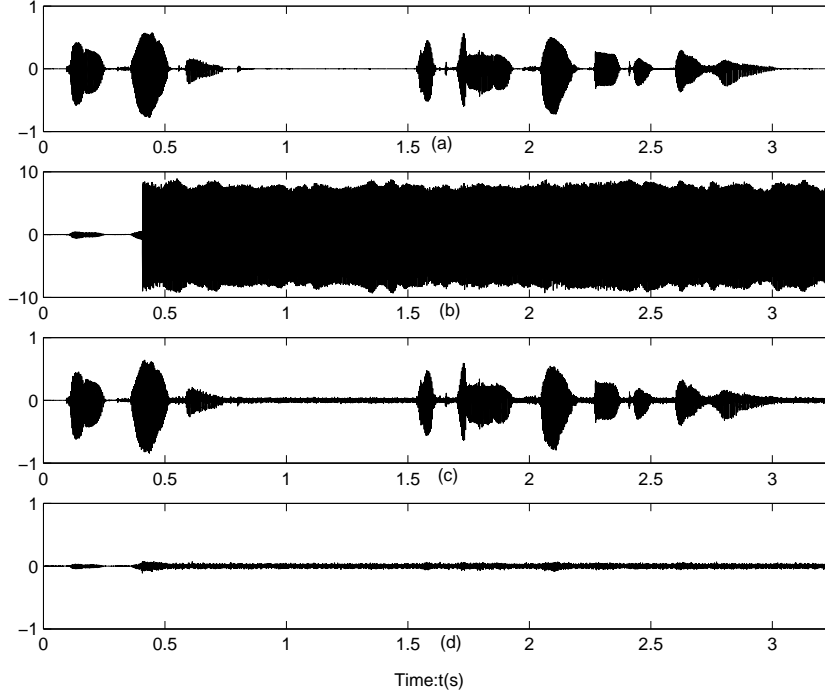


Figure 3.14: Processing results for scenario 2: (a) Desired signal $s(t)$; (b) Received noisy signal in one channel; (c) Beamformer output $z_2(t)$; (d) Error signal: $e_2(t) = z_2(t) - s(t)$.

direction ($\phi_0 = 180^\circ, \theta_0 = 60^\circ$), and ambient noise in the background. The SIR is $-30dB$ and the SNR is $0dB$. It should be noted that the SIR is computed based on the average energy of the two speech signals, which are broadband signals. Because the energy of a speech signal concentrates mostly in low frequencies, it can be expected that the actual SIRs at those low frequencies may be less than the average SIR $-30dB$. The narrow-band beamformers at those low frequencies cannot completely remove those strong interference since the sidelobe level is $-30dB$. In order to remove the interference, we use the combined design to incorporate the beamformer with $-30dB$ sidelobe into a LCMV beamformer that also has a null at the direction of the interference. Fig. 3.15 shows the 2-D array pattern obtained at $700Hz$, which is taken out of the 3-D array pattern by using the surface $\theta = 60^\circ$ cutting through the main look direction. The 2-D array pattern has an overall sidelobe of $-30dB$ and a deep null at $\phi = 180^\circ$, which is the direction of the interference. The processing results using the new beamformer are

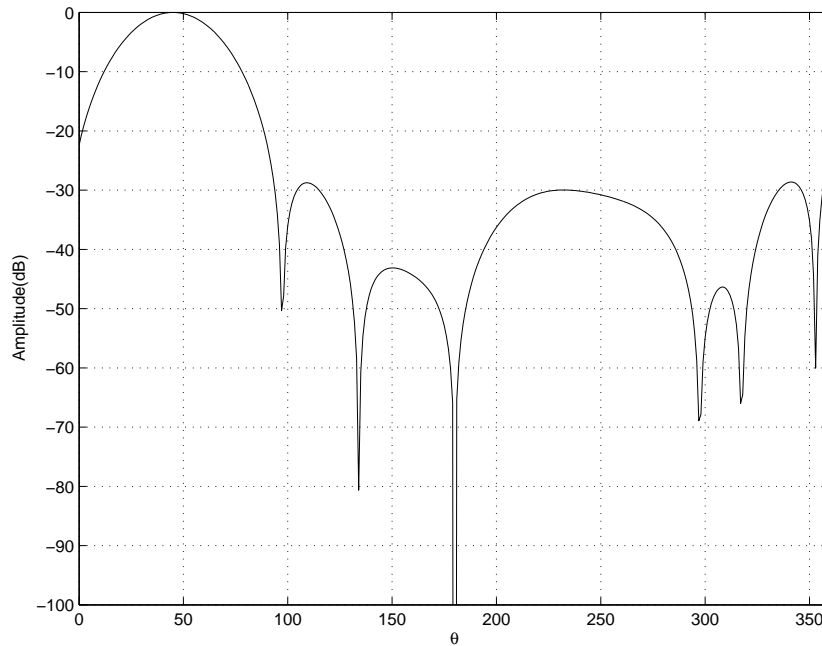


Figure 3.15: 2-D array pattern obtained at $700Hz$.

shown in Fig. 3.16. By examining the output in (c) and error signal in (d), it is seen the beamformer successfully removes the interference and noise.

3.6.2 Method II

In this subsection we use an example to demonstrate Method II. The discrete CRA used in this example is composed of 4 rings. Using the band broadening technique, the array can operate on a frequency range centered around the array's original operating frequency f_0 . The radii normalized by the wavelength λ_0 are: $R/\lambda_0 = [0.2346, 0.4691, 0.7037, 0.9382]$. A Chebyshev function with $-20dB$ sidelobe level is used as the desired array pattern. From (3.28), the minimum number of array elements required for each ring is found to be $N1 = [6, 10, 14, 18]$. To demonstrate the error control ability of the proposed method, a reduced set $N2 = [4, 8, 10, 12]$ is used, resulting in a saving of 14, or about 30% of the array elements. In Method II, the weighting matrix in (3.33) is chosen so that the mismatched error in the sidelobe region receives more weighting to achieve more

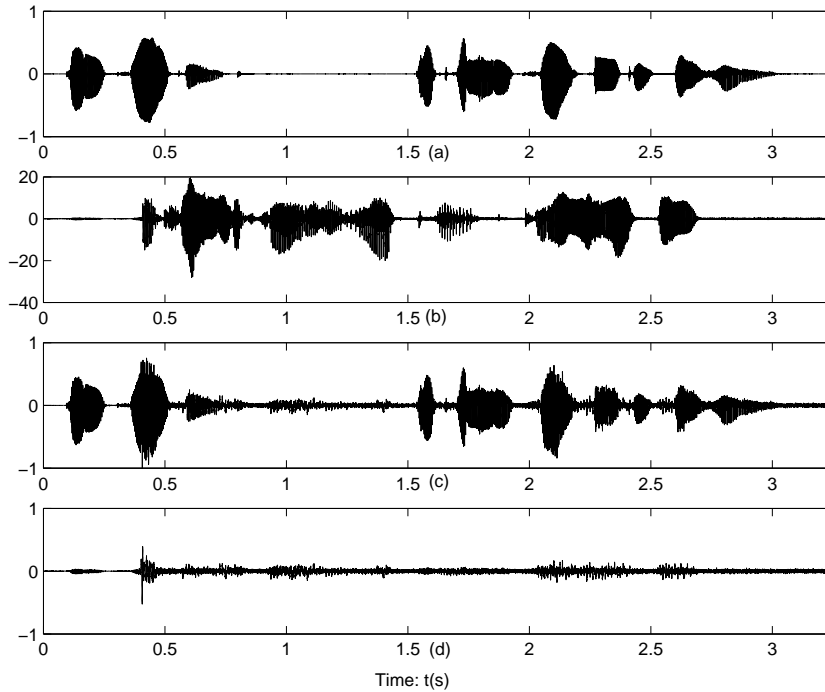


Figure 3.16: Processing results for scenario 3: (a) Desired signal $s(t)$; (b) Received noisy signal in one channel; (c) Beamformer output $z_3(t)$; (d) Error signal: $e_3(t) = z_3(t) - s(t)$.

reduction in this region. Only one linear constraint that is the unit gain constraint in the signal's look direction ($\phi_0 = 45^\circ, \theta_0 = 90^\circ$) is used.

For the signal component at frequency f_0 , the synthesized array pattern (solid line) using Method II is presented in Fig. 3.17 together with the desired array pattern (dotted line). The synthesized array pattern has achieved a sidelobe level of $-20dB$ at the price of a slightly wider mainlobe. The balance of the mainlobe width and sidelobe level can be adjusted through the weighting matrix K to some extent. Comparison between synthesized array pattern using Method II and Method I is presented in Fig.3.18. In both cases, the reduced set of array elements $N/2$ is used. The synthesized array pattern from Method I has a maximum sidelobe level of $-15dB$ due to insufficient number of array elements. Method II, however, achieves excellent result and has better control of the sidelobe level.

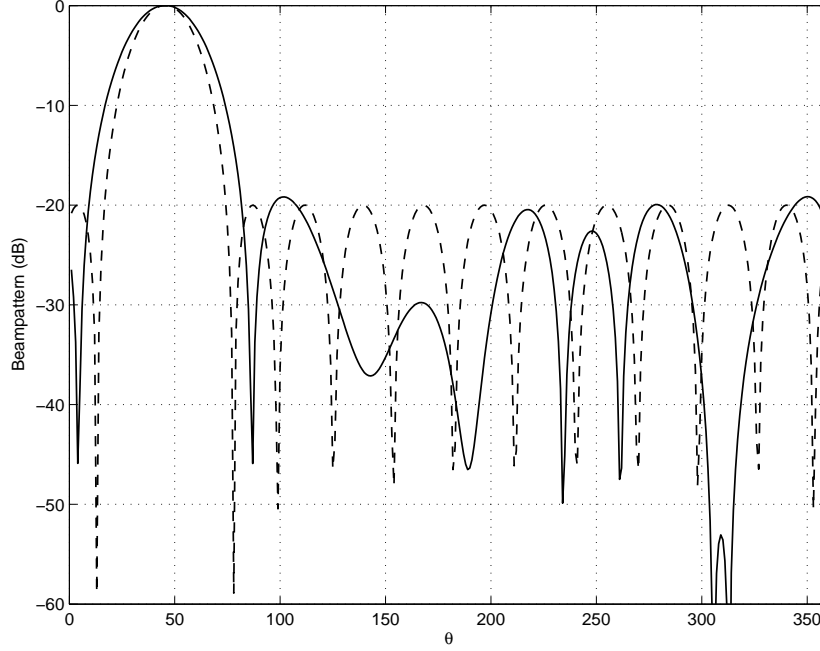


Figure 3.17: The Desired and synthesized array pattern: Desired (dashed line), synthesized (solid line). The main look direction is $\phi = 45^\circ$.

3.6.3 Method III

In this example, the highest operating frequency of the CRA is set to $f_0 = 2000Hz$ and the number of rings M in the CRA is chosen to be 12 to maintain the relative truncation error defined as in (3.19) to be $-30dB$ in the Fourier-Bessel series expansion. Assuming the sound speed is $343\text{ meter}/s$, the radii are determined by using (3.14). Among them, the largest radius is 0.50 meter and the smallest one is 0.03 meter. The number of array elements on each ring is then found from (3.41) as $N = [5\ 8\ 11\ 15\ 18\ 21\ 24\ 27\ 30\ 34\ 37\ 40]$, from the innermost to the outermost ring. The total number of array elements is 270.

In the first simulation, the look direction of the CRA is $(\phi_0, \theta_0) = (45^\circ, 45^\circ)$. The desirable array pattern $g(\varphi)$ is the Chebyshev function of order 8 [87] and has a $-30dB$ sidelobe level. The 3-D beampattern obtained from the proposed method in Section 3.3 at $f_0 = 2000Hz$ is shown in Fig. 3.19. The 3-D beampattern has two mainlobes and

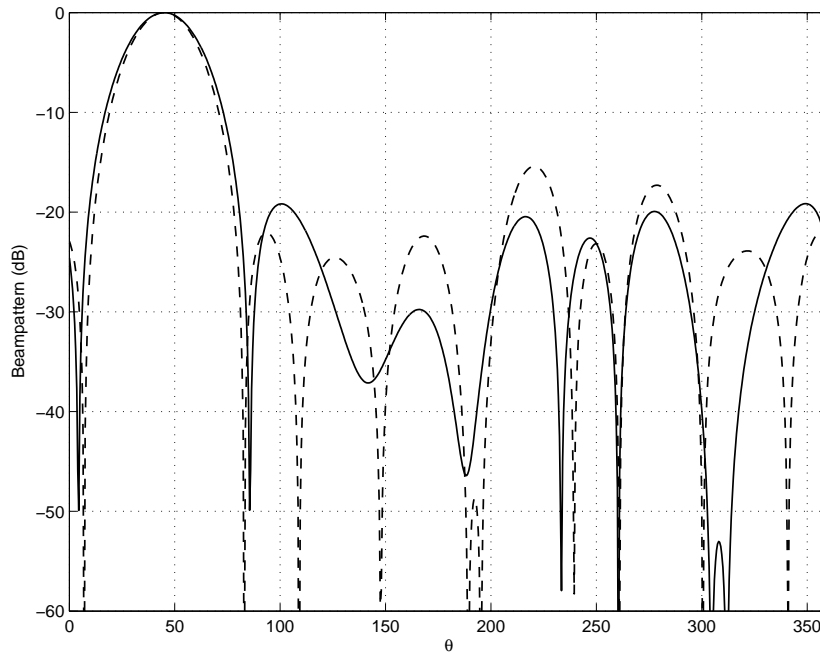


Figure 3.18: Method I (dashed line) vs. Method II (solid line). The main look direction is $\phi = 45^\circ$.

is symmetric with respect to the x - y plane due to the DOA ambiguity of planar arrays. The mainlobes are quite directional to provide effective 3-D beamforming.

We now apply Method III to achieve FI array patterns over a certain frequency range. The look direction of the CRA is $(\phi_0, \theta_0) = (45^\circ, 60^\circ)$. At a given frequency f , the delay-and-sum weights are first generated using (3.6). Next, (3.12) is applied to $g(\varphi)$ to obtain the inter-ring weights w_m . (3.8) is then used to generate the array pattern. The array patterns from $900Hz$ to $2000Hz$ with $100Hz$ increment are depicted in Fig. 3.20 and overlapped in Fig. 3.21. For illustration purpose, only the 2-D beampatterns by cutting through the mainlobes of the 3-D beampatterns using a surface defined by $\theta = 60^\circ$ are shown. From the figures it is clear that the sidelobe level is kept at $-30dB$, and the mainlobe width is approximately the same at the frequencies within the range from 900 to $2000Hz$. Note that the beampatterns in Fig. 3.20 and Fig. 3.21 represent the ideal case and they have not taken into account the distortion due to finite length FFT applied to the input signal for broadband beamforming.

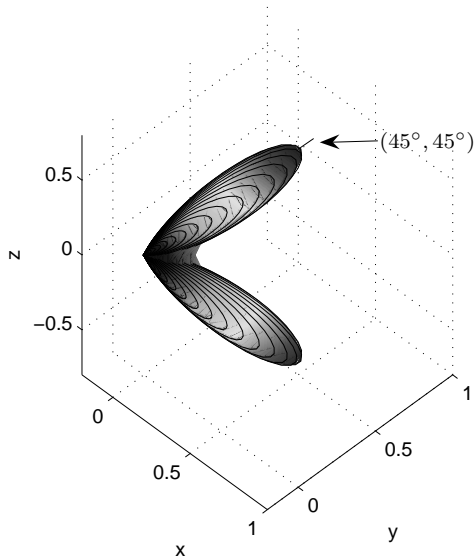


Figure 3.19: 3D array pattern at $2000Hz$, the look direction is $(45^\circ, 45^\circ)$

To verify that the 3-D array patterns are indeed frequency invariant, we compare the relative Mean Squared Error (MSE) in the array pattern at a given frequency with respect to that at $f_0 = 2000Hz$, i.e.,

$$MSE_f = \int_{\theta} \int_{\phi} |F_f(\phi, \theta) - F_{f_0}(\phi, \theta)|^2 d\phi d\theta / \int_{\theta} \int_{\phi} |F_{f_0}(\phi, \theta)|^2 d\phi d\theta.$$

The MSE_f from $600Hz$ to $2000Hz$ is shown in Fig. 3.22. It is seen from the figure that the relative MSE in the array pattern generally increases when f decreases. This is because that the truncation error of the Fourier-Bessel series becomes larger at lower frequencies. If the tolerable relative MSE is $-35dB$, then the lowest frequency to maintain FI array pattern is around $900Hz$.

The dynamic range ratios for the inter-ring weights over the 900 - 2000 Hz frequency range are 5.5651, 2333.0 and 89.4168 for the minimum, maximum and mean values. The large maximum value is resulted from a very small weight (0.001) in the outermost ring at a few frequencies, where the Fourier-Bessel expansion (3.11) is able to approximate the Chebyshev function very well with only the first few terms.

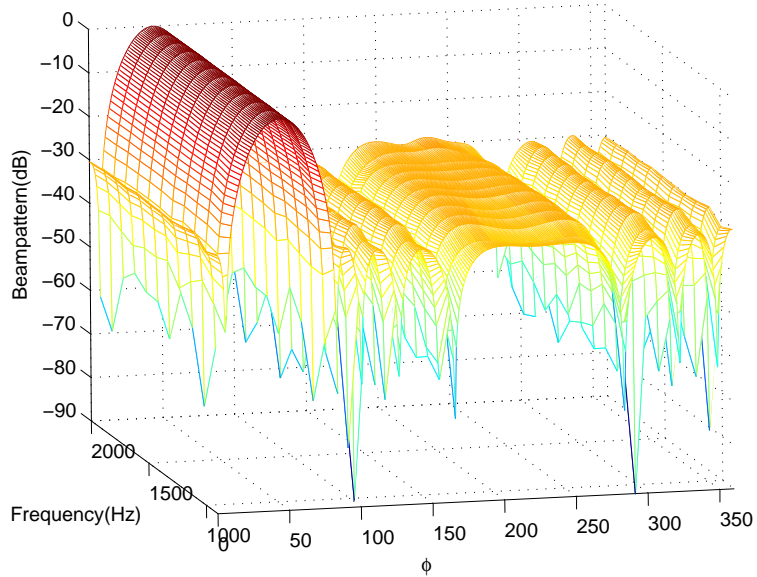


Figure 3.20: 3-D view of 2-D beampatterns from $900Hz$ to $2000Hz$, sampled at every $100Hz$.

3.7 Summary

In this chapter, we have discussed the design of deterministic broadband beamforming using CRA. To facilitate our design, we partition the weights into two parts: the inter-ring weights and intra-ring weights. We focus on how to control the sidelobe and/or mainlobe of the array pattern through designing of the inter-ring weights, and the intra-ring weights are fixed to delay-and-sum weights. Three methods to derive the inter-ring weights have been proposed. In Method I, the inter-ring weights at the original operating frequency is first obtained through Fourier-Bessel series expansion so that a desired sidelobe level can be achieved. An interpolation technique is then used to obtain weights at a range of frequencies that can yield the desired sidelobe level. Method II uses MMSE optimization to find the inter-ring weights that can reduce the pattern synthesis error when array elements are not enough. Method III improves on previous methods by selecting appropriate desirable prototype array pattern at a frequency and then extend it to other different frequencies to achieve FI design. To broaden the applications of our

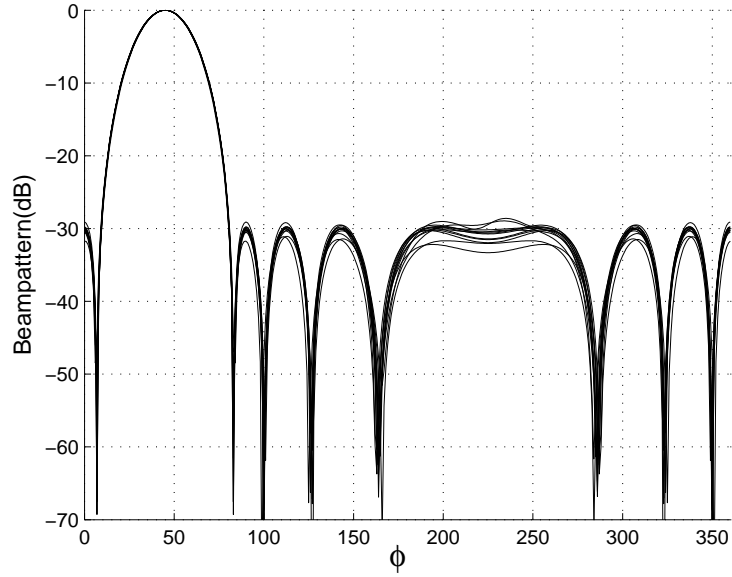


Figure 3.21: Overlapped beampatterns from $900Hz$ to $2000Hz$, sampled at every $100Hz$.

proposed deterministic designs, we show that they can be incorporated into a LCMV beamformer so that nulls can be added into the array pattern to cancel strong interferences. The experiment and simulation results verify that our design of a deterministic broadband CRA is successful.

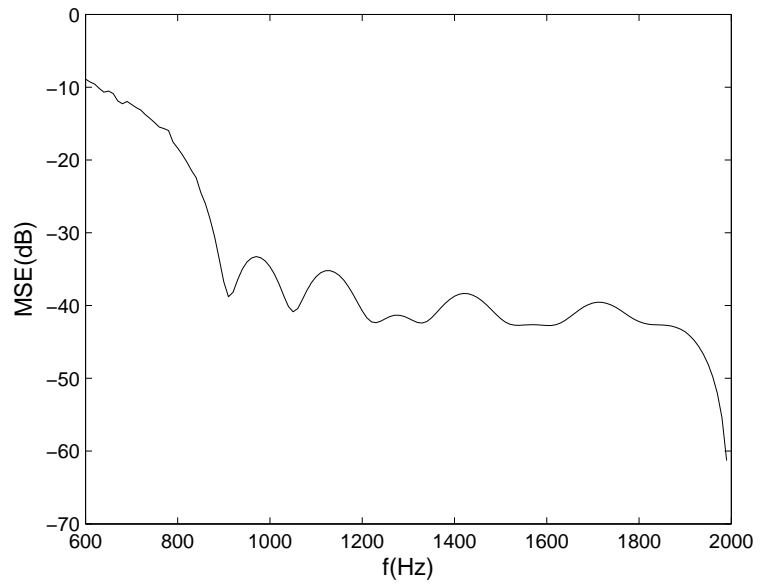


Figure 3.22: The relative MSE from $600Hz$ to $2000Hz$.

Chapter 4

Design of Adaptive Concentric Ring Array

The deterministic beamformers described in Chapter 3 work most effectively in stationary environment where an appropriate sidelobe level can be chosen based on the *a priori* knowledge of noise and interferences. A drawback of the deterministic beamformer is that it is unable to track changes in the signals, thus its performance tends to deteriorate in non-stationary signal environment.

In non-stationary signal environment, adaptive beamforming is necessary. Adaptive array can adapt its weights by learning the characteristics of an environment in real-time, thus they are more suitable for applications in non-stationary environment. Although many existing adaptive array design methods are available, the difficulty of designing an adaptive broadband CRA lies in that it usually consists of a large number of array elements. Thus if the array operates in a fully adaptive manner, the computation burden can be a serious issue for real-time applications. Moreover, the convergence rate can be slow, which makes the adaptive array ineffective in rapidly changing signal environment.

This chapter addresses the problem of designing adaptive CRA. To increase the convergence rate and reduce computation, we propose a partially adaptive array by making use of the specific structure of the CRA. In the proposed design, only a small portion of

the array weights are adapted while the majority others are kept fixed by using *a priori* knowledge of the desired signal's DOA, which is usually available to a beamformer. The proposed design can be implemented as a Linear Constrained Minimum-Variance (LCMV) beamformer or a General Sidelobe Canceller (GSC). Results from the deterministic beamformer design can then be incorporated to reduce the sidelobe level in the LCMV or GSC's quiescent beampattern [88]. The proposed method to achieve partially adaptive CRA is generic and different adaptation algorithms can be applied.

The rest of this chapter is organized as follows. In Section 4.1, we discuss the design of a fully adaptive CRA. Two adaptive approaches are available and the disadvantages of applying them to a fully adaptive large size array are discussed. In Section 4.2, we propose a generalized partially adaptive CRA design method for arbitrary partitioning schemes. Implementation of the partially adaptive CRA using the LMS and RLS algorithms are also presented. Performance analysis of the proposed partially adaptive CRA is presented in Section 4.3. In Section 4.4, several partially adaptive CRAs from different partitioning schemes are demonstrated and their performances in terms of convergence rate and residual interference and noise power are compared through simulations. Finally, a summary is given in Section 4.5.

4.1 Fully Adaptive CRA

As discussed earlier in Section 2.2.2 of Chapter 2, the LCMV beamformer is the mostly widely used form in adaptive beamforming. In our research, we only consider implementing the adaptive CRA as a LCMV beamformer and its equivalent form – the GSC. Basic concepts of the LCMV and GSC have already been presented in Chapter 2, here we only briefly describe the optimum solutions for the CRA implemented as a LCMV or GSC beamformer, and then focus the discussion on the adaptive approaches to compute the optimum solutions.

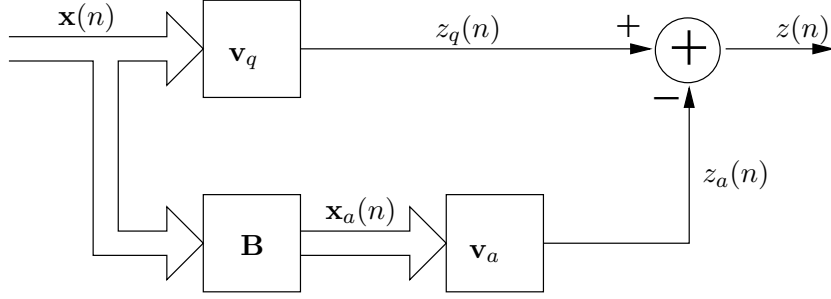


Figure 4.1: General sidelobe canceller.

The CRA considered here consists of M rings and a total of $K = \sum_{m=1}^M N_m$ array elements, where N_m is the number of array elements on the m -th ring. Its output at time index n is given by

$$z(n) = \mathbf{v}^H \mathbf{x}(n) \quad (4.1)$$

where \mathbf{v} is the weight vector and $\mathbf{x}(n)$ is the data vector, both are $K \times 1$ vectors.

The CRA is implemented as a LCMV beamformer with a number of Q linear constraints specified as

$$\mathbf{C}^H \mathbf{v} = \mathbf{b} \quad (4.2)$$

where \mathbf{C} is a $K \times Q$ constraint matrix and \mathbf{b} is a $Q \times 1$ vector of constraint values.

The weights are chosen to minimize the power of the beamformer output $E[|z(n)|^2] = \mathbf{v}^H \mathbf{R}_{xx} \mathbf{v}$ subjecting to a set of linear constraints given in (4.2), and the solution is given by [2]

$$\mathbf{v}_{opt} = \mathbf{R}_{xx}^{-1} \mathbf{C} (\mathbf{C}^H \mathbf{R}_{xx}^{-1} \mathbf{C})^{-1} \mathbf{b}. \quad (4.3)$$

where $\mathbf{R}_{xx} = E[\mathbf{x}(n)\mathbf{x}^H(n)]$ is the spatial covariance matrix of the array data.

Next, we look at the alternative implementation of the LCMV beamformer using the GSC structure. The diagram of the GSC is shown in Fig. 4.1. The upper branch in the GSC is the quiescent response of the beamformer and \mathbf{v}_q is given by [72]

$$\mathbf{v}_q = \mathbf{C} (\mathbf{C}^H \mathbf{C})^{-1} \mathbf{b}, \quad (4.4)$$

which is determined by the constraints only and independent of array data.

In the lower branch, the array signal $\mathbf{x}(n)$ goes through the blocking matrix \mathbf{B} and yields $\mathbf{x}_a(n)$, thus $\mathbf{x}_a(n) = \mathbf{B}^H \mathbf{x}(n)$. The weights \mathbf{v}_a are chosen to minimize the mean squared error of the GSC output $z(n)$, which is an unconstrained optimization problem and the solution is given by [72]

$$\mathbf{v}_{a,opt} = \mathbf{R}_{x_a x_a}^{-1} \mathbf{r}_{x_a z_q} \quad (4.5)$$

where $\mathbf{R}_{x_a x_a} = E[\mathbf{x}_a(n) \mathbf{x}_a^H(n)]$ is the spatial covariance matrix of $\mathbf{x}_a(n)$ and $\mathbf{r}_{x_a z_q} = E[\mathbf{x}_a(n) z_q^*(n)]$ is the cross-correlation vector between $\mathbf{x}_a(n)$ and $z_q(n)$.

The number of unconstrained weights in the beamformer is referred as *degrees of freedom* (DOFs). In the fully adaptive CRA, the number of weights is K and the number of linear constraints is Q , and thus the DOFs is $K - Q$. This relation is clearly shown in the GSC, where the adaptive branch performs an unconstrained optimization and the dimension of the adaptive weight vector is exactly $K - Q$. For the LCMV, the DOFs is also $K - Q$, although it is not explicitly shown in the form of its optimum weight vector in (4.3).

The optimum solutions obtained for the LCMV and GSC beamformers in (4.3) and (4.5) require knowledge of the second order statistics of the array signal, which are usually unknown in practice and need to be estimated. By assuming the array signal is ergodic in time, those statistics can be estimated through the time ensemble average of the signal. In the case of non-stationary signal environment, those statistics change with time and adaptive algorithms are most suitable for finding the optimum solutions. There are two adaptive approaches available, namely the block adaptive approach and the sample-by-sample adaptive approach [74], which are described below.

4.1.1 Adaptive Approaches

(1) Block Adaptive Approach

The block adaptive approach uses a block of data to estimate the statistics of the

signal, and calculate the optimum solution based on the estimation results. The block of data being used is updated with incoming samples so that the algorithm can track the changes in the signal.

Suppose we take the optimum solution for the LCMV beamformer in (4.3) for example. The covariance matrix \mathbf{R}_{xx} is typically estimated using the Maximum-likelihood (ML) estimation, which yields

$$\hat{\mathbf{R}}_{xx} = \frac{1}{N_B} \sum_{n=0}^{N_B-1} \mathbf{x}(n)\mathbf{x}^H(n) \quad (4.6)$$

where N_B is the length of the data block and n denotes the sample index of the data vector in the block. The solution of the LCMV beamformer is obtained by substituting (4.6) into (4.3), which yields

$$\hat{\mathbf{v}}_{opt} = \hat{\mathbf{R}}_{xx}^{-1} \mathbf{C}(\mathbf{C}^H \hat{\mathbf{R}}_{xx}^{-1} \mathbf{C})^{-1} \mathbf{b}. \quad (4.7)$$

Notice that the inverse of $\hat{\mathbf{R}}_{xx}$ requires $\hat{\mathbf{R}}_{xx}$ to be a full rank matrix. $\hat{\mathbf{R}}_{xx}$ is a $K \times K$ matrix, therefore to yield a full rank $\hat{\mathbf{R}}_{xx}$ using the estimation method in (4.6), it requires averaging of at least K samples of the data vector $\mathbf{x}(n)$. Thus the block size N_B must satisfy $N_B \geq K$. In some beamforming applications, training data is available for estimation of the statistics. In such case, using larger N_B gives better results.

The block adaptive approach for the GSC can be developed in a similar way. In the GSC, the spatial covariance matrix $\mathbf{R}_{x_a x_a}$ is of size $(K - Q) \times (K - Q)$, which is smaller than the covariance matrix used in the LCMV. Usually Q is small, and the size of the spatial covariance matrices in both cases are mostly determined by the array size K . A CRA normally consists of a large number of array elements, thus the covariance matrices also have large size. It is known that the inversion of large size matrices is very time consuming: roughly $O(K^3)$ multiplies are involved. For this reason, the block adaptive approach is not suitable for large size CRA.

Another drawback of the block adaptive approach is that when the signal statistics are time-varying and the length of data block is relatively large, the estimation results

can be poor. This problem is especially serious for large size array, since the length of the block must be kept above some minimum, i.e., K in the case of the LCMV or $K - Q$ in the case of the GSC , to yield an estimated spatial covariance matrix of full rank.

(2) Sample-by-sample Adaptive Approach

The sample-by-sample adaptive approach avoids directly solving the matrix inverse to compute the optimum weights. Instead, the weights are updated on each incoming sample so that they can gradually converge to the optimum solution. By doing so, the beamformer has better tracking ability and the computation is less complex comparing to the block adaptive approach. Because of these advantages, we adopt the sample-by-sample adaptive approach to implement the adaptive CRA.

Two most widely used sample-by-sample adaptive algorithms are the Least Mean Square (LMS) and the Recursive Least Squares (RLS) algorithms [72]. Details on implementation of these two algorithms are illustrated later in Section 4.2.3. For now we only give a general description of them.

The LMS algorithm is based on the method of steepest descent. The error surface of the MSE of the beamformer output has the shape of a bowl and the optimum weights reside in the bottom of the bowl. At each incoming sample, the LMS algorithm adjusts the current weights in the direction that yields the steepest descent on the error surface, so that the weights can take the shortest way to converge to the optimum weights.

In the RLS method the time consuming process of directly computing the inverse of the matrix is avoided. The RLS method is based on recursively updating the inverse of the covariance matrix as new data samples coming in. Usually the data samples used to update the inverse of the matrix are exponentially weighted so that the effects of relatively old data can be gradually removed and the adaptive weights are able to track the changes in current data samples.

The performance of the sample-by-sample adaptive methods greatly depends on the

convergence rate of the weights towards the optimum solution. A slow convergence rate may not be acceptable in some real-time applications. The convergence rate of LMS algorithm is inversely proportional to the eigenvalue spread of the covariance matrix: the larger the eigenvalue spread the slower the convergence rate. For large size covariance matrix, the eigenvalue spread tends to be large, which results in slow convergence rate. The RLS offers faster convergence rate independent of the eigenvalue spread, however, its convergence rate is also restricted by the array size, since it takes longer time to accurately estimate a large size covariance matrix. Although the RLS has faster convergence rate than the LMS, this advantage is overshadowed by its complexity. The multiplies involved in the LMS algorithm is roughly $O(2K)$ and the multiplies involved in the RLS algorithm is roughly $O(K^2)$. Application of the RLS algorithm in a large size fully adaptive array is restricted by the computational complexity required.

4.1.2 Broadband Adaptive Beamforming

The preceding discussion on computational complexity is limited to narrowband beamforming. As we have pointed out in Section 3.5.1, in broadband beamforming, the received broadband signal is usually decomposed into many narrowband components using FFT and different components are processed separately. Denote the number of FFT components as L . If the sample-by-sample adaptive approach is adopted, for the LCMV implementation, there are a total of $K \times L$ number of weights that need to be adapted; for the GSC implementation, the number of adaptive weights is $(K - Q) \times L$. When K or L is large, the total computation required can be a huge burden and become the major obstacle for real-time applications.

4.1.3 Summary on Fully Adaptive CRA

From the discussion above, it can be seen that the two most important issues concerning the design of fully adaptive CRA are the computational complexity and the convergence rate. A brief summary on them is given below.

(1) Computational complexity increase with the number of narrowbands and the size of the array.

(2) The effect of the array size on the computational complexity differs with algorithms. Block adaptive approaches have roughly $O(K^3)$ multiplies involved, thus they have limited usage in our research. Among the sample-by-sample adaptive approaches, the LMS requires roughly $O(2K)$ multiplies, the RLS requires roughly $O(K^2)$ multiplies.

(3) Large array size results in slow convergence rate for both LMS and RLS. Among them, the RLS has faster convergence rate, however, the computational complexity of the RLS makes it not suitable for large array.

The number of narrowband components and the array size are determined by application scenario, and usually cannot be reduced significantly without causing serious degradation in the beamformer performance. Thus the most practical solution to avoid the disadvantages listed above is to reduce the number of adaptive weights by developing partially adaptive array, which is the problem to be addressed in the next section.

4.2 Partially Adaptive CRA

4.2.1 Introduction to Partially Adaptive Array Design

Partially adaptive array design splits the whole array into many subarrays where deterministic beamforming is applied in each of them individually. The outputs from all the subarrays are then collected for further adaptive processing. This process can be interpreted as projecting the received array signal into a reduced-dimension signal subspace

and performing the optimization in the reduced-dimension subspace. Finding adaptively the optimum solution in the reduced-dimension subspace has faster convergence speed and requires less computation. However, the advantages are achieved at the cost of certain amount of degradation in the interference and noise cancellation performance, since the number of degrees of freedom (DOFs) in the optimization is reduced as compared to the fully adaptive array.

Projecting the original $K \times 1$ data vector \mathbf{x} into a reduced-dimension signal space can be described by a matrix \mathbf{T} of size $K \times K_r$, where K_r is the dimension of the reduced signal space. \mathbf{T} usually has the following form

$$\mathbf{T} = [\mathbf{v}_1, \mathbf{v}_2, \dots, \mathbf{v}_{K_r}], \quad (4.8)$$

where \mathbf{v}_m is a $K \times 1$ unit-norm column vector representing the weights for the m -th subarray. Thus each column of \mathbf{T} corresponds to a subarray. Depending on how \mathbf{T} and \mathbf{v}_m is constructed, the existing partially adaptive methods can be classified into two main categories: the element space method and the beam space method [72]. We briefly review these methods below.

The element space methods [98,99] split the array into many subarrays with less array elements. Thus \mathbf{v}_m has both zero and non-zero elements. Non-zero elements indicate that the corresponding array elements are included into the m -th subarray. Assuming the same look direction in each subarray, non-adaptive beamforming is performed and the outputs from all the subarrays are then collected for further adaptive processing. The element space methods can be applied to both the LCMV and the GSC.

The beam space methods [100–102] decompose \mathbf{T} as $\mathbf{T} = \mathbf{T}_r \mathbf{B}$ and then choose \mathbf{T}_r and \mathbf{B} separately. Different from element space method, each subarray in the beam space method has the same number of array elements but points to different possible directions of the interference. These beamformers form the columns of \mathbf{T}_r . \mathbf{B} is then used to select a subset of the output of \mathbf{T}_r , each subset usually consists of outputs from

beamformers pointing at adjacent directions. By doing so, the reduced-dimension signal space contains all the possible interferences and they can be used to adaptively estimate the statistics of interferences.

4.2.2 Proposed Partially Adaptive CRA

The preceding discussion shows that two approaches are available to implement the partially adaptive array, i.e., the beam space approach and the element space approach. The beam space methods requires *a priori* knowledge of the DOAs of the interference, which limits its applications. In our research, we are more interested in developing a beamformer suitable for general purpose applications, thus we take the element space approach to design the partially adaptive array.

Partially adaptive array seeks optimization in the reduced-dimension signal space and thus suffers performance degradation in terms of residual interference and noise power. The amount of degradation varies with partition schemes. Van Veen and Roberts [103] proposed a method to select partition scheme based on minimization of the power of the interference in the output. The method requires training in a range of possible interference signal scenarios, and the partition scheme yields the best average performance is chosen. Their method is more suitable in applications where *a priori* knowledge of the DOAs and statistics of the interferences are available. For general applications, there lacks a universal criterion to choose partition scheme, part of the difficulty also lies in that the choice of partition scheme is closely related to array geometry. For 1-D arrays, or 2-D arrays such as the cross array and the rectangular array etc., partition scheme is relatively easier to choose, because those arrays can be easily divided into many subarrays of similar dimension.

For CRA, it is more difficult to choose \mathbf{T} . In the following, we first derive the general form of a partially adaptive CRA with an arbitrary partitioning structure. Performance analysis will then follow in the next section.

An arbitrary partitioning scheme is described by \mathbf{T} of the form

$$\mathbf{T} = [\mathbf{h}_1, \mathbf{h}_2, \dots, \mathbf{h}_{K_r}], \quad (4.9)$$

where \mathbf{h}_m is a unit-norm column vector whose non-zero elements correspond the weights for the m -th subarray, and the number of those non-zero elements is the size of the m -th subarray. Here we assume \mathbf{T} has full column rank and its columns are linearly independent. Many standard deterministic beamforming techniques can be used to obtain \mathbf{h}_m . The deterministic beamforming within each subarray can reduce certain amount of noise and interference. The adaptive processing further attenuates the interferences by creating nulls in the incoming directions of interferences.

After projected by \mathbf{T}^H , a $K \times 1$ signal vector $\mathbf{x}(n)$ is reduced to a $K_r \times 1$ signal vector $\mathbf{y}(n)$ as

$$\mathbf{y}(n) = \mathbf{T}^H \mathbf{x}(n). \quad (4.10)$$

Adaptive processing is then performed on $\mathbf{y}(n)$ to form the final beamformer output

$$z(n) = \mathbf{w}^H \mathbf{y}(n) \quad (4.11)$$

where \mathbf{w} is a $K_r \times 1$ vector representing the adaptive weights for each ring.

Putting (4.10) into (4.11) yields

$$\begin{aligned} z(n) &= \mathbf{w}^H \mathbf{T}^H \mathbf{x}(n) \\ &= (\mathbf{T} \mathbf{w})^H \mathbf{x}(n) \end{aligned} \quad (4.12)$$

Comparing the above equation with the output of the fully adaptive array given in the form $z(n) = \mathbf{v}^H \mathbf{x}(n)$, it is seen that the partially adaptive array actually partitions the fully adaptive weight vector to

$$\mathbf{v} = \mathbf{T} \mathbf{w} = \begin{bmatrix} w_1 \mathbf{h}_1 \\ w_2 \mathbf{h}_2 \\ \vdots \\ w_{K_r} \mathbf{h}_{K_r} \end{bmatrix}. \quad (4.13)$$

In this partitioned form of \mathbf{v} , there are a total number of $(K + K_r)$ weights, among which we fix the K weights represented by \mathbf{h}_i using a priori knowledge and only adapts the K_r weights represented by \mathbf{w} .

It follows from (4.13) that the linear constraints specified as $\mathbf{C}^H \mathbf{v} = \mathbf{b}$ can be converted into constraints on \mathbf{w} as

$$\bar{\mathbf{C}}^H \mathbf{w} = \mathbf{b} \quad (4.14)$$

where $\bar{\mathbf{C}} = \mathbf{T}^H \mathbf{C}$.

With the preceding derivations, finding the optimum partially adaptive weights can be formed as a standard LCMV problem as described below,

$$\mathbf{w}_{opt} = \min_{\mathbf{w}} \mathbf{w}^H \mathbf{R}_{yy} \mathbf{w} \quad \text{subject to} \quad \bar{\mathbf{C}}^H \mathbf{w} = \mathbf{b}$$

where \mathbf{R}_{yy} denotes the covariance matrix of $\mathbf{y}(n)$ defined in (4.10). The DOFs in the partially adaptive array is $K_r - Q$.

The following design is presented using the GSC, because its structure offers greater clarity on the unconstrained optimization problem. The design of partially adaptive array implemented as LCMV is similar and will not be discussed separately.

The diagram of the proposed partially adaptive beamformer implemented as a GSC is shown in Fig. 4.2, where input data vector is the reduced-dimension vector $\mathbf{y}(n)$. \mathbf{w}_q in the upper branch specifies the quiescent pattern of the partially adaptive array, it can be specified using different techniques depending on the design objective. Here we choose \mathbf{w}_q so that the quiescent response in the partially adaptive array is the closest to that of the fully adaptive array in the least-squares sense. That is, given the quiescent response \mathbf{v}_q from certain design, we find \mathbf{w}_q that minimizes $\|\mathbf{T}\mathbf{w}_q - \mathbf{v}_q\|^2$ which yields

$$\mathbf{w}_q = (\mathbf{T}^H \mathbf{T})^{-1} \mathbf{T}^H \mathbf{v}_q. \quad (4.15)$$

Note that the matrix inverse in (4.15) always exists since \mathbf{T} has full column rank and its columns are linearly independent. The output of the quiescent response is denoted by $z_q(n)$ and $z_q(n) = \mathbf{w}_q^H \mathbf{y}(n)$.

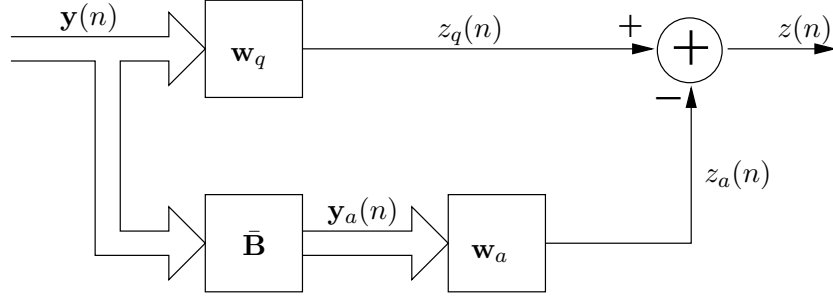


Figure 4.2: General sidelobe canceller.

In the lower branch of the partially adaptive GSC structure in Fig. 4.2, $\bar{\mathbf{B}}$ is a $M \times (M - Q)$ blocking matrix satisfying $\bar{\mathbf{B}}^H \bar{\mathbf{C}} = \mathbf{0}$. \mathbf{w}_a is the $(M - Q) \times 1$ adaptive weight vector. The optimum solution of \mathbf{w}_a is given by the Wiener-Hopf equation [72],

$$\mathbf{w}_{a,opt} = \mathbf{R}_{y_a y_a}^{-1} \mathbf{r} \quad (4.16)$$

where $\mathbf{R}_{y_a y_a} = E\{\mathbf{y}_a(n) \mathbf{y}_a^H(n)\}$ is the lower branch covariance matrix and $\mathbf{r} = E\{\mathbf{y}_a(n) z_q^*(n)\}$ is the cross-correlation vector between $\mathbf{y}_a(n)$ and $z_q(n)$.

4.2.3 Adaptive Algorithms

There are many adaptive algorithms available to obtain $\mathbf{w}_{a,opt}$. Among them the most popular ones are the LMC and RLS algorithms, we will describe their implementation for the partially adaptive CRA below.

LMS algorithm

The LMS algorithm is based on the steepest descent method. The optimum weights in adaptive branch is chosen based on minimizing the mean squared error between the outputs from the adaptive branch and quiescent branch, i.e., minimizing

$$\begin{aligned} E[|z(n)|^2] &= E[|z_q(n) - z_a(n)|^2] \\ &= E[[z_q(n) - \mathbf{w}_a^H \mathbf{y}_a(n)][z_q(n) - \mathbf{w}_a^H \mathbf{y}_a(n)]^H] \\ &= E[z_q(n) z_q^*(n)] - \mathbf{w}_a^H \mathbf{R}_{y_q z_q} - \mathbf{R}_{z_q y_a} \mathbf{w}_a + \mathbf{w}_a^H \mathbf{R}_{y_a y_a} \mathbf{w}_a. \end{aligned} \quad (4.17)$$

where $\mathbf{R}_{y_q z_q} = E[\mathbf{y}_a(n)z_q^*(n)]$, $\mathbf{R}_{z_q y_a} = E[z_q(n)\mathbf{y}_a^H(n)]$ and $\mathbf{R}_{y_a y_a} = E[\mathbf{y}_a(n)\mathbf{y}_a^H(n)]$.

The gradient of the above is

$$\nabla_{\mathbf{w}} = \frac{\partial E[|z(n)|^2]}{\partial \mathbf{w}^*} = -\mathbf{R}_{y_q z_q} + \mathbf{R}_{y_a y_a} \mathbf{w}_a \quad (4.18)$$

The new weight vector $\mathbf{w}_a(n+1)$ is obtained through adjusting the current weight vector $\mathbf{w}_a(n)$ towards the negative direction of the gradient, which yields

$$\begin{aligned} \mathbf{w}_a(n+1) &= \mathbf{w}_a(n) - \mu \nabla_{\mathbf{w}} \\ &= \mathbf{w}_a(n) - \mu [-\mathbf{R}_{y_q z_q} + \mathbf{R}_{y_a y_a} \mathbf{w}_a(n)] \end{aligned} \quad (4.19)$$

where μ is the step size indicating the amount of adjustment. Larger value of μ results in faster convergence rate but also raises the gradient noise level in steady-state. The statistics $\mathbf{R}_{y_q z_q}$ and $\mathbf{R}_{y_a y_a}$ are not available and need to be estimated.

In LMS algorithm these statistics are replaced by their instantaneous estimates, i.e., $\mathbf{R}_{y_q z_q}$ is replaced by $\mathbf{y}_a(n)z_q^*(n)$ and $\mathbf{R}_{y_a y_a}$ is replaced by $\mathbf{y}_a(n)\mathbf{y}_a^H(n)$. Putting the instantaneous estimates into (4.19) and rearrange them yields

$$\mathbf{w}_a(n+1) = \mathbf{w}_a(n) + \mu z_q^*(n)\mathbf{y}_a(n), \quad (4.20)$$

where $z(n)$ is obtained as

$$z(n) = z_q(n) - \mathbf{w}_a^H(n)\mathbf{y}_a(n). \quad (4.21)$$

In practice, to simplify the selection of μ in (4.20), normalized LMS (NLMS) algorithm is usually used:

$$\mathbf{w}_a(n+1) = \mathbf{w}_a(n) + \frac{2\mu}{\mathbf{y}_a^H(n)\mathbf{y}_a(n)} \mathbf{y}_a(n)z_q^*(n). \quad (4.22)$$

It is shown that the NLMS algorithm converges in the mean square if $0 < \mu < 1$ [104]. In the following analysis and simulations we will use NLMS instead of LMS algorithm.

The convergence rate of the NLMS algorithm is dependent on the eigenvalue spread of the covariance matrix $\mathbf{R}_{y_a y_a}$: the larger the eigenvalue spread of $\mathbf{R}_{y_a y_a}$, the slower the

convergence rate. The convergence rate in NLMS can be increased by enlarging the step size μ but the steady state performance will suffer.

RLS algorithm

Due to the small number of adaptive weights in the proposed partially adaptive array, more advanced adaptive algorithm such as RLS [72] algorithm can be used. RLS algorithm recursively computes the inverse of the covariance matrix, which yields faster convergence rate when compared to the NLMS algorithm. The RLS algorithm applied to the proposed partially adaptive array is summarized as follow:

$$\mathbf{G}(n) = \frac{\mathbf{P}(n-1)\mathbf{y}_a(n)}{\gamma + \mathbf{y}_a^H(n)\mathbf{P}(n-1)\mathbf{y}_a(n)} \quad (4.23)$$

$$z(n) = z_q(n) - \mathbf{w}_a^H(n-1)\mathbf{y}_a(n) \quad (4.24)$$

$$\mathbf{P}(n) = \frac{1}{\gamma}[\mathbf{P}(n-1) - \mathbf{G}(n)\mathbf{y}_a^H(n)\mathbf{P}(n-1)] \quad (4.25)$$

$$\mathbf{w}_a(n) = \mathbf{w}_a(n-1) + \mathbf{G}(n)z^*(n) \quad (4.26)$$

where γ is a constant, and its typical value is between 0.98 and 1.

4.2.4 Comparison Between the Fully and Partially Adaptive CRA

Comparing the fully adaptive array with the proposed partially adaptive array, the DOFs in the weights is reduced from $(K - Q)$ to $(K_r - Q)$. The number of complex multiplications required to update the weight vector for both of them is listed in Table 4.1 for comparison. In typical applications, K is in the order of hundreds and K_r is less than 10. Thus the proposed partially adaptive beamformer is able to reduce greatly the computation and at the same time improve significantly the convergence rate and hence the tracking performance.

The partially adaptive array has $(K_r - Q)$ DOFs and it is capable of cancelling up to $(K_r - Q)$ additional interferences besides those priorly specified in the linear constraint

	Fully adaptive	Partially adaptive
LMS	$O(2(K - Q) + K)$	$O(2(K_r - Q) + K)$
RLS	$O(3(K - Q)^2 + K)$	$O(3(K_r - Q)^2 + K)$

Table 4.1: Number of required complex multiplications.

matrix $\bar{\mathbf{C}}$. One consequence of the partially adaptive method is that the Mean Square Error (MSE) of the steady state output will be larger than that of the fully adaptive one due to the reduction in the DOFs for the weights. Based on the optimum solution (4.16), it is shown in Section 4.4 that the increase in steady state MSE of the partially adaptive array is only marginal: less than $1.6dB$ at $30dB$ interference-to-noise ratio (INR) and about $1.2dB$ at $-20dB$ INR.

4.3 Analysis of Partially Adaptive CRA

The performance of the partially adaptive array largely depends on the choice of \mathbf{T} . First of all, the number of columns in \mathbf{T} determines the number of DOFs in the partially adaptive array, which is given by $K_r - Q$. It is also equal to the maximum number of interferences that the array can remove. Thus, K_r should be set large enough to remove the maximum number of expectable interferences. In fact, a larger K_r value also provides more DOFs so that the adaptive weights can be adjusted to provide a smaller amount of residual interference and noise in the array output. However, K_r should not be too large, otherwise the gain in convergence rate (tracking ability) and computation will be reduced.

Once the size of \mathbf{T} is determined, the remaining task is to choose a partition scheme to divide the array into K_r subarrays. Interesting though, given a fixed K_r , different partition schemes (choice of \mathbf{T}) will affect the convergence speed resulted from different eigenvalue spreads as well as residual interference and noise power.

4.3.1 Convergence Rate

The convergence rate in the NLMS algorithm (4.22) is governed by the number of adaptive coefficients and the eigenvalue spread of the input correlation matrix. Partially adaptive array has only $K_r - Q$ adaptive coefficients as compared to $K - Q$ in fully adaptive case. If K_r is much less than K , a significant increase in convergence speed is achieved. The behavior of the eigenvalue spread of the input correlation matrix in the adaptive system is more difficult to predict. In fact, it is dependent on the partition matrix \mathbf{T} .

In general, the partially adaptive array always yields faster convergence rate since K_r is much smaller than K . If more sophisticated adaptive algorithm is employed such as the RLS algorithm, the convergence rate is independent of the eigenvalue spread and depends only on K_r . In such a case, different partitioning schemes but with the same size of \mathbf{T} will give identical convergence speed.

4.3.2 Steady State Performance

Analysis of the steady state performance of partially adaptive array can be found in [105]. The array structure we adopted in our research is different than the one used in [105]. Here we develop the theoretical formula to calculate the steady state residual interference and noise power in our proposed array structure.

From adaptive filter theory and the GSC system in Fig. 4.2, the adaptive weight vector \mathbf{w}_a will converge to the optimum solution given by the Wiener-Hopf equation [105] at steady state,

$$\begin{aligned}\mathbf{w}_{a,opt} &= E[\mathbf{y}_a(l)\mathbf{y}_a^H(l)]^{-1}E[\mathbf{y}_a(l)z_q^*(l)] \\ &= (\mathbf{T}_e^H \mathbf{R}_{xx} \mathbf{T}_e)^{-1} \mathbf{T}_e^H \mathbf{R}_{xx} \mathbf{v}_e\end{aligned}\tag{4.27}$$

where $\mathbf{T}_e = \mathbf{T}\bar{\mathbf{B}}$, $\mathbf{v}_e = \mathbf{T}\mathbf{w}_q$ and (4.10) has been used to derive the result. The desired signal is uncorrelated with the interference and noise, hence \mathbf{R}_{xx} can be decomposed as

$\mathbf{R}_{xx} = \mathbf{R}_s + \mathbf{R}_{i+n}$, where \mathbf{R}_s denotes the desired signal correlation matrix and \mathbf{R}_{i+n} is the correlation matrix of interference plus noise. Utilizing a property of the GSC that $\mathbf{T}_e^H \mathbf{R}_s = \mathbf{0}$, (4.27) becomes

$$\mathbf{w}_{a,opt} = (\mathbf{T}_e^H \mathbf{R}_{i+n} \mathbf{T}_e)^{-1} \mathbf{T}_e^H \mathbf{R}_{i+n} \mathbf{v}_e. \quad (4.28)$$

For partially adaptive array, the residual interference and noise power at the steady state in the array output is

$$p_{i+n,ss} = \mathbf{w}_{opt}^H \mathbf{T}^H \mathbf{R}_{i+n} \mathbf{T} \mathbf{w}_{opt}, \quad (4.29)$$

where \mathbf{w}_{opt} is the overall optimum weight vector in the adaptive system shown in Fig. 2, which is $\mathbf{w}_{opt} = \mathbf{w}_q - \bar{\mathbf{B}} \mathbf{w}_{a,opt}$. Upon using (4.28), (4.29) becomes

$$\begin{aligned} p_{i+n,ss} &= \mathbf{v}_e^H \mathbf{R}_{i+n} \mathbf{v}_e \\ &\quad - \mathbf{v}_e^H \mathbf{R}_{i+n} \mathbf{T}_e (\mathbf{T}_e^H \mathbf{R}_{i+n} \mathbf{T}_e)^{-1} \mathbf{T}_e^H \mathbf{R}_{i+n} \mathbf{v}_e. \end{aligned} \quad (4.30)$$

The first term in (4.30) is the interference and noise power in the upper branch. The second term represents the interference and noise power that can be reduced by the lower branch, and it is subtracted from that in the upper branch to form the residual interference and noise power in the array output. The partition scheme affects the estimation performance in the lower branch and thus the ability of removing interference and noise. This is clear in (4.30) where $p_{i+n,ss}$ is explicitly dependent on $\mathbf{T}_e = \mathbf{T} \bar{\mathbf{B}}$. For all the candidate partition schemes under certain signal scenario, $p_{i+n,ss}$ can be evaluated and serves as a criterion to compare the performance of different partition schemes.

4.4 Experimental Results

This section first uses some examples to illustrate the proposed design method by examining the performance of partially adaptive arrays in terms of their convergence rates and the residual interference and noise power. A realistic broadband beamforming example is then given to show the flexibility of the proposed design method. Four types

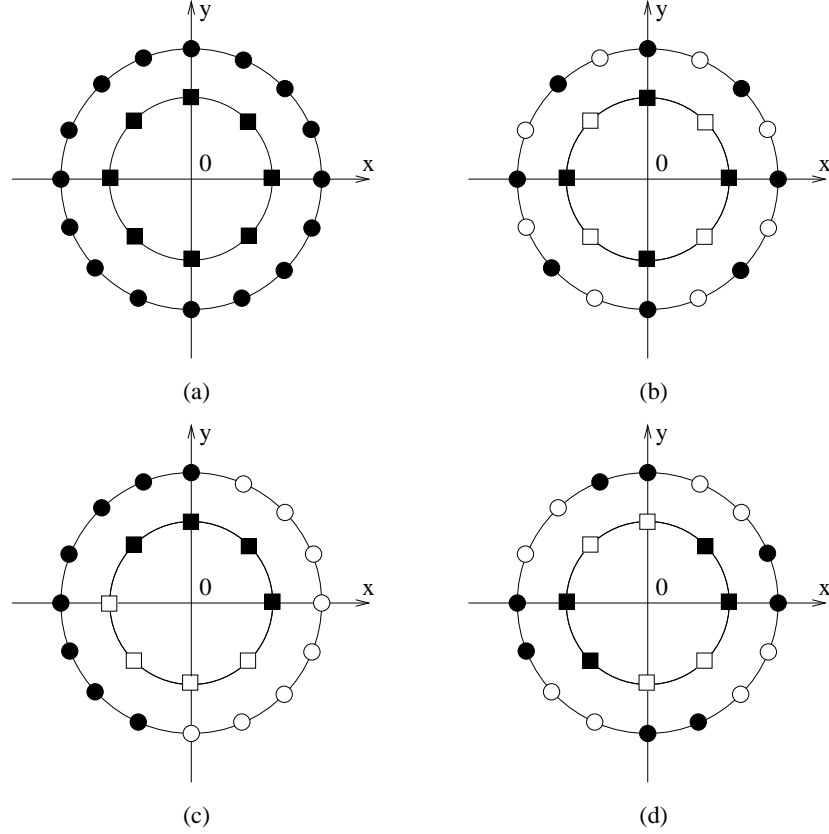


Figure 4.3: Partition schemes of partially adaptive arrays: Type 1 (a), Type 2 (b), Type 3 (c) and Type 4 (d). Only two adjacent rings are shown, where the array elements in the same subarray are represented by the same symbols.

of partially adaptive CRAs are examined here as shown in Fig. 4.3 where only two adjacent rings are shown for illustration purpose:

Type 1: Each of the M rings in a CRA is treated as a subarray. The number of DOFs is thus $M - Q$. This partially adaptive array is the same as that in [106].

Type 2: Each ring is further divided by taking at alternate the array elements on that ring to form 2 subarrays. The number of DOFs is increased to $2M - Q$.

Type 3: Each ring is split into two symmetric halves to form 2 subarrays. The adjacent rings are rotated by 90° to avoid similar directional spatial sampling patterns in all the subarrays. The number of DOFs is $2M - Q$.

Type 4: Each ring is divided by taking at alternate two adjacent elements on that

ring into 2 subarrays. The number of DOFs is $2M - Q$.

In this simulation study, we set \mathbf{h}_m in the partition matrix \mathbf{T} to be the delay-and-sum weights given in (3.6) in Chapter 3.

4.4.1 Adaptation Performance

A narrowband beamforming example is considered to study the adaptation performance of the partially adaptive arrays. The CRA consists of 4 equally spaced rings, where the smallest and the largest ring radii normalized to the wavelength of the center frequency are 0.2346 and 0.9382. The number of array elements is allocated as [12, 12, 20, 24] from the innermost to the outermost ring. Hence K is 68 and M is 4. The NLMS algorithm as shown in (4.21) - (4.22) is used for adaptation. The adaptation performance of the fully adaptive and the four types of partially adaptive arrays are examined, and their numbers of adapting coefficients are 67, 3, 7, 7 and 7 respectively.

The simulation scenario assumes the array has a look direction of $(0^\circ, 90^\circ)$ and the desired signal has unit energy. Three stationary directional interferences and ambient background noise are simulated. The DOAs of the three interferences are $(120^\circ, 75^\circ)$, $(150^\circ, 90^\circ)$ and $(220^\circ, 80^\circ)$, with the Signal-to-Interference Ratio (SIRs) being $-25dB$, $-35dB$ and $-30dB$ respectively. The Signal-to-Noise Ratio (SNR) of the ambient background noise is $0dB$. Based on 50 independent runs, the interference and noise power in the array outputs, p_{i+n} , for fully and partially adaptive arrays as a function of the number of iterations are plotted in Fig.4.4. The p_{i+n} values shown are normalized to the interference and noise power before adaptation begins and are given in dB unit. As adaptation proceeds, p_{i+n} in all adaptive arrays decrease gradually as the adaptive weights converge to the optimal solutions. To reveal more details of the trajectories, we calculated the locally averaged interference and noise power at a series of iteration numbers as shown below.

As can be seen from Fig. 4.4 and Table 4.2, fully adaptive array has the slowest

Iterations	Fully	Type 1	Type 2	Type 3	Type 4
100	1.3605	0.4277	0.6550	0.7699	1.6214
200	0.3132	0.0350	0.0946	0.1001	0.2761
300	0.1307	0.0286	0.0356	0.0374	0.0952
500	0.0431	0.0279	0.0191	0.0186	0.0295
1000	0.0171	0.0275	0.0176	0.0167	0.0178
3000	0.0152	0.0258	0.0170	0.0165	0.0174
5000	0.0151	0.0243	0.0168	0.0165	0.0174
<i>Theory</i>	0.0148	0.0203	0.0163	0.0160	0.0169

Table 4.2: Interference and noise power at some iteration numbers.

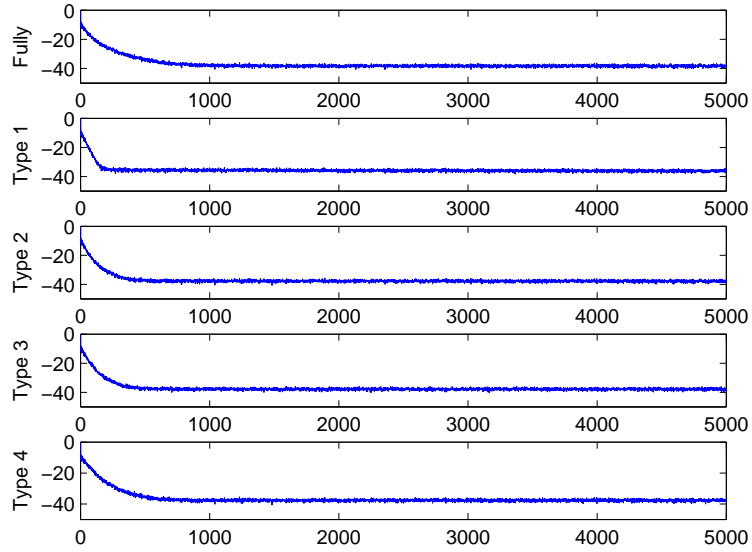


Figure 4.4: Interference and noise power in array outputs. Vertical axis: Normalized interference and noise power in dB, horizontal axis: number of iterations.

convergence rate and Type 1 partially adaptive array converges the fastest at the beginning. The convergence rates of Type 2, 3, and 4 partially adaptive arrays are comparable to each other. This is as expected since in general the convergence rates are inversely proportional to the number of DOFs. We have also calculated the theoretical interference and noise power at steady state using (4.30) and they are shown in the last row of Table 4.2. Note that except Type 1 partially adaptive array, all other arrays are able to approach within a very close range of the theoretical value at around 5000 iterations.

We have observed that Type 1 partially adaptive array was able to approach close to the theoretical value given more iterations. This could be due to the fact that Type 1 adaptive array may have a larger eigenvalue spread.

4.4.2 Comparison of Partitioning Schemes

In this subsection, we compare the steady state interference and noise cancellation performance of the four types of partially adaptive arrays. The same CRA in the previous subsection is used. The desired signal has unit energy and its DOA is denoted by (θ_0, ϕ_0) . The ambient background noise has a SNR of $0dB$. To simplify the study, there is only one interference whose DOA is denoted by (θ_i, ϕ_i) and the SIR is $-45dB$. In this simulation, the DOA of the interference is always maintained outside of the mainlobe of the beamformer so that the effect of different partition schemes on the residual interference and noise power can be demonstrated more clearly. One linear constraint is used to maintain a unity gain in the look direction.

We shall denote the steady state residual interference and noise power $p_{i+n,ss}$ at certain values of (θ_0, ϕ_0) and (θ_i, ϕ_i) as $p_{i+n,ss}(\theta_0, \phi_0, \theta_i, \phi_i)$. We define the average $p_{i+n,ss}$ and maximum $p_{i+n,ss}$ as

$$P_{ave} = \frac{\int_{\theta_0} \int_{\phi_0} \int_{\theta_i} \int_{\phi_i} p_{i+n,ss}(\theta_0, \phi_0, \theta_i, \phi_i) d\phi_i d\theta_i d\phi_0 d\theta_0}{\Theta_0 \Phi_0 \Theta_i \Phi_i}, \quad (4.31)$$

and

$$P_{max} = \max_{\theta_0, \phi_0, \theta_i, \phi_i} p_{i+n,ss}(\theta_0, \phi_0, \theta_i, \phi_i), \quad (4.32)$$

where the range for θ_0 is $[0, 2\pi]$ and ϕ_0 is $[0, \pi]$. The ranges for θ_i and ϕ_i are similar to those of θ_0 and ϕ_0 except the angles within the mainlobe of the beamformer are excluded. $\Theta_0, \Phi_0, \Theta_i, \Phi_i$ in (4.31) represent the widths of the integrals. The values of P_{ave} and P_{max} for the fully and Type 1-4 partially adaptive arrays are shown in Table 4.3.

The results indicate that the partially adaptive CRAs increase both P_{ave} and P_{max} as compared to the fully adaptive array. Type 1 array has the largest amount of increase.

	Fully	Type 1	Type 2	Type 3	Type 4
DOFs	67	3	7	7	7
P_{ave}	0.01475	0.01541	0.01532	0.01501	0.01506
P_{max}	0.01483	0.01892	0.01668	0.01673	0.01755

Table 4.3: Steady state residual interference and noise power.

However, the increase is only 4.5% in P_{ave} and 27.6% in P_{max} although the numbers of DOFs is about 20 times smaller than that of the fully adaptive array. Types 2-4 arrays have 7 DOFs and are able to yield smaller P_{ave} and P_{max} compared to Type 1. Type 3 array has the smallest P_{ave} and Type 2 has the smallest P_{max} among them. In practice, depending on whether the design priority is on the best averaged performance or on the tolerance of the worst performance, different partition schemes can be chosen accordingly.

4.4.3 Broadband Beamforming

The performance of the proposed partially adaptive array method is now examined for adaptive broadband beamforming. A CRA consisting of 204 array elements allocated on 10 rings is used [106]. The radii of the 10 rings normalized to the smallest radius are: [1, 2, 3, 4, 6, 8, 12, 16, 24, 32]. The smallest radius is 0.02m and the largest radius is 0.64m. The CRA uses nested array design as shown in Table 4.4, and it covers a frequency range from 200Hz up to 8KHz. The ring index is counting from the innermost ring.

Subband	Ring Index	Array Elements on Each Ring	Frequency Range
1	1 2 3 4	[12 16 20 24]	3.6 - 8KHz
2	2 4 5 6	[8 12 20 24]	1.8 - 3.6KHz
3	4 6 7 8	[12 12 20 24]	0.9 - 1.8kHz
4	6 8 9 10	[12 12 20 24]	0.2 - 0.9KHz

Table 4.4: Configuration of CRA in the nested array design.

The simulation scenario contains a desired signal and four interferences as summarized in Table 4.5. The desired signal is a bird sound with non-stationary behavior. The interferences are also non-stationary. The background noise is stationary and the SNR is $5dB$.

	Signal Type	SIR	DOA
Desired Signal	Bird Sound	NA	$(30^\circ, 85^\circ)$
Interference 1	Helicopter Noise	$-30dB$	$(200^\circ, 75^\circ)$
Interference 2	Tank Noise	$-35dB$	$(90^\circ, 90^\circ)$
Interference 3	Firetruck Noise	$-40dB$	$(350^\circ, 85^\circ)$
Interference 4	Jet Noise	$-30dB$	$(180^\circ, 60^\circ)$

Table 4.5: Desired signal and interferences.

The fully adaptive and the four types of partially adaptive arrays described earlier are implemented. One linear constraint is used to maintain a unity gain in the look direction. The average number of adaptive weights in the fully adaptive, Type 1 and Type 2-4 adaptive arrays are 67, 3 and 7 respectively in each frequency component of the FFT decomposition. The partially adaptive arrays are implemented using the RLS algorithm. The fully adaptive array is implemented using the NLMS algorithm since the RLS algorithm is computationally too costly due to the large number of adaptive weights.

The residual interference and noise of all types of arrays are shown in Fig. 4.5, where they are obtained from the difference between the desired signal and the corresponding array outputs. Type 1 partially adaptive array has the poorest performance because it only has 3 DOFs and is not able to remove all 4 interferences. The fully adaptive array is not performing well because the signal and interferences are highly non-stationary and its convergence rate is too slow to track changes in the signal characteristics. Types 2, 3 and 4 partially adaptive arrays yield similar convergence performance and are able to effectively remove the interferences. Type 3 array outperforms Type 2 and 4 arrays a little, which is consistent with the theory as indicated in Table 4.3.

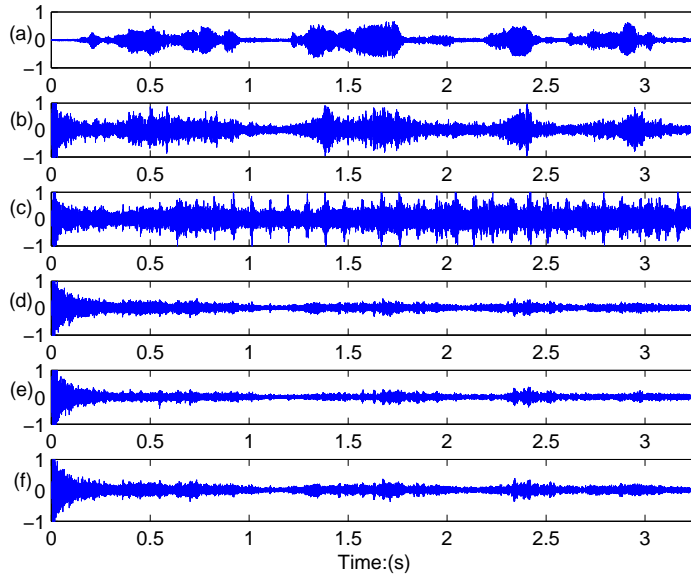


Figure 4.5: Processing results. (a) Desired signal. (b)-(f) Residual interference and noise in fully adaptive array and Type 1-4 partially adaptive array.

4.5 Summary

In this chapter, we discuss the adaptive beamforming using CRA. We first analyze the disadvantages of implementing the CRA as a fully adaptive array, which are slow convergence rate and high computational complexity. To solve these problems we propose a partially adaptive design. The design is based on element space partially adaptive approach. An important consideration in the element space approach is the choice of an appropriate partition scheme because it affects the convergence and the interference and noise cancellation performance. The proposed method accommodates arbitrary partition schemes and thus provides a basis for their comparison. We then derive the analytical form of the steady state residual interference and noise power and use it as an evaluation criterion for different partition structures. Simulations have verified the advantages of the proposed method.

Chapter 5

DOA Estimation Using Concentric Ring Array

Through out our design of deterministic and adaptive CRA in previous chapters, we have assumed that the DOA of the desired signal is known. In the deterministic design, we also assume the Directions of Arrival (DOA)s of interferences are known so that nulls can be placed in the beampattern. However, in practice, the DOAs of the incoming signals are generally unknown and need to be estimated.

DOA estimation problem has been a central topic in array processing for the past few decades due to its importance in a great variety of applications including radar and sonar, personal communications, teleconference, surveillance, underwater acoustics, and medical diagnosis/treatment, etc [107]. In this chapter we first review current DOA estimation techniques and then propose a broadband DOA estimation method for CRA. The performance of the proposed estimator is studied in detail and is evaluated by simulations.

The rest of this chapter is organized as below. Section 5.1 is a review of the DOA estimation techniques. Section 5.2 describes the proposed method. Study of the statistical performance of the proposed method is given in Section 5.3, followed by simulation results presented in Section 5.4. Finally, Section 5.5 is a summary.

5.1 Introduction to DOA Estimation

Depending on the spectrum of the signal of interest, the DOA estimation methods can be categorized as narrowband and broadband methods. These two types of methods are reviewed briefly in this section. In addition, DOA estimation techniques specifically proposed for circular arrays are also reviewed.

5.1.1 Narrowband DOA Estimation

Narrowband DOA estimation methods can be categorized as (1) Spectral-based and (2) Parametric approaches [107].

The Spectral-based approaches include DOA estimation based on beamforming techniques and Subspace-based methods. The former has small computation but suffers poor resolution [107]. Subspace-based methods are model-based, which requires the knowledge of the array signal model. By performing eigen-decomposition of the spatial covariance matrix of the array data, the array data signal space is decomposed into signal subspace and noise subspace. Direction finding algorithms can then be applied, such as Multiple Signal Classification (MUSIC) [108, 109] and ESPRIT [110] etc. When the source signals are correlated, the signal subspace cannot be determined correctly thus resulting in erroneous DOA estimates.

Parametric methods are developed by more fully exploiting the underlying signal generation process. The most well known parametric methods are Maximum Likelihood (ML) techniques [111, 112]. Based on the different statistical assumptions of the source signal, ML methods can be classified as Deterministic ML method and Stochastic ML method. The advantages of parametric methods are higher resolution and robustness to correlated signal sources. However, they generally involve multidimensional search, which makes them computationally unattractive.

5.1.2 Broadband DOA Estimation

DOA estimation for broadband signals can be divided into two classes: incoherent and coherent processing methods [113]. The incoherent processing methods are natural extensions of the narrowband estimation techniques described above. In such method, the broadband signals are first decomposed into many non-overlapping narrowband components, DOA estimation is then performed in each narrowband and the results from each narrowband are combined to form the broadband signal DOA estimates. These methods are computationally inefficient and they can not handle the cases when there are correlated signal sources.

The coherent signal subspace processing (CSS) methods are discussed in [113–116]. This kind of methods use focusing matrices to align the signal subspaces of the narrowband components and then combine the aligned signal subspace to form a single covariance matrix at some reference frequency. The subspace DOA estimation techniques for narrowband signal can then be performed on this single covariance matrix. Compared with incoherent method, CSS methods yield higher estimation accuracy and can handle correlated signals.

5.1.3 DOA Estimation Using Circular Arrays

Circular arrays are favored in many DOA estimation applications because (1) they can yield both azimuth and elevation angle estimates since they are 2-D arrays. (2) Comparing to other 2-D arrays, their symmetric structures provide nearly invariant beampattern for 360° azimuthal coverage. Many of the previous described DOA estimation techniques are suitable for arbitrary 2-D and 3-D array geometry and thus they can be applied to circular arrays directly. Nevertheless, much research effort has been made to either improve the efficiency of those “generic” techniques or to develop new techniques using specific features of circular arrays. Those results are briefly reviewed below.

[117,118] discuss application of uniform linear array bearing estimation techniques to uniform circular arrays (UCA's). The applicability of the ESPRIT principle in conjunction with rotationally invariant arrays (such as UCA's) was studied in [119]. In [120], Lau *et al.* improves the robustness of a transformation [58] that can create approximate Vandermonde form array manifold vector in UCA, so that beamforming and DOA estimation techniques for ULA can be applied to UCA.

In [121], the array manifold of a UCA is transformed to beamspace manifold through phase mode excitation-based beamformers, which leads to the development of two eigenstructure based estimation algorithms that operate in beamspace, namely, UCA-RB-MUSIC and UCA-ESPRIT. The latter yields computationally efficient 2-D angle estimation algorithm and its performance analysis can be found in [122].

In [123], a model-fitting approach is applied to DOA estimation with UCA that can improve drastically upon conventional beamformer and yields performance comparable to the best high-resolution techniques.

Direction finding of coherent signals for UCAs has been discussed in [124,125]. Evaluation of the statistic performance of MUSIC and ML estimator for azimuth and elevation narrowband DOA estimation using UCA can be found in [126,127].

5.2 Proposed Broadband DOA Estimation Method Using CRA

Most of the DOA estimation techniques for circular arrays assume narrowband scenario. They can be extended to broadband scenario using either incoherent or coherent approach. As pointed out earlier, incoherent approach has many disadvantages and it should be avoided. Implementation of coherent approach requires the design of focusing matrices at different frequencies, which can be a very challenging task. Moreover, applying CSS methods to CRA may involve a large amount of computation. This is

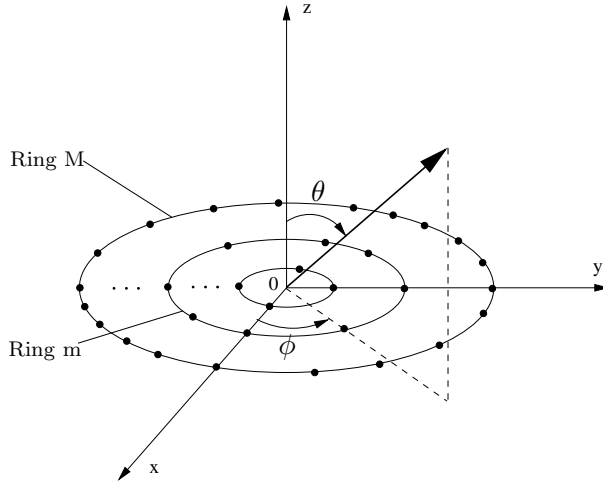


Figure 5.1: Configuration of a CRA.

because a typical CRA has several dozens to a few hundreds of array elements and the computation required to identify the signal subspaces through eigenvalue decomposition is very high for an array that has a large size.

Based on the work by Lee [1], we here propose a broadband DOA estimation technique specifically for CRA. The proposed method also takes the CSS approach but operates in beamspace, thus greatly reduces the computational complexity.

5.2.1 Signal Model

The configuration of a CRA is shown in Fig. 5.1, where ϕ denotes the azimuth angle and θ the elevation angle with respect to the z -axis. The array consists of M rings, and the numbering of the rings starts from the innermost one. The m -th ring has N_m equally spaced array elements and its radius is R_m , $m = 1 \dots M$. The total number of array elements is $K = \sum_{m=1}^M N_m$.

Consider the scenario of D broadband sources impinging on the CRA. The D sources are located in the far field of the CRA so that the plane wave assumption holds at all array elements. The received array signals are first divided into short frames. Using a bank of L bandpass filters, each data frame is then decomposed into L narrowband

components, centered at ω_l , $l = 1, \dots, L$. The array snapshot vector at frequency ω_l and n -th frame is [1]

$$\mathbf{x}(n; \omega_l) = \mathbf{A}(\omega_l)\mathbf{s}(n; \omega_l) + \mathbf{v}(n; \omega_l), \quad l = 1, 2, \dots, L, \quad (5.1)$$

where $\mathbf{s}(n; \omega_l)$ is a $D \times 1$ source signal vector. $\mathbf{v}(n; \omega_l)$ is a $K \times 1$ vector representing the additive spatially white noise present at all the array element. $\mathbf{A}(\omega_l)$ is a $K \times D$ source direction matrix, whose i -th column is the array manifold corresponding to the i -th source and has the form [1]

$$\mathbf{a}(\vec{r}, \omega_l) = [e^{j\omega_l \frac{\vec{r} \cdot \vec{\alpha}_1}{c}}, e^{j\omega_l \frac{\vec{r} \cdot \vec{\alpha}_2}{c}}, \dots, e^{j\omega_l \frac{\vec{r} \cdot \vec{\alpha}_K}{c}}]^T, \quad (5.2)$$

with $\vec{r} = \vec{r}_i$, where \vec{r}_i is the unit vector pointing at the i -th source from the array phase center. $\vec{\alpha}_k$ is the coordinate vector of the k -th array element with respect to the array phase center, and c is the propagation speed of the wave. Using the coordinate system defined in Fig. 5.1, (5.2) can be written as

$$\mathbf{a}_{i, \omega_l} = \mathbf{a}(\vec{r}_i, \omega_l) = [e^{\frac{j2\pi r_1}{\lambda_l} \sin \theta_i \cos(\phi_i - \gamma_1)}, e^{\frac{j2\pi r_2}{\lambda_l} \sin \theta_i \cos(\phi_i - \gamma_2)}, \dots, e^{\frac{j2\pi r_K}{\lambda_l} \sin \theta_i \cos(\phi_i - \gamma_K)}]^T, \quad (5.3)$$

where r_k is the distance between the k -th element and the origin and γ_k is its azimuth angle.

If a series of matrices \mathbf{T}_l , $l = 1, \dots, L$ exist, such that

$$\mathbf{T}_l \mathbf{A}(\omega_l) = \mathbf{A}(\omega_0), \quad l = 1, \dots, L, \quad (5.4)$$

then the source direction matrices at various frequency bins can be transformed into a single direction matrix at some pre-selected frequency ω_0 . Such \mathbf{T}_l , $l = 1, \dots, L$ are referred to as *focusing* matrices [1].

Using focusing matrices, the “focused” data covariance matrix can be formed as [1]

$$\begin{aligned}\bar{\mathbf{R}}_{xx} &= \sum_{l=1}^L \beta_l \mathbf{T}_l \mathbf{R}_{xx}(\omega_l) \mathbf{T}_l^H \\ &= \mathbf{A}(\omega_0) \bar{\mathbf{R}}_{ss} \mathbf{A}^H(\omega_0) + \bar{\mathbf{R}}_{vv}\end{aligned}\quad (5.5)$$

where

$$\mathbf{R}_{xx}(\omega_l) = E[\mathbf{x}(n; \omega_l) \mathbf{x}^H(n; \omega_l)] \quad (5.6)$$

$$\bar{\mathbf{R}}_{ss} = \sum_{l=1}^L \beta_l E[\mathbf{s}(n; \omega_l) \mathbf{s}^H(n; \omega_l)] \quad (5.7)$$

$$\bar{\mathbf{R}}_{vv} = \sum_{l=1}^L \beta_l \mathbf{T}_l E[\mathbf{v}(n; \omega_l) \mathbf{v}^H(n; \omega_l)] \mathbf{T}_l^H \quad (5.8)$$

and β_l is a set of pre-selected weights.

Narrowband DOA estimation techniques, such as MUSIC, can then be performed on this focused covariance matrix $\bar{\mathbf{R}}_{xx}$. Compared to incoherent processing methods, CSS methods achieve lower detection and resolution SNR threshold at reduced computational complexity. In addition, they can handle the correlated signal sources. A limitation of CSS methods is that they usually require preliminary DOA estimates to construct the focusing matrices, and erroneous preliminary estimates can result in large estimation bias in CSS methods [128].

5.2.2 Focusing Matrices Design Using Frequency Invariant CRA

Broadband DOA estimation in beamspace has the merit of reducing computation [129, 130]. In [1], Lee proposed a CSS method based on beamspace processing, in which beamforming matrices that yield identical beampatterns at different frequencies are used to align the signal subspaces of the narrowband components in beamspace for DOA estimation. Comparing to element space CSS methods, beamspace CSS (BS-CSS) method

yields similar performance and greatly reduces computation. Moreover, it requires no *a priori* knowledge of the spatial distribution of the broadband sources.

In [1], Lee uses a Least-Squares(LS) fit procedure to design frequency invariant (FI) beamformers. [89] and [131] follow Lee's DOA estimation approach but use different techniques to design FI beamformers. In [89], Ward *et al.* avoids frequency decomposition of array signal by implementing the FI beamformers through FIR filtering. [131] uses a simple FI design that is suitable for arbitrary array, however, the design lacks control on the sidelobe level and mainlobe width of the beampattern, which may compromise the quality of DOA estimate.

In Chapter 3, we proposed a design method (Method III) that can achieve desired FI array pattern for CRA at a range of frequencies. Using this beamformer design technique, we propose a beamspace broadband DOA estimation technique for CRA based on Lee's approach [1]. The proposed technique has the merit that no optimization process is required to obtain the FI beamformers and it can control the mainlobe width and sidelobe level of the beampattern.

In the proposed method, multiple beams are first formed over the interested DOA ranges. At each frequency bin ω_l , a $K \times P$ beamforming matrix $\mathbf{V}_l = [\mathbf{v}_{l1}, \mathbf{v}_{l2}, \dots, \mathbf{v}_{lP}]$ can be formed, where P is the number of beams and \mathbf{v}_{lp} is a $K \times 1$ vector representing the weights to form the p -th beam at frequency ω_l . The element space snapshot vector $\mathbf{x}(n; \omega_l)$ can thus be transformed to beamspace snapshot vector [1]

$$\mathbf{x}_B(n; \omega_l) = \mathbf{V}_l^H \mathbf{x}(n; \omega_l), l = 1, \dots, L. \quad (5.9)$$

The number of beams P needs to satisfy $P > D$ in order to resolve all D signal sources. At the same time, P is usually chosen to be less than K so that the beamspace has a smaller dimension compared to element space and reduction of computation can be achieved.

Putting (5.1) into (5.9) yields

$$\mathbf{x}_B(n; \omega_l) = \mathbf{B}(\omega_l)\mathbf{s}(n; \omega_l) + \mathbf{v}_B(n; \omega_l), \quad l = 1, \dots, L. \quad (5.10)$$

where

$$\mathbf{B}(\omega_l) = \mathbf{V}_l^H \mathbf{A}(\omega_l), \quad l = 1, \dots, L \quad (5.11)$$

and

$$\mathbf{v}_B(n; \omega_l) = \mathbf{V}_l^H \mathbf{v}(n; \omega_l), \quad l = 1, \dots, L \quad (5.12)$$

The columns of \mathbf{V}_l are FI beamformer weights obtained by using the FI beamformer design method described in Chapter 3. Hence, the left side of (5.11) will approximate the same beamspace direction matrix at a pre-selected frequency ω_0 , i.e.,

$$\mathbf{B}(\omega_l) \approx \mathbf{B}(\omega_0), \quad l = 1, \dots, L. \quad (5.13)$$

where $\mathbf{B}(\omega_0)$ is the beamspace DOA matrix at ω_0 .

In the same manner of forming the focused covariance matrix in element space, a focused covariance matrix of the beamspace data can be formed as [1]

$$\begin{aligned} \bar{\mathbf{Q}}_{xx} &= \sum_{l=1}^L \beta_l E[\mathbf{x}_B(n; \omega_l) \mathbf{x}_B^H(n; \omega_l)] \\ &= \mathbf{B}(\omega_0) \bar{\mathbf{R}}_{ss} \mathbf{B}^H(\omega_0) + \bar{\mathbf{Q}}_{vv} \end{aligned} \quad (5.14)$$

where $\bar{\mathbf{R}}_{ss}$ is as defined in (5.7) and

$$\begin{aligned} \bar{\mathbf{Q}}_{vv} &= \sum_{l=1}^L \beta_l E[\mathbf{v}_B(n; \omega_l) \mathbf{v}_B^H(n; \omega_l)] \\ &= \sum_{l=1}^L \beta_l \mathbf{V}_l^H E[\mathbf{v}(n; \omega_l) \mathbf{v}^H(n; \omega_l)] \mathbf{V}_l \end{aligned} \quad (5.15)$$

Assuming the additive noise received at each array element is spatially white and has a common variance σ_l^2 , i.e., $E[\mathbf{v}(n; \omega_l) \mathbf{v}^H(n; \omega_l)] = \sigma_l^2 \mathbf{I}, l = 1, 2, \dots, L$. Under this assumption, (5.15) becomes

$$\bar{\mathbf{Q}}_{vv} = \sum_{l=1}^L \beta_l \sigma_l^2 \mathbf{V}_l^H \mathbf{V}_l \quad (5.16)$$

If \mathbf{V}_l is constructed such that its columns are orthonormal, i.e.

$$\mathbf{V}_l^H \mathbf{V}_l = \mathbf{I} \quad (5.17)$$

(5.16) is reduced to

$$\bar{\mathbf{Q}}_{vv} = \sum_{l=1}^L \beta_l \sigma_l^2 \mathbf{I} = \bar{\sigma}^2 \mathbf{I} \quad (5.18)$$

where $\bar{\sigma}^2 = \sum_{l=1}^L \beta_l \sigma_l^2$ is the weighted sum of noise variance at different frequencies. In the following derivation, we assume (5.18) holds. Narrowband DOA estimation methods can be applied on $\bar{\mathbf{Q}}_{xx}$, which is of size $P \times P$. When $P \ll K$, a great reduction of computation is achieved.

Performing eigen-decomposition of $\bar{\mathbf{Q}}_{xx}$ yields

$$\bar{\mathbf{Q}}_{xx} = \mathbf{U} \mathbf{\Lambda} \mathbf{U}^H \quad (5.19)$$

where $\mathbf{\Lambda} = \text{diag}\{\lambda_1, \lambda_2, \dots, \lambda_P\}$ is a diagonal matrix with $\lambda_1 \geq \lambda_2 \geq \dots \geq \lambda_P$ being the eigenvalues in descending order, and \mathbf{U} is the corresponding eigenvector matrix. From the assumption in (5.18), there are $P - D$ eigenvalues equal to $\bar{\sigma}^2$ and the rest D eigenvalues are larger, i.e. $\lambda_1 \geq \lambda_2 \geq \dots \geq \lambda_D > \lambda_{D+1} = \lambda_{D+2} = \dots = \lambda_P = \bar{\sigma}^2$. Accordingly, the eigenvectors in \mathbf{U} can be partitioned into two sets: the noise eigenvectors that correspond to $\lambda_{D+1}, \lambda_{D+2}, \dots, \lambda_P$ and the signal eigenvectors that correspond to $\lambda_1, \lambda_2, \dots, \lambda_D$. Hence, $\bar{\mathbf{Q}}_{xx}$ can be written as [107]

$$\bar{\mathbf{Q}}_{xx} = \mathbf{U}_s \mathbf{\Lambda}_s \mathbf{U}_s^H + \mathbf{U}_n \mathbf{\Lambda}_n \mathbf{U}_n^H \quad (5.20)$$

The noise eigenvectors \mathbf{U}_n span the noise space, which is the orthogonal complement of the signal space spanned by \mathbf{U}_s . Thus \mathbf{U}_n is orthogonal to the beamspace DOA matrix $\mathbf{B}(\omega_0)$. Define the projection matrix onto the noise space spanned by \mathbf{U}_n as [107]

$$\mathbf{\Pi}^\perp = \mathbf{U}_n \mathbf{U}_n^H = \mathbf{I} - \mathbf{B}(\omega_0) [\mathbf{B}^H(\omega_0) \mathbf{B}(\omega_0)]^{-1} \mathbf{B}^H(\omega_0). \quad (5.21)$$

In practice, the true statistics used above needs to be estimated, which are usually obtained through time sample averaging by assuming time ergodicity of the signal. Suppose an estimate $\hat{\Pi}^\perp$ of the noise space projection matrix is obtained, a MUSIC spatial spectrum can be calculated [107]

$$P(\phi, \theta) = \frac{\mathbf{b}^H(\phi, \theta)\mathbf{b}(\phi, \theta)}{\mathbf{b}^H(\phi, \theta)\hat{\Pi}^\perp\mathbf{b}(\phi, \theta)}, \quad (5.22)$$

and the D peaks of $P(\phi, \theta)$ correspond to the DOAs of the D sources. An exhaustive 2-D search of $P(\phi, \theta)$ is necessary to locate these D peaks.

Note that when the number of frequency bins $L = 1$, the proposed method reduced to a narrowband beamspace estimation method.

5.3 Statistical Performance Analysis

The performance of an estimator is usually examined in two aspects: (1) Whether the estimator is unbiased, (2) The amount of its estimation variance. A desirable estimator should be unbiased and has acceptable small estimation variance. Cramer-Rao Lower Bound (CRLB) specifies the lowest variance an unbiased estimator can achieve, thus it provides a useful tool to investigate the statistical performance of an estimator.

Study of CRLB of the MUSIC and ML methods for narrowband DOA estimation can be found in [132–134]. CRLB of 2-D angle estimation using 2-D array is discussed in [135]. [126, 127] analyze the statistic performance of narrowband MUSIC and ML estimator for 2-D angle DOA estimation using UCA.

Statistical performance of broadband DOA estimation techniques is discussed in [114, 131, 136–138]. [114] uses coherent processing technique to perform broadband DOA estimation and derives a broadband CRLB of its method. [137] derives the CRLB for broadband DOA estimation using ULA. [138] first constructs a stacked data vector using snapshot data vectors from all frequency bins, and then use the covariance matrix of

the stacked data vectors to analyze the CRLB of wideband source localization and DOA estimation for single source. [138] also derives the CRLBs for source localization and DOA estimation specifically for UCA. Different from [138], [131] uses coherent processing techniques to form a single covariance matrix at some reference frequency and use this covariance matrix to derive the variance of the DOA estimator.

5.3.1 Cramer-Rao Lower Bound Analysis

Denote a set of random variables by χ , its probability density function conditioned on Θ is given by $p(\chi|\Theta)$, where $\Theta = (\theta_1, \theta_2, \dots, \theta_d)$ is a set of parameters. Let $\hat{\Theta}$ be the estimate of Θ . The CRLB of the estimator $\hat{\Theta}$ is [114],

$$CRLB(\hat{\Theta}) = \mathbf{J}^{-1}(\Theta) \quad (5.23)$$

where $\mathbf{J}(\Theta)$ is the Fisher information matrix defined by

$$[\mathbf{J}(\Theta)]_{i,j} = -E\left[\frac{\partial^2 \log p(\chi|\Theta)}{\partial \theta_i \partial \theta_j}\right], \quad i, j = 1, \dots, d. \quad (5.24)$$

The CRLB for estimating the azimuth and elevation angles of a single source using a CRA is described below. In such a case, the random variables are $\mathbf{x}(n; \omega_l)$, $n = 1, \dots, Q$ and $l = 1, \dots, L$, where Q is the total number of frames in time domain. The parameter to be estimated is the 2-D angle pair (ϕ, θ) .

At each frequency bin, $\mathbf{x}(n; \omega_l)$, $n = 1, \dots, Q$ is assumed to be gaussian variables with zero mean and its correlation matrix is given by $\mathbf{R}_{xx}(\omega_l) = E[\mathbf{x}(n; \omega_l)\mathbf{x}^H(n; \omega_l)]$. The log-likelihood function of $\chi(\omega_l) = \{\mathbf{x}(n; \omega_l)\}$, $n = 1, \dots, Q$ is [114]

$$\log p(\chi(\omega_l)|\phi, \theta) = a - \log \det[\mathbf{R}_{xx}(\omega_l)] - \text{tr}[\hat{\mathbf{R}}_{xx}(\omega_l)\mathbf{R}_{xx}^{-1}(\omega_l)] \quad (5.25)$$

where $\hat{\mathbf{R}}_{xx}(\omega_l) = Q^{-1} \sum_{n=1}^Q \mathbf{x}^H(n; \omega_l)\mathbf{x}(n; \omega_l)$ is the sample correlation matrix of $\mathbf{x}(n; \omega_l)$ and a is a constant independent of ϕ and θ .

The frequency components $\mathbf{x}(n; \omega_l)$ are asymptotically independent and complex normal with zero-mean [114]. Thus the log-likelihood function of $\chi = \{\chi(\omega_l)\}$ is the sum of log-likelihood function from each frequency bin, i.e.

$$\log p(\chi|\phi, \theta) = \sum_{l=1}^L \log p(\chi(\omega_l)|\phi, \theta) \quad (5.26)$$

Putting (5.26) into (5.24) yields [139]

$$[\mathbf{J}(\Theta)]_{i,j} = \sum_{l=1}^L \text{tr} \left\{ \frac{\hat{\mathbf{R}}_{xx}(\omega_l)}{\partial \theta_i} \mathbf{R}_{xx}^{-1}(\omega_l) \frac{\hat{\mathbf{R}}_{xx}(\omega_l)}{\partial \theta_j} \mathbf{R}_{xx}^{-1}(\omega_l) \right\} \quad (5.27)$$

Denote the estimator of azimuth angle by $\hat{\phi}$ and the estimator of elevation angle by $\hat{\theta}$. Using results from [134], the CRLBs of $\hat{\phi}$ and $\hat{\theta}$ for the CRA are

$$CRLB(\hat{\phi}) = [KQG \sin^2(\theta) \sum_{m=1}^M R_m^2 N_m]^{-1} \quad (5.28)$$

and

$$CRLB(\hat{\theta}) = [KQG \cos^2(\theta) \sum_{m=1}^M R_m^2 N_m]^{-1} \quad (5.29)$$

with

$$G = \frac{1}{c^2} \sum_{l=1}^L \omega_l^2 \frac{(p_l/n_l)^2}{1 + K(p_l/n_l)}, \quad (5.30)$$

where p_l and n_l are the signal and noise power at frequency bin ω_l respectively.

The $CRLB(\hat{\theta})$ and $CRLB(\hat{\phi})$ are independent of ϕ . This is because the CRA has a symmetric structure in the azimuth plane. The CRLBs in (5.28) and (5.29) also suggest that when the DOA moves closer to the azimuth plane, the variance of the azimuth angle estimates becomes smaller and the variance of the elevation angle estimates becomes larger.

Comparison of (5.28) and (5.29) indicates that

$$\begin{aligned} CRLB(\hat{\phi}) &> CRLB(\hat{\theta}), \text{ if } \theta < 45^\circ \\ CRLB(\hat{\phi}) &= CRLB(\hat{\theta}), \text{ if } \theta = 45^\circ \\ CRLB(\hat{\phi}) &< CRLB(\hat{\theta}), \text{ if } \theta > 45^\circ. \end{aligned} \quad (5.31)$$

5.4 Experimental Results

In this section, we use simulations to investigate the performance of the proposed broadband DOA estimator for CRA. The CRA considered in this section has the same configuration as the one described in Section 3.6.3 in Chapter 3, which has 12 rings and a total number of 270 elements.

5.4.1 Narrowband Beamspace

We first look at the performance of the proposed beamspace DOA estimator in narrowband scenario.

The received array signal is generated in frequency domain at $2000Hz$, which contains a stationary directional signal and white gaussian noise. The source signal is assumed to be in the far-field and the DOA is $(\phi = 45^\circ, \theta = 60^\circ)$.

The desirable beampattern of the CRA is a Chebyshev function of order 8 [87] and has a $-30dB$ sidelobe level. The look directions are the grids formed by the following azimuth and elevation angle values: $\phi = [0^\circ : 10^\circ : 90^\circ]$ and $\theta = [45^\circ, 70^\circ, 90^\circ]$. The total number of beams generated is 30 and they cover the area of interest.

By setting the number of frequency bins to 1, the proposed broadband DOA estimator becomes a narrowband beamspace DOA estimator. It is then used to generate the MUSIC spectrum as defined in (5.22) and a 2-D searching algorithm is applied to the 2-D spectrum to locate the peak. A total of $Q = 256$ samples are used for the estimation. Based on 20 independent runs, we plot the root mean squares error (RMSE) of the azimuth and elevation angle estimates at various SNRs in Fig. 5.2. The CRLB of calculated from (5.28) and (5.29) are also plotted for reference.

From the Fig. 5.2 we can see the beamspace estimator has small RMSE values. The estimation error of the azimuth angle is lower than that of the elevation angle, which is consistent with (5.31) as the elevation angle is larger than 45° . The RMSEs

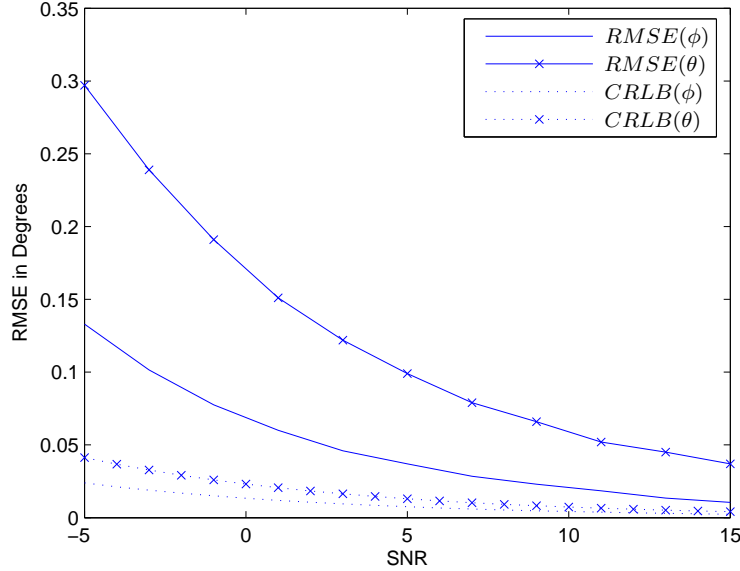


Figure 5.2: Narrowband beamspace estimator: RMSEs in degrees vs. SNR.

of the estimator approach the CRLBs in the high SNRs but can not attain them. The RMSEs can be further reduced by increasing the number of beams, however, doing so greatly increase the computational complexity and lose the merit of the beamspace processing method. Moreover, putting too many the beams in a given area may also violate the orthonormal condition in (5.17). This is because the beams have certain mainlobe width, putting different beams too close to each other will cause overlapping between their mainlobes and resultantly the orthonormal condition in (5.17) will be violated, which may lead to degraded performance.

5.4.2 Proposed Broadband Beamspace Method

In the second simulation, the source signal has certain bandwidth and the proposed broadband DOA estimator is used. The source signal is generated in frequency domain, it is a stationary directional signal with flat spectrum from $1000Hz$ to $2000Hz$. The background noise is white gaussian noise. The source signal is assumed to be in the far-field and the DOA is $(\phi = 45^\circ, \theta = 60^\circ)$. 512 point-FFT is used, there are a total

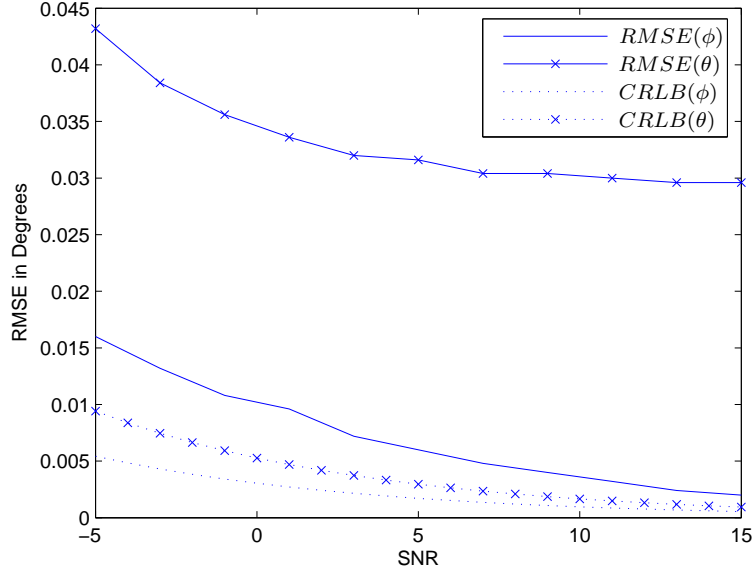


Figure 5.3: Coherent broadband estimator: RMSEs in degrees vs. SNR.

of 33 frequency bins within the signal’s frequency range. At each frequency bin, we generate 30 beams with frequency invariant property using Method III proposed in 3. The look directions of the 30 beams are the same as in the previous simulation.

The length of the frequency samples is $T = 256$. The proposed broadband DOA estimation method is then applied, the reference frequency f_0 is chosen at the middle of the frequency range. The RMSEs of the estimation results based on 20 independent runs are shown in Fig. 5.3 together with the corresponding CRLBs.

Comparing Fig. 5.3 with the narrowband scenario in Fig. 5.2, we can see the estimation results improved because of the information from more frequency bins are included. Same as in Fig. 5.2, the RMSE of the azimuth angle estimation is smaller than that of the elevation angle and it approaches the CRLB in high SNR region. Several factors may degrade the performance of estimator. First, the number of beams is limited. Secondly, due to design limitations, the orthonormal condition in (5.17) is not strictly satisfied. Thirdly, the frequency invariant array pattern design is not perfect, thus (5.4) can only be approximated.

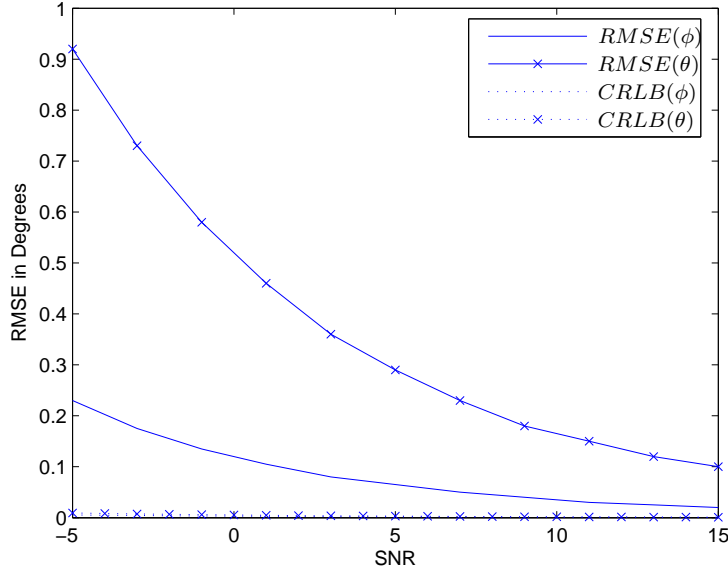


Figure 5.4: Incoherent broadband estimator: RMSEs in degrees vs. SNR.

For comparison, we also implemented an incoherent broadband 2-D angle estimator. At each frequency bin, we perform the narrowband beamspace method described in Section 5.4.1 to generate a narrowband MUSIC spectrum. The MUSIC spectrum from all frequency bins are then averaged and this averaged MUSIC spectrum is used for angle estimation. The signal scenario is the same as the previous simulation in this section. The RMSEs of the estimation results based on 5 independent runs are shown in Fig. 5.3.

Comparing Fig. 5.4 with Fig. 5.3 clearly indicates the advantage of the coherent broadband estimator in estimation accuracy. Note that in the incoherent broadband method, the computational complexity is almost $L = 33$ times that of the coherent broadband method. It is because the eigen-decomposition needs to be calculated at every frequency bin in the incoherent method while only once in the coherent broadband method.

5.4.3 Correlated Sources

In the last simulation, we demonstrate the performance of the proposed broadband DOA estimator for correlated sources.

Two far field sources signals are simulated, the first signal $s_1(t)$ is from the direction $(\phi_1 = 45^\circ, \theta_1 = 60^\circ)$ and the second signal $s_2(t)$ is from the direction $(\phi_2 = 40^\circ, \theta_2 = 50^\circ)$. $s_1(t)$ is a stationary signal with flat spectrum from $1000Hz$ to $2000Hz$. $s_2(t)$ is a delayed version of $s_1(t)$, i.e, $s_2(t) = s_1(t - \tau)$ with $\tau = 0.5s$. The background noise is white gaussian noise. Both signals have a $SNR = 10dB$. The number of samples is 256.

First, using the narrowband beamspace estimator in Section 5.4.1, we generate the MUSIC spectrum as shown in Fig. 5.5. There is only one peak lies between the true locations of the two source signals. Obviously, the narrowband estimator fails to estimate the correlated source signals. This is a well-known limitation of narrowband subspace method. They are ineffective to estimate the directions of correlated sources, because the correlated sources will degenerate the signal subspace. Note that the incoherent broadband method in previous section cannot yield correct estimates either, since incoherent broadband method also relies on the narrowband MUSIC spectrum.

We then apply the same coherent broadband estimator from previous section to generate the MUSIC spectrum as shown in Fig. 5.6. The MUSIC spectrum shows two peaks near the true locations of the two source signals. Based on 10 independent runs, we obtain estimates of the two source locations as $(\hat{\phi}_1 = 44.25^\circ, \hat{\theta}_1 = 58.02^\circ)$ and $(\hat{\phi}_2 = 39.65^\circ, \hat{\theta}_2 = 49.46^\circ)$, which are very close to the true locations.

5.5 Summary

In this section, we proposed a broadband DOA estimation method for the CRA. First, the proposed method takes the beamspace approach, thus greatly reduces the computation. Secondly, the propose method uses the frequency invariant beamformer design

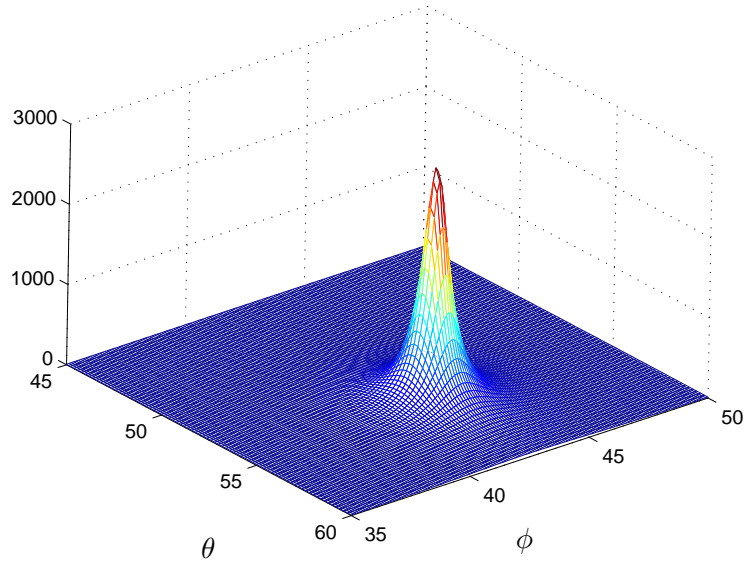


Figure 5.5: Narrowband estimator: MUSIC spectrum of two correlated sources.

method we proposed in Chapter 3 to align the beamspace covariance matrices obtained at different frequency bins to form a focused beamspace covariance matrix. Narrowband estimation technique can then be applied to the focused beamspace covariance matrix. Comparing the an incoherent broadband estimation method, our proposed broadband DOA estimation method requires much less computation, significantly improves the estimation accuracy and has the capability to estimate correlated sources.

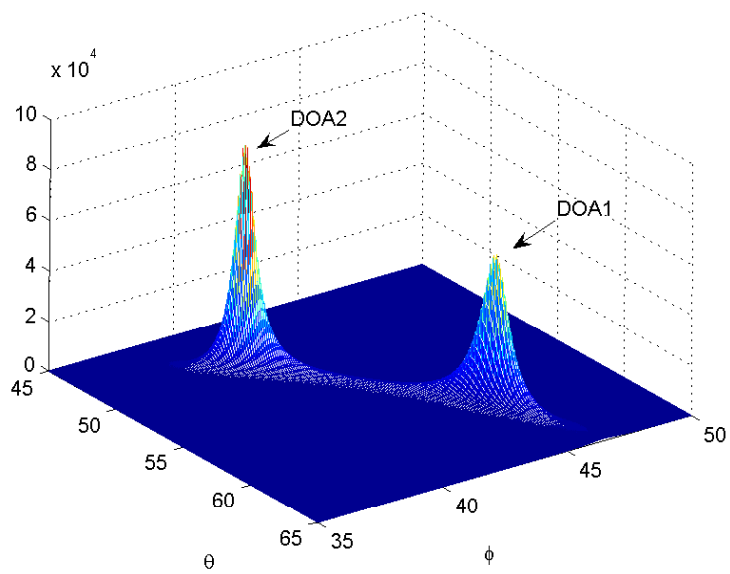


Figure 5.6: Proposed coherent broadband estimator: MUSIC spectrum of two correlated sources.

Chapter 6

Application of Concentric Ring Array in Bird Monitoring

Collisions between aircraft and birds have become an increasing concern for human health and safety. According to statistics from the Federal Aviation Administration (FAA), there were over 33,000 bird strikes reported to civil aircraft between 1990 and 2000, and about 15% of all bird strikes result in aircraft damage. Since 1960, about 400 aircraft have been destroyed and over 370 people killed as a result of bird and other wildlife strikes [97,140]. To minimize the number of bird strikes, microphone arrays have been used to monitor birds near the airport or some critical locations in the airspace. The received signals can be further processed to help identifying the bird species, this is important because some bird species are considered most hazardous to aircraft in certain area. However, the range of existing arrays is only limited to a few hundred meters. Moreover, the bird species identification performance in low signal-to-noise environment is not satisfactory.

Under the support of the US Air Force, Intelligent Automation, Incorporated (IAI) and the University of Missouri at Columbia, propose a novel system to improve bird monitoring and recognition system in noisy environments. First, a CRA is used to provide very directional and long range (a few thousand meters) acquisition of bird sounds.

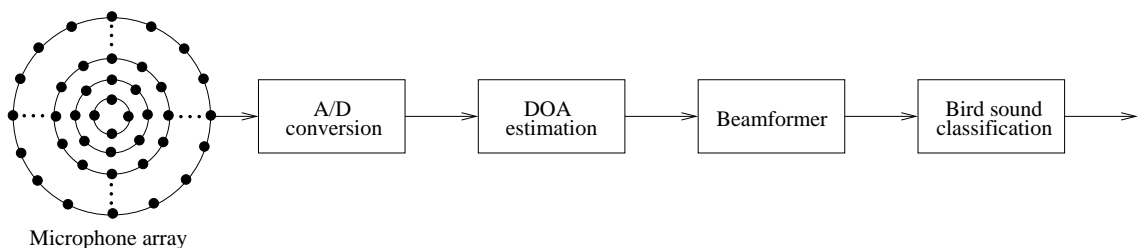


Figure 6.1: Proposed automated bird monitoring and recognition system.

Second, an efficient bird species recognition algorithm is proposed which uses Hidden Markov Model (HMM) and Gaussian Mixture Models (GMM). The overall system is suitable for real-time monitoring and recognition for a large number of birds.

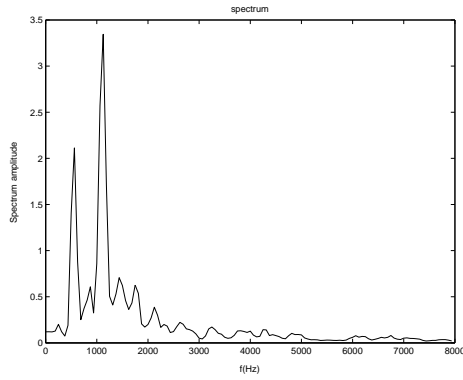
In this chapter, we first briefly describe the overall bird monitoring system in Section 6.1. In Section 6.2, we present a CRA based on Method I proposed in Chapter 3 for bird sound acquisition, which is first tested by simulations and then implemented in hardware and tested by field data. These experimental results are also presented.

6.1 Overall System Description

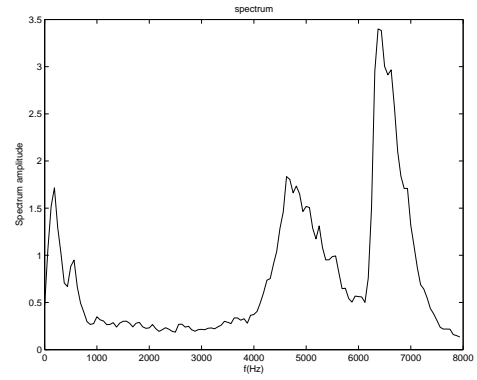
Fig. 6.1 shows the proposed system diagram, which consists of a CRA, followed by a data acquisition system, and then the software algorithms including DOA estimation, beamforming and bird sound classification.

The design of the CRA and its beamforming algorithms have been discussed in previous chapters and will not be repeated here. The data acquisition system and the bird classification algorithm are developed by IAI [97, 141], they will not be discussed here.

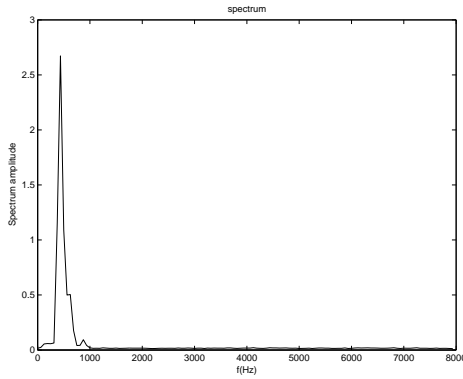
A beamformer requires the DOAs of the directional signals for beamforming to enhance the desired signal or to remove interference. The DOAs of the signal and interference are not known in practice and need to be estimated. In the simulations, we adopt the Multiple Signal Classification (MUSIC) [108, 109] algorithm for DOA estimation.



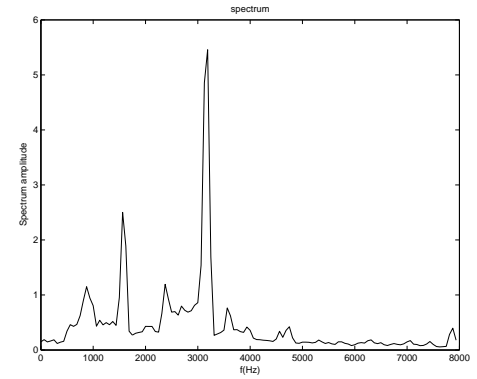
(a) Canadian goose



(b) Sparrow



(c) Dove



(d) Gull

Figure 6.2: Spectrum of some bird species. Spectrum computed using 256 point FFT.

6.2 Experimental Results

In this section, we first describe the configuration of the proposed CRA. The beamforming results obtained from both simulated data and field data are then presented.

6.2.1 Array Configuration

Fig. 6.2 shows the spectrum of the sound of some hazardous bird species. From the figure, it can be seen that most of the energy of those bird sounds concentrates in the frequency range of $200 - 8kHz$. Thus the operating frequency of the bird monitoring array should have the same range. To cover such a wide frequency range, the nested array design as presented in Section 3.4.1 of Chapter 3 is adopted, which divides the

whole array into different subarrays to cover different frequency subbands.

The proposed array consists of 64 array elements allocated among 10 rings. The radii of the rings and the distribution of array elements is summarized in Table 6.1.

Ring No.	1	2	3	4	5	6	7	8	9	10
Radius	R_1	$2R_1$	$3R_1$	$4R_1$	$6R_1$	$8R_1$	$12R_1$	$16R_1$	$24R_1$	$32R_1$
No. of array elements	4	4	6	8	6	8	6	8	6	8

Table 6.1: Radii of each ring and array elements distribution.

The 10 rings are grouped into 4 subarrays. As shown in Table. 6.2, each subarray has an original operating frequency and by using the Method I proposed in Section 3.4.1 it can cover a certain frequency range. The 4 subarrays altogether covers the interested frequency range of $200 - 8kHz$.

Subarray No.	Ring No.	Original operating frequency	Frequency range
1	1 2 3 4th	$4kHz$	$3600 - 8kHz$
2	2 4 5 6th	$2kHz$	$1800 - 3600Hz$
3	4 6 7 8th	$1kHz$	$900 - 1800Hz$
4	6 8 9 10th	$500Hz$	$200 - 900Hz$

Table 6.2: Grouping of subarrays and their configuration, numbers in round bracket indicates the array elements are shared with other subarrays.

The largest radius R_{10} is calculated using (3.16), which yields

$$R_{10} = \frac{\delta_4 \lambda_{500Hz}}{4\pi} = 0.64m$$

where δ_4 is the 4th root of the Bessel function $J_0()$ and is equal to 11.79. The radius of the 1st ring is found to be $R_1 = R_{10}/32 = 0.02m$.

6.2.2 Simulation Results

Given the limited number of array elements, the overall sidelobe level is chosen to be $-10dB$ and a Chebyshev function is used as the desired beampattern function. Using Method I proposed in Section 3.4.1, we generate the 2-D beampattern when the DOA of the signal is $(\theta_0 = 45^\circ, \phi_0 = 60^\circ)$. The beampatterns for some sampled frequencies

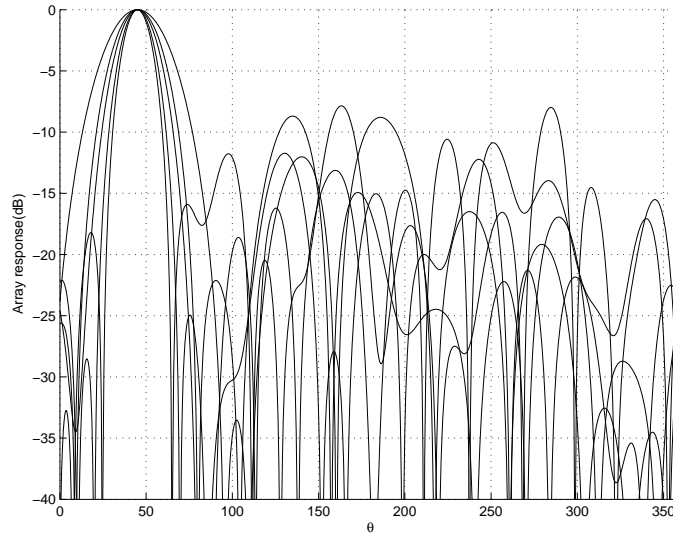


Figure 6.3: 2-D Beampatterns in the 2nd subarray: curves starting from the outside one are beampatterns at frequencies: $900Hz$, $1100Hz$, $1300Hz$, $1500Hz$ and $1700Hz$ respectively. The main look direction in this 2-D beampattern is $\theta = 45^\circ$

in the 2nd subarray are shown in Fig. 6.3, where the curves, starting from the outside one counted in the mainlobe, are beampatterns at $900Hz$, $1100Hz$, $1300Hz$, $1500Hz$ and $1700Hz$ respectively. The 2-D beampattern presented here is the surface $\phi = 60^\circ$ cutting through the look direction. The beampatterns for other subarrays are nearly identical. As can be seen from the figure, the beampatterns fulfill the design objective of $-10dB$ sidelobe level.

We then consider two simulated scenarios for bird sound acquisition. In the first scenario, the array signal contains a bird sound of interest plus interference and background noise. The bird sound is the sound of Canadian goose coming from the direction $(\theta = 45^\circ, \phi = 60^\circ)$. The interference is the sound generated by a plane taking off, coming from the direction $(\theta = 115^\circ, \phi = 80^\circ)$, and the SIR is $-20dB$. The background noise has a SNR of $0dB$. The interference and background start to appear at $t = 0.5s$. The second scenario assumes the same signal environment as the first scenario except an additional interference starts to appear at $t = 0.5s$, which is the sound of sparrows from the direction $(\theta = 270^\circ, \phi = 45^\circ)$ and the SIR is $-10dB$. In both scenarios, the

method proposed in Section 3.5.3 is used to generate nulls in the beampattern to cancel the interferences. The processing results for these two scenarios are presented in Fig. 6.4 and Fig. 6.5. From the figure, it is seen that in both scenarios most of the interference and background noise have been removed.

6.2.3 Field Data Testing Results

The proposed array is then implemented in hardware. As shown in Fig. 6.6, 64 microphones are placed in circles on a wood board to form a microphone dish, which is used to collect data in an open field (parking lot). Two loud speakers placed at about 40ft from the microphone dish serve as two sound sources, one is playing the bird sound and the other is playing plane noise as interference. The bird sound being played is either the sound of Canadian goose or the sound of chip sparrow, classification algorithms will be applied later to judge the bird species. The direction of the loud speakers with respect to the microphone dish is arbitrary and unknown to the beamformer. The output from the microphone dish is immediately fed into a data acquisition system, which performs A/D conversion and then transforms the discrete data to a computer [97]. After the data is stored in a computer, we first use the MUSIC algorithm to estimate the number of directional signals and the corresponding DOAs, and then use the previously described beamforming algorithm to process the array signal. We present processing results from two set of data below.

In the first set of data, estimation results from MUSIC algorithm shows there are two directional signals in the received array data, their DOAs are $(\theta = 320^\circ, \phi = 19^\circ)$ and $(\theta = 165^\circ, \phi = 43^\circ)$. We alternately assume one of the two DOAs as the main look direction of the beamformer and perform the beamforming. By listening to both outputs we are able to identify one of the directional signal is the bird sound of interest and the other is an interference. The enhanced bird sound together with the noisy array signal are shown in Fig. 6.7. In the second set of data, estimated results from MUSIC

algorithm shows there are also two directional signals in the received array data, their DOAs are $(\theta = 171^\circ, \phi = 30^\circ)$ and $(\theta = 329^\circ, \phi = 39^\circ)$. The processing results are shown in Fig. 6.8. The beamformer outputs in both sets of data are greatly improved. Besides the results presented here, many other tests using field data are conducted, all of them show substantial improvement in the beamformer outputs.

The bird sound used is either the sound of Canadian goose or the sound of chip sparrow. Bird classification algorithm is applied to distinguish the bird species. In the classification process, the bird sound signals are matched with the sound models of Canadian goose and chip sparrow, the model with higher probability will be output as decision. Both the signal before and after beamforming are used for classification, the results are summarized in Table 6.3 and 6.4.

	Prob. as Canadian goose	Prob. as chip sparrow	Decision
Canadian goose	-107.2907	-118.1171	Canadian goose
Chip sparrow	-121.6638	-117.6680	Chip sparrow

Table 6.3: Classification results before beamforming.

	Prob. as Canadian goose	Prob. as chip sparrow	Decision
Canadian goose	-100.9485	-149.3710	Canadian goose
Chip sparrow	-131.2033	-92.4776	Chip sparrow

Table 6.4: Classification results after beamforming.

From the table, we can see the classification algorithm is able to make correct decisions with or without beamforming. However, the difference between matching probability is much smaller without beamforming comparing to the case of using beamforming, which indicates it is very difficult to set thresholds if beamforming is not used.

6.3 Summary

In this chapter, we describe the application of a CRA to bird monitoring. The research is still under development, presented here are some of the preliminary results. However,

it can be seen the work is fruitful and has great potential for further improvement.

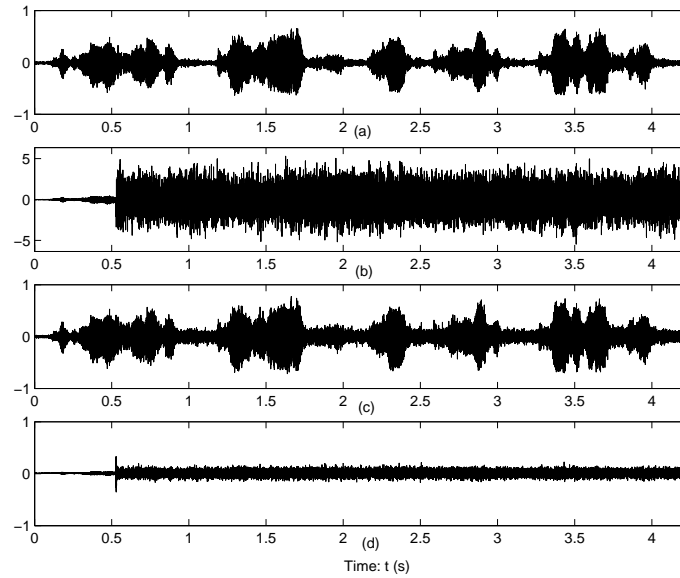


Figure 6.4: Processing results for scenario 1: (a) Desired signal $s(t)$; (b) Received noisy signal in one channel; (c) Beamformer output $z_1(t)$; (d) Error signal: $e_1(t) = z_1(t) - s(t)$.

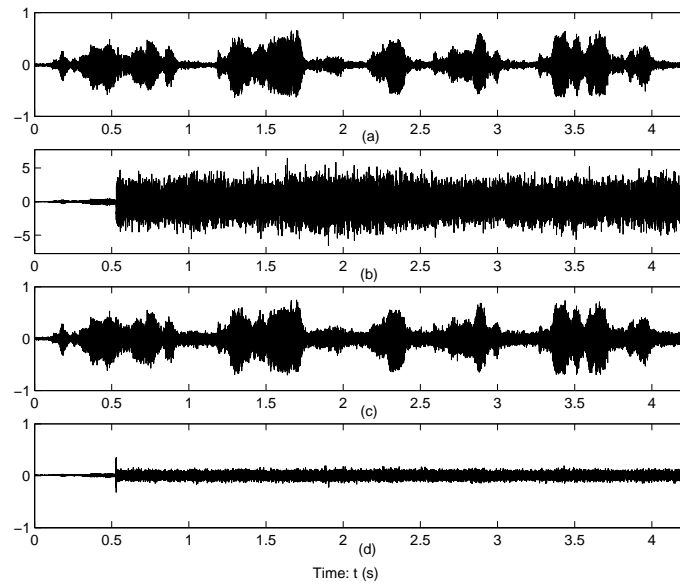
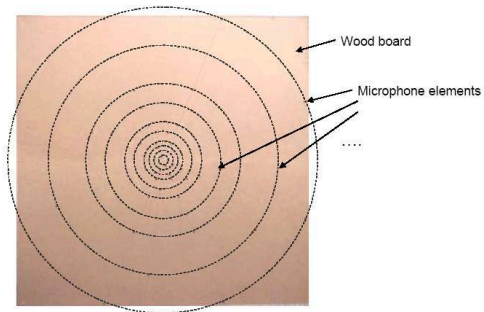
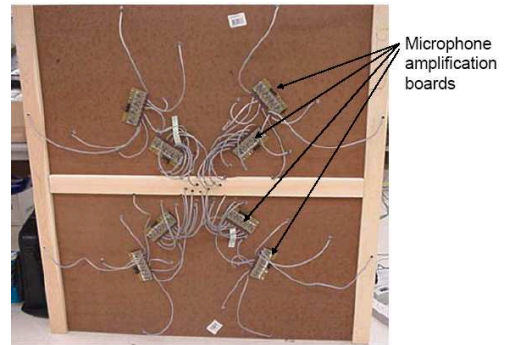


Figure 6.5: Processing results for scenario 2: (a) Desired signal $s(t)$; (b) Received noisy signal in one channel; (c) Beamformer output $z_1(t)$; (d) Error signal: $e_1(t) = z_1(t) - s(t)$.



(a) Front view.



(b) Rear view

Figure 6.6: Implemented microphone array.

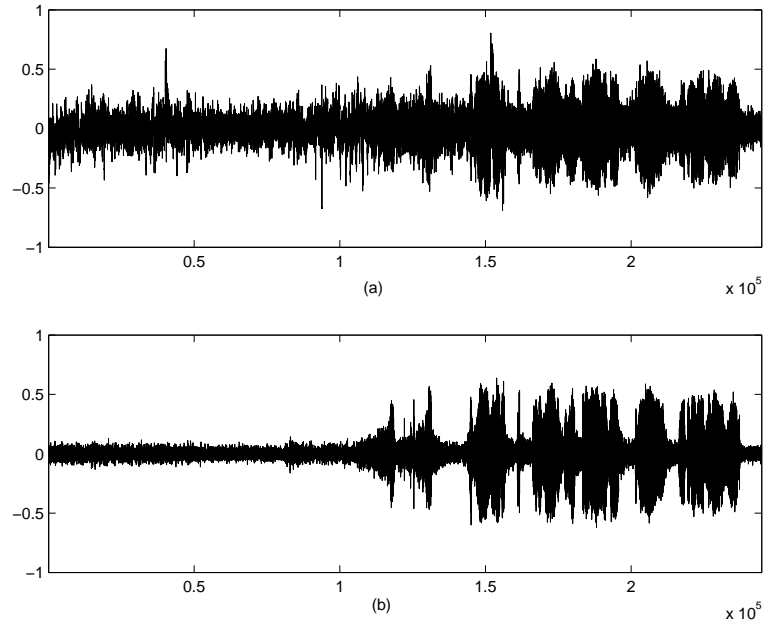


Figure 6.7: Processing results for the first set of field data: (a) Received noisy signal in one channel; (b) Beamformer output. Horizontal axis represents the number of samples.

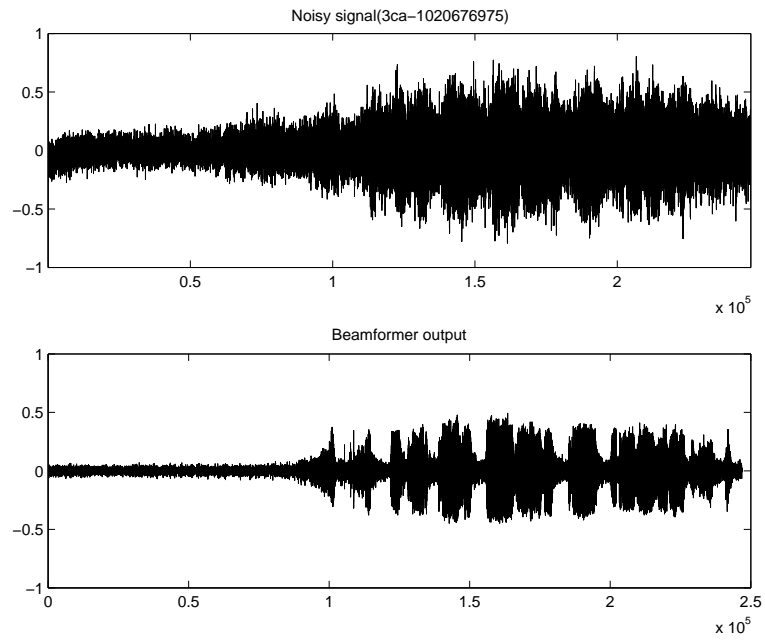


Figure 6.8: Processing results for the second set of field data: (a) Received noisy signal in one channel; (b) Beamformer output. Horizontal axis represents the number of samples.

Chapter 7

Conclusion and Future Work

In this chapter we first summarize the completed research work and then discuss the future research topics.

7.1 Completed Research

During my research study, I have investigated the problem of designing a broad-band beamformer using CRA. Three pattern synthesis methods for deterministic broad-band beamformer using the CRA have been proposed [95, 142, 143]. For beamforming in non-stationary signal environment, I have proposed a partially adaptive broad-band CRA [106, 144, 145]. The proposed deterministic design has been applied to bird monitoring applications and yielded encouraging results [97].

7.1.1 Deterministic CRA Design

Our proposed design of deterministic broad-band beamformer is based on Stearns and Stewart's work [33], in which they proposed a pattern synthesis method for continuous concentric ring antennas using Fourier-Bessel series expansion. However, their method is limited to 2-D narrow-band beamforming. We first generalize their method to 3-D beamforming and then propose a way to decompose the array weights into inter-ring

and intra-ring weights. Three methods are proposed to design the inter-ring weights to achieve desirable sidelobe level and/or mainlobe over a range of frequencies. Method I uses interpolation techniques to derive inter-ring weights at different frequencies to control the sidelobe level. In Method I, several approximations have been used which are valid if the number of array elements is sufficiently large; otherwise degradation is expected in the increase of sidelobe level. To alleviate the degradation, we propose Method II that optimizes the inter-ring weights using the MMSE criterion. Method II yields better sidelobe level control by taking the degradation due to insufficient array elements into an optimization process. Thirdly, we propose Method III that is able to achieve frequency invariant beampattern at a range of frequencies.

The frequency range that the proposed methods can be effectively applied is restricted by the array configuration, i.e., the array size, number of array elements and number of rings. A nested array design is adopted which can greatly expand the frequency range and make efficient use of array elements so that the total number of array elements can be kept to minimum.

The deterministic methods proposed above can achieve desired sidelobe level and/or mainlobe at arbitrary frequency within a given frequency range, thus broad-band beamformer based on FFT can be implemented very conveniently. To expand the scope of applications for the proposed deterministic designs, we have shown that our deterministic design can be incorporated into the Linear Constrained Minimum-Variance (LCMV) design using a method proposed by Griffiths and Buckley [88]. By doing so, nulls can be added in the beampattern to cancel strong interferences. We simulated various signal scenarios to test the performance of the proposed deterministic broad-band beamformer, the results confirm that our design is successful.

7.1.2 Adaptive CRA Design

Second, we look into developing the adaptive form of the CRA for applications in non-stationary signal environment. We first showed that if the array is implemented in fully adaptive manner, its computational complexity will be high and the convergence rate will be slow since the CRA usually consists of a large number of array elements.

To avoid these disadvantages, we propose the use of partially adaptive CRA. We first develop the generalized form of the partially adaptive CRA that accommodates arbitrary partitioning schemes. All the subarrays operate as deterministic beamformers using weights computed based on *a priori* knowledge of the desired signal's DOA. The adaptive processing is performed on the outputs from the subarrays, thus number of the weights is greatly reduced. We develop the partially adaptive CRA in the framework of Linear Constrained Minimum-Variance (LCMV) beamformer and its equivalent form – the General Sidelobe Canceller (GSC). The linear constraints applied to fully adaptive weighting vector are transformed to the partially adaptive weighting vector. We further show that our deterministic beamformer design can be incorporated into the LCMV or GSC design to improve the beamformer's quiescent beampattern by adding an additional linear constraint [88]. Two partially adaptive algorithms based on the LMS and RLS for the proposed partially adaptive CRA are also presented. Finally, we derive the theoretical formula of the steady state residual interference and noise power, which can serve as a criterion to evaluate different partitioning schemes.

In the simulations, we compare several typical partitioning schemes and compare their performance in terms of convergence rates and steady state residual interference and noise power. The proposed partially adaptive array yields very good performance as demonstrated by experiments. It is also shown that although the partially adaptive array may not achieve the global optimum solution in the steady state, the degradation in steady state performance is negligible.

7.1.3 Broadband DOA Estimation

The proposed deterministic and adaptive design method of CRA all assume the DOAs of the desirable signals are known. However, in practice, the DOAs are unknown and need to be estimated. To complete our research, we propose a broadband DOA estimation method for CRA.

Since the CRA usually contains a few dozens to hundreds of array elements, the computation required to perform signal subspace DOA estimation method in element space is very high. Our proposed method operates in beamspace to reduce computation. Furthermore, based on a broadband method by Lee [1], we use the frequency invariant deterministic design method proposed in Chapter 3 to design a broadband DOA estimator. In the proposed broadband DOA estimation method, the received array signals are first decomposed into narrowband components using FFT. At each frequency bin, the array signal is transformed to beamspace using a set of frequency invariant beamformers. The beamspace covariance matrices from different frequency bins are then calculated and coherently combined to form a single focused beamspace covariance matrix. Any narrowband DOA estimation technique can then be applied to the focused beamspace covariance matrix to yield DOA estimate. The CRLB of any unbiased DOA estimator using the CRA is also given to analyze the statistical performance of the proposed broadband DOA estimator.

Simulations confirm that the proposed broadband DOA estimator yields high estimation accuracy and greatly reduces computation compared to conventional incoherent estimation methods. In addition, the proposed method is able to resolve correlated sources when conventional incoherent estimation method fails.

7.1.4 Bird Monitoring Application

Collisions between aircraft and birds have become an increasing concern for human health and safety. We cooperated with US Air Force and Intelligent Automation, Incorporated in a bird monitoring project. The proposed deterministic CRA design has been used to enhance the performance of a bird monitoring system. Bird sounds in very noisy environment are picked up by a CRA using our proposed design, the received noisy signal is then processed using our beamforming algorithms. The improvement in output signal SNRs and bird sound classification score is corroborated by simulations and field data experiments.

7.2 Future Work

We plan to continue our research on CRA in these following topics:

- (1) Improve the range of the CRA beamforming

Long range beamforming aims to pick up weak signal in long distance. It is a very challenging problem in that with the increasing operation range of the beamformer the amount of interference and noise received are also greatly increased. Possible solution might be the developing of CRA with high directivity together with robust adaptive processing capability.

- (2) Improve the accuracy of direction finding

Although the proposed broadband DOA estimator in Chapter 5 achieves high accuracy, it still has some room for improvement as suggested by the CRLB, especially for the estimation accuracy of the elevation angle.

Bibliography

- [1] T.-S. Lee, “Efficient wideband source localization using beamforming invariance technique,” *IEEE Trans. Signal Processing*, vol. 42, no. 6, pp. 1376–1387, June 1994.
- [2] D. H. Johnson and D. E. Dudgeon, *Array signal processing: concepts and techniques*. Upper Saddle River, NJ: Prentice Hall, 1993.
- [3] E. Brookner, “Phased-array radar,” *Scientific American*, vol. 252, pp. 94–102, Feb. 1985.
- [4] S. Haykin, Ed., *Array Signal Processing*. Englewood Cliffs, NJ: Prentice-Hall, 1985.
- [5] D. C. Munson, J. D. O’Brian, and W. K. Jenkins, “A tomographic formulation of spot-light mode synthetic aperture radar,” *Proc. IEEE*, vol. 71, pp. 917–925, Aug. 1983.
- [6] W. C. Knight, R. Pridham, and S. M. Kay, “Digital signal processing for sonar,” *Proc. IEEE*, vol. 69, pp. 1451–1506, Nov. 1981.
- [7] N. L. Owsley, *Array Signal Processing*, S. Haykin, Ed. Englewood Cliffs, NJ: Prentice-Hall, 1985.
- [8] J. A. TenCate, T. G. Muir, and et al., “Beamforming on seismic interface waves with an array of geophones on the shallow sea floor,” *IEEE J. Oceanic Eng.*, vol. 20, no. 4, pp. 300–310, Oct. 1995.

- [9] H. M. Chouhan and G. V. Anand, "Bearing estimation of a sound source in a shallow water channel," in *Proc. TENCON '89. Fourth IEEE Region 10 Int. Conf.*, Nov. 1989, pp. 259–262.
- [10] B. Widrow, J. R. G. Jr., and et al., "Adaptive noise cancelling: principles and applications," *Proc. IEEE*, vol. 63, pp. 1692–1716, Dec. 1975.
- [11] W. Gee, S. Lee, and et al., "Focused array hyperthermia applicator: theory and experment," *IEEE Trans. Biomed. Eng.*, vol. BME-31, pp. 38–45, Jan. 1984.
- [12] P. M. Peterson, N. I. Durlach, and et al., "Multimicrophone adaptive beamforming for interference reduction in hearing aids," *Jour. of Rehab. R&D*, vol. 24, Fall 1987.
- [13] J. T. Mayhan, "Nulling limitations for a multiple-beam antenna," *IEEE Trans. Antennas Propagat.*, vol. 24, pp. 769–779, Nov. 1976.
- [14] R. T. C. Jr., "An adaptive array in a spread-spectrum communication system," *Proc. IEEE*, vol. 66, pp. 289–298, Mar. 1978.
- [15] J. H. Justice, *Array Signal Processing*, S. Haykin, Ed. Englewood Cliffs, NJ: Prentice-Hall, 1985.
- [16] A. C. Readhead, "Radio astronomy by very-long-baseline interferometry," *Scientific American*, vol. 246, pp. 52–61, June 1982.
- [17] J. L. Yen, *Array Signal Processing*, S. Haykin, Ed. Englewood Cliffs, NJ: Prentice-Hall, 1985.
- [18] A. Macovski, *Mdeical Imaging*. Englewood Cliffs, NJ: Prentice-Hall, 1983.
- [19] W. K. Pratt, *Digital Image Processing*. New York: Wiley and Sons, 1978.
- [20] A. C. Kak, *Array Signal Processing*, S. Haykin, Ed. Englewood Cliffs, NJ: Prentice-Hall, 1985.

- [21] W. Gabriel, "Adaptive circular arrays for communications systems," in *Proc. IEEE Antennas Propagat. Int. Symp. '75*, vol. 13, June 1975, pp. 289–292.
- [22] R. Bahl and P. Indiresan, "A novel beamformer for circular sonar arrays," in *Proc. IEEE ICASSP'81*, Apr. 1981, pp. 1050–1053.
- [23] Z. D. Qin, J. Ylitalo, and J. Oksman, "Circular-array ultrasound holography imaging using the linear-array approach," *IEEE Trans. Ultrason., Ferroelect., Freq. Contr.*, vol. 36, no. 5, pp. 485–493, Sept. 1989.
- [24] P. Fletcher and P. Darwood, "Beamforming for circular and semicircular array antennas for low-cost wireless lan data communications systems," *IEE Proc. Microwaves, Antennas and Propagat.*, vol. 145, no. 2, pp. 153–158, Apr. 1998.
- [25] Z. Jianhua, X. Hong, and Y. Jianping, "Analysis of the dipole circular array in interferometric direction-finding system," in *Proc. IEEE ISAPE'00*, Aug. 2000, pp. 255–260.
- [26] L. Bogdan and C. Comsa, "Analysis of circular arrays as smart antennas for cellular networks," in *Proc. IEEE Int. Symp. Signals, Circuits and Systems. '03*, vol. 2, July 2003, pp. 525–528.
- [27] H. Stenzel, *Elek. Nachrichtentech.*, vol. 6, pp. 165–181, 1929.
- [28] W. R. LePage, C. S. Roys, and S. Seeley, "Radiation from circular current sheets," *Proc. IRE*, vol. 38, pp. 1069–1072, Sept. 1950.
- [29] R. H. DuHamel, "Pattern synthesis for arrays on circular, elliptical, and spherical surfaces," *Univ. of Illinois, Urbana, Tech. Rept.*, no. 16, p. 43, May 1952.
- [30] H. L. Knudsen, "The field radiated by a ring quasi-array of an infinite number of tangential or radial dipoles," *Proc. IRE*, vol. 41, pp. 781–789, June 1953.

- [31] J. R. Wait and J. Householder, "Pattern synthesis for slotted cylinder antennas," *J. Res. Nat. Bur. Stand.*, vol. 63D, no. 3, pp. 303–313, Nov-Dec. 1959.
- [32] H. P. Neff and J. D. Tillman, "An electronically scanned circular antenna array," *IRE Internat'l Conv. Rec.*, no. 8, pp. 41–47, 1960.
- [33] C. O. Stearns and A. C. Stewart, "An investigation of concentric ring antennas with low sidelobes," *IEEE Trans. Antennas Propagat.*, vol. AP-13, no. 6, pp. 856–863, Nov. 1965.
- [34] N. Goto and D. K. Cheng, "On the synthesis of concentric-ring arrays," *Proc. IEEE*, vol. 58, p. 839, May 1970.
- [35] T. Taylor, "Design of circular apertures for narrow beamwidth and low sidelobes," *IEEE Trans. Antennas Propagat.*, vol. AP-8, no. 1, pp. 17–22, Jan. 1960.
- [36] T. B. Vu, "Side-lobe control in circular ring array," *IEEE Trans. Antennas Propagat.*, vol. 41, no. 8, pp. 1143–1145, Aug. 1993.
- [37] T.-S. Chu, "On the use of uniform circular arrays to obtain omnidirectional patterns," *IEEE Trans. Antennas Propagat.*, vol. AP-9, pp. 436–438, Oct. 1959.
- [38] D. Sinnott and R. Harrington, "Analysis and design of circular antenna arrays by matrix methods," *IEEE Trans. Antennas Propagat.*, vol. 21, no. 5, pp. 610–614, Sept. 1973.
- [39] F. Tseng and D. Cheng, "Pattern synthesis of circular arrays with many directive elements," *IEEE Trans. Antennas Propagat.*, vol. AP-16, no. 6, pp. 758–759, Nov. 1968.
- [40] J. Blass, "An analysis of the radiation from circular arrays of directive elements," *IEEE Trans. Antennas Propagat.*, vol. 22, no. 1, pp. 84–87, Jan. 1974.

- [41] T. Taylor, "A synthesis method for circular and cylindrical antennas composed of discrete elements," *IRE Trans. on Antennas and Propogat.*, vol. 3, no. 1, pp. 251–261, Aug. 1952.
- [42] T. L. Simpson and J. D. Tillmann, "Parasitic excitation of circular antenna arrays," *IRE Trans. Antennas Propagation*, vol. AP-9, pp. 263–267, May 1961.
- [43] S. W. Lee and Y. T. Lo, "On the pattern function of circular arc arrays," *IEEE Trans. Antennas Propagat.*, vol. AP-13, no. 4, pp. 649–650, July 1965.
- [44] T. Lo and H. Hsuan, "An equivalence theory between elliptical and circular arrays," *IEEE Trans. Antennas Propagat.*, vol. AP-13, no. 2, pp. 247–256, Mar. 1965.
- [45] F. Tseng and D. Cheng, "Pattern synthesis of circular arrays in a moving medium," *IEEE Trans. Antennas Propagat.*, vol. AP-17, no. 4, pp. 524–526, July 1969.
- [46] D. Cheng and F. Tseng, "Pencil-beam synthesis for large circular arrays," in *Proc. IEEE Antennas Propagat. Int. Symp. '69*, vol. 7, Dec. 1969, pp. 26–28.
- [47] F. Ares, S. R. Rengarajan, J. A. Ferreira, and A. Trastoy, "Synthesis of antenna patterns of circular arc arrays," in *Proc. IEEE Antennas Propagat. Int. Symp. '97*, July 1997, pp. 2248–2251.
- [48] N. Goto and Y. Tsunoda, "Sidelobe reduction of circular array with a constant excitaion amplitude," *IEEE Trans. Antennas Propagat.*, vol. AP-25, no. 6, pp. 896–898, Nov. 1977.
- [49] D. K. Cheng, "Optimization techniques for antenna arrays," *Proc. IEEE*, vol. 59, p. 1664, 1971.

- [50] F. Watanabe and N. Goto, "A synthesis of circular arrays by taking account of the excitation circuit," in *Proc. IEEE Antennas Propagat. Int. Symp.*'79, vol. 17, June 1979, pp. 42–45.
- [51] F. Watanabe, N. Goto, A. Nagayama, and G. Yoshida, "A pattern synthesis of circular arrays by phase adjustment," *IEEE Trans. Antennas Propagat.*, vol. AP-28, no. 6, pp. 857–863, Nov. 1980.
- [52] H. Coleman, "An iterative technique for reducing sidelobes of circular arrays," *IEEE Trans. Antennas Propagat.*, vol. 18, no. 4, pp. 566–567, July 1970.
- [53] S. Prasad and R. Charan, "On the constrained synthesis of array patterns with applications to circular and arc array," *IEEE Trans. Antennas Propagat.*, vol. AP-32, no. 7, pp. 725–730, July 1984.
- [54] R. Vescovo, "Constrained and unconstrained synthesis of array factor for circular arrays," *IEEE Trans. Antennas Propagat.*, vol. 43, no. 12, pp. 1405–1410, Dec. 1995.
- [55] —, "Pattern synthesis with assigned field reduction in near-field for circular arrays," in *Proc. IEEE Antennas Propagat. Int. Symp.*'02, vol. 1, June 2002, pp. 540–543.
- [56] B. P. Kumar and G. R. Branner, "Design of low sidelobe circular ring array by element radius optimization," in *Proc. IEEE Antennas Propagat. Int. Symp.*'99, Orland, USA, July 1999, pp. 2032–2035.
- [57] B. K. Lau and Y. H. Leung, "A Dolph-Chebyshev approach to the synthesis of array patterns for uniform circular arrays," in *Proc. IEEE ISCAS'00*, Geneva, Switzerland, May 2000, pp. I124 – I127.

- [58] D. E. N. Davies, "A transformation between the phasing techniques required for linear and circular aerial arrays," *Proc. IEE*, vol. 112(11), pp. 2041–2045, 1965.
- [59] S. C. Chan and C. K. S. Pun, "On the design of digital broadband beamformer for uniform circular array with frequency invariant characteristics," in *Proc. IEEE ISCAS'02*, vol. 1, Arizona, USA, May 2002, pp. I-693 – I-696.
- [60] Chan, "Tba," in *Proc. IEEE ICASSP'05*, Philadelphia, USA, Mar. 2005.
- [61] T. Sarkar and R. Adve, "Space-time adaptive processing using circular arrays," *IEEE Antennas Propagat. Mag.*, vol. 43, no. 1, pp. 138–143, Feb. 2001.
- [62] I. Jouny, "Beamspace STAP for circular arrays," in *Proc. IEEE Antennas Propagat. Int. Symp. '99*, Orland, USA, July 1999, pp. 784–787.
- [63] M. Zatman, "Circular array STAP," *IEEE Trans. Aerosp. Electron. Syst.*, vol. 36, no. 2, pp. 510–517, Apr. 2000.
- [64] H. N. Nguyen, J. D. Hiemstra, and J. S. Goldstein, "The reduced rank multistage wiener filter for circular array STAP," in *Proc. IEEE conf. Radar'03*, May 2003, pp. 66–70.
- [65] K. L. Virga and H. Zhang, "Spatial beamformer weighting sets for circular array STAP," in *Proc. IEEE Int. Conf. on Phased Array Sys. and Tech. '00*, May 2000, pp. 561–564.
- [66] B. Friedlander, "The MVDR beamformer for circular arrays," in *Proc. Conf. Record of the 34th Asilomar Conf. on Signals, Systems and Computers. '00*, Oct. 2000, pp. 25–29.
- [67] J. Coffey, "The effect of multipath on adaptive nulling in a circular array," in *Proc. IEEE Antennas Propagat. Int. Symp. '86*, vol. 24, June 1986, pp. 961–964.

- [68] R. Vescovo, "Phase-only null control for circular arrays," in *Proc. IEEE Antennas Propagat. Int. Symp. '96*, July 1996, pp. 818–821.
- [69] ———, "Pattern synthesis with null constraints for circular arrays of equally spaced isotropic elements," *IEE Proc. Microwaves, Antennas and Propagat.*, vol. 143, no. 2, pp. 103–106, Apr. 1996.
- [70] J. A. Hejres and J. E. Richie, "A simple method for null steering in a circular array by perturbations of the radial locations of the elements," in *Proc. IEEE Antennas Propagat. Int. Symp. '96*, July 1996, pp. 1138–1141.
- [71] J. Abele, J. Joubert, and J. W. Odendaal, "Introduction of multiple nulls in otherwise omnidirectional pattern of circular dipole array," *IEEE Electro. Lett.*, vol. 34, no. 14, pp. 1371–1373, July 1998.
- [72] D. G. Manolakis, V. K. Ingle, and S. M. Kogon, *Statistical and Adaptive Signal Processing*. Boston: McGraw-Hill, 2000.
- [73] L. J. Griffiths, "An alternative approach to linearly constrained adaptive beamforming," *IEEE Trans. Antennas Propagat.*, vol. 30, no. 1, pp. 27–34, Jan. 1982.
- [74] B. D. V. Veen and K. M. Buckley, "Beamforming: A versatile approach to spatial filtering," *IEEE ASSP Mag.*, vol. 5, pp. 4–24, Apr. 1988.
- [75] J.-L. Yu and C.-C. Yeh, "Generalized eigenspace-based beamformers," *IEEE Trans. Signal Processing*, vol. 43, no. 11, pp. 2453–2461, Nov. 1995.
- [76] F. Asano, S. Hayamizu, T. Yamada, and S. Nakamura, "Speech enhancement based on the subspace method," *IEEE Trans. Speech Audio Processing*, vol. 8, no. 5, pp. 497–507, Sept. 2000.

- [77] S. Doclo and M. Moonen, "GSVD-based optimal filtering for single and multi-microphone speech enhancement," *IEEE Trans. Signal Processing*, vol. 50, no. 9, pp. 2230–2244, Sept. 2002.
- [78] F. Jabloun and B. Champagne, "A perceptual signal subspace approach for speech enhancement in colored noise," in *Proc. IEEE ICASSP'02*, May 2002, pp. I569–I572.
- [79] H. Unz, "Linear arrays with arbitrary distributed elements," *IEEE Trans. Antennas Propagat.*, vol. AP-8, pp. 222–223, Mar. 1960.
- [80] M. G. Andreasan, "Linear arrays with variable interelement spacings," *IEEE Trans. Antennas Propagat.*, vol. AP-10, pp. 137–143, Mar. 1962.
- [81] B. P. Kumar and G. R. Branner, "Design of unequally spaced arrays for performance improvement," *IEEE Trans. Antennas Propagat.*, vol. 47, no. 3, pp. 511–523, Mar. 1999.
- [82] Y. Hua, T. K. Sarkar, and D. D. Weiner, "An L-shaped array for estimating 2-d directions of wave arrival," *IEEE Trans. Antennas Propagat.*, vol. 39, no. 2, pp. 143–146, Feb. 1991.
- [83] S. Horiguchi, T. Ishizone, and Y. Mushiake, "Radiation characteristics of spherical triangular array antenna," *IEEE Trans. Antennas Propagat.*, vol. 33, no. 4, pp. 472–476, Apr. 1985.
- [84] S. Yu and J. Lee, "Design of two-dimensional rectangular array beamformers with partial adaptivity," *IEEE Trans. Antennas Propagat.*, vol. 45, no. 1, pp. 157–167, Jan. 1997.
- [85] A. Manikas, A. Sleiman, and I. Dacos, "Manifold studies of nonlinear antenna

- array geometries,” *IEEE Trans. Signal Processing*, vol. 49, no. 3, pp. 497–506, Mar. 2001.
- [86] R. Kronberger, A. Stephan, and M. Daginnus, “3D antenna measurement and electromagnetic simulation for advanced vehicle antenna development,” in *Proc. IEEE Antennas Propagat. Int. Symp. ’01*, vol. 3, July 2001, pp. 342–345.
- [87] R. E. Collin and F. J. Zucker, *Antenna Theory: Part I*. New York: McGraw-Hill, 1969.
- [88] L. J. Griffiths and K. M. Buckley, “Quiescent pattern control in linearly constrained adaptive arrays,” *IEEE Trans. Acoust., Speech, Signal Processing*, vol. 35, no. 7, pp. 917–926, July 1987.
- [89] D. B. Ward, Z. Ding, and R. A. Kennedy, “Broadband DOA estimation using frequency invariant beamforming,” *IEEE Trans. Signal Processing*, vol. 46, no. 5, pp. 1463–1469, May 1998.
- [90] D. B. Ward and T. D. Abhayapala, “Range and bearing estimation of wideband sources using an orthogonal beamspace processing structure,” in *Proc. IEEE ICASSP’04*, Montreal, Quebec, Canada, May 2004, pp. II 109 – II 112.
- [91] K. Nishikawa, T. Yamamoto, K. Oto, and T. Kanamori, “Wideband beamforming using fan filter,” in *Proc. IEEE ISCAS’92*, May 1992, pp. 533 – 536.
- [92] D. B. Ward, R. A. Kennedy, and R. C. Williamson, “FIR filter design for frequency invariant beamformers,” *IEEE Signal Processing Lett.*, vol. 3, no. 3, pp. 69–71, Mar. 1996.
- [93] T. Sekiguchi and Y. Karasawa, “Wideband beamspace adaptive array utilizing FIR fan filters for multibeam forming,” *IEEE Trans. Signal Processing*, vol. 48, no. 1, pp. 277–284, Jan. 2000.

- [94] D. B. Ward, R. A. Kennedy, and R. C. Williamson, "Theory and design of broadband sensor arrays with frequency invariant far-field beam patterns," *J. Acoust. Soc. Amer.*, vol. 97, no. 2, pp. 1023–1034, Feb. 1995.
- [95] Y. Li, K. C. Ho, and C. Kwan, "Design of broad-band circular ring microphone array for speech acquisition in 3-D," in *Proc. IEEE ICASSP'03*, Hongkong, China, Apr. 2003, pp. 221–224.
- [96] Y. M. C. Marro and K. U. Simmer, "Analysis of noise reduction and dereverberation techniques based on microphone arrays with postfiltering," *IEEE Trans. Speech Audio Proc.*, vol. 6, no. 3, pp. 240–259, May 1998.
- [97] C. Kwan *et al.*, "An automated acoustic system to monitor and classify birds," in *Proc. Bird Monitoring Workshop'03*, Toronto, Canada, Aug. 2003.
- [98] D. R. Morgan, "Partially adaptive array techniques," *IEEE Trans. Antennas Propagat.*, vol. 26, pp. 823–833, Nov. 1978.
- [99] D. J. Chapman, "Partial adaptivity for the large arrays," *IEEE Trans. Antennas Propagat.*, vol. 24, pp. 685–696, Sept. 1976.
- [100] A. M. Vural, "A comparative performance study of adaptive array processors," in *Proc. IEEE ICASSP'77*, Apr. 1977, pp. 695–700.
- [101] R. N. Adams, L. L. Horowitz, and K. D. Senne, "Adaptive main-beam nulling for narrow-beam antenna arrays," *IEEE Trans. Aerosp. Electron. Syst.*, vol. 16, pp. 509–516, July 1980.
- [102] W. F. Gabriel, "Using spectral estimation techniques in adaptive array processing," *IEEE Trans. Antennas Propagat.*, vol. 34, pp. 291–300, Mar. 1986.

- [103] B. D. V. Veen and R. A. Roberts, "Partially adaptive beamformer design via output power minimization," *IEEE Trans. Acoust., Speech, Signal Processing*, vol. 35, pp. 1534–1532, Nov. 1987.
- [104] M. Rupp, "The behavior of LMS and NLMS algorithms in the presence of spherically invariant processes," *IEEE Trans. Signal Processing*, vol. 41, pp. 1149 – 1160, Mar. 1993.
- [105] B. D. V. Veen, "Minimum variance beamforming," in *Adaptive Radar Detection and Estimation*, S. Haykin and A. Steinhardt, Eds. New York: John Wiley & Sons, 1992.
- [106] Y. Li, K. C. Ho, and C. Kwan, "A novel partial adaptive broad-band beamformer using concentric ring array," in *Proc. IEEE ICASSP'04*, Montreal, Quebec, Canada, May 2004, pp. II 177 – II 180.
- [107] H. Krim and M. Viberg, "Two decades of array signal processing research: the parametric approach," *IEEE Signal Processing Mag.*, vol. 13, no. 4, pp. 67–94, July 1996.
- [108] G. Bienvenu and L. Kopp, "Optimality of high resolution array processing using the eigensystem approach," *IEEE Trans. Acoust., Speech, Signal Processing*, vol. 31, pp. 1235–1248, Oct. 1983.
- [109] R. Schmidt, "Multiple emitter location and signal parameter estimation," *IEEE Trans. Antennas Propagat.*, vol. 34, pp. 276–280, Mar. 1986.
- [110] R. Roy and T. Kailath, "ESPRIT-estimation of signal parameters via rotational invariance techniques," *IEEE Trans. Acoust., Speech, Signal Processing*, vol. 37, no. 7, pp. 984–995, July 1989.

- [111] F. C. Robey, D. Fuhrmann, E. J. Kelly, and R. Nitzberg, "A CFAR adaptive matched filter detector," *IEEE Trans. Aerosp. Electron. Syst.*, vol. 28, pp. 208 – 216, Jan. 1992.
- [112] E. Baranoski and J. Ward, "Source localization using adaptive subspace beamformer outputs," in *Proc. IEEE ICASSP'97*, Apr. 1997, pp. 3773 – 3776.
- [113] M. A. Doron and A. J. Weiss, "On focusing matrices for wide-band array processing," *IEEE Trans. Signal Processing*, vol. 40, no. 6, pp. 1295–1302, June 1992.
- [114] H. Wang and M. Kaveh, "Coherent signal-subspace processing for the detection and estimation of angles of arrival of multiple wide-band sources," *IEEE Trans. Acoust., Speech, Signal Processing*, vol. 33, no. 4, pp. 823–831, Aug. 1985.
- [115] H. Hung and M. Kaveh, "Focussing matrices for coherent signal-subspace processing," *IEEE Trans. Acoust., Speech, Signal Processing*, vol. 36, no. 8, pp. 1272–1281, Aug. 1988.
- [116] K. M. Buckley and L. J. Griffiths, "Broad-band signal-subspace spatial-spectrum (BASS-ALE) estimation," *IEEE Trans. Acoust., Speech, Signal Processing*, vol. 36, no. 7, pp. 953–964, July 1988.
- [117] A. H. Tewfik and W. Hong, "On the application of uniform linear array bearing estimation techniques to uniform circular arrays," *IEEE Trans. Signal Processing*, vol. 40, no. 4, pp. 1008–1011, Apr. 1992.
- [118] B. Friedlander and A. J. Weiss, "Direction finding using spatial smoothing with interpolated arrays," *IEEE Trans. Aerosp. Electron. Syst.*, vol. 28, no. 2, pp. 574–587, Apr. 1992.
- [119] A. Swindlehurst, "DOA identifiability for rotationally invariant arrays," *IEEE Trans. Signal Processing*, vol. 40, no. 7, pp. 1825–1828, July 1992.

- [120] B. K. Lau *et al.*, “Direction of arrival estimation in the presence of correlated signals and array imperfections with uniform circular arrays,” in *Proc. IEEE ICASSP’02*, May 2002, pp. III 3037 – III 3040.
- [121] C. P. Mathews and M. D. Zoltowski, “Eigenstructure techniques for 2-D angle estimation with uniform circular arrays,” *IEEE Trans. Signal Processing*, vol. 42, no. 9, pp. 2395–2407, Sept. 1994.
- [122] ———, “Performance analysis of the UCA-ESPRIT algorithm for circular ring arrays,” *IEEE Trans. Signal Processing*, vol. 42, no. 9, pp. 2535–2539, Sept. 1994.
- [123] J.-J. Fuchs, “On the application of the global matched filter to DOA estimation with uniform circular arrays,” *IEEE Trans. Signal Processing*, vol. 49, no. 4, pp. 702–709, Apr. 2001.
- [124] M. Wax and J. Sheinvald, “Direction finding of coherent signals via spatial smoothing for uniform circular arrays,” *IEEE Trans. Antennas Propagat.*, vol. 42, no. 5, pp. 613–620, May 1994.
- [125] M. He, Y. Yin, and X. Zhang, “UCA-ESPRIT algorithm for 2-D angle estimation,” in *Proc. WCCC-ICSP’00*, vol. 1, Aug. 2000, pp. 437–440.
- [126] A. Y. J. Chan and J. Litva, “High-resolution two-dimensional direction finding for uniform circular array,” in *Proc. IEEE Seventh SP Workshop on Statistical Signal and Array Processing 94’*, June 1994, pp. 149–152.
- [127] ———, “MUSIC and maximum likelihood techniques on two-dimensional DOA estimation with uniform circular array,” *IEE Proc. Radar, Sonar and Navigation*, vol. 142, no. 3, pp. 105–114, June 1995.
- [128] J. Krolik and D. Swingler, “Multiple broad-band source location using steered

- covariance matrices,” *IEEE Trans. Acoust., Speech, Signal Processing*, vol. 37, no. 10, pp. 1481–1494, Oct. 1989.
- [129] X. L. Xu and K. M. Buckley, “Maximum likelihood and least-squares broadband source localization in beam-space,” in *Proc. Twenty-Second Asilomar Conference on Signals, Systems and Computers '88*, Oct. 1988, pp. 593–597.
- [130] H. B. Lee and M. S. Wengrovitz, “Resolution threshold of beamspace MUSIC for two closely spaced emitters,” *IEEE Trans. Acoust., Speech, Signal Processing*, vol. 38, no. 9, pp. 1545–1559, Sept. 1990.
- [131] T. Do-Hong, F. Demmel, and P. Russer, “Wideband direction-of-arrival estimation using frequency-domain frequency-invariant beamformers: an analysis of performance,” *IEEE Microwave Wireless Compon. Lett.*, vol. 14, no. 8, pp. 383–385, Aug. 2004.
- [132] P. Stoica and N. Arye, “MUSIC, maximum likelihood, and Cramer-Rao bound,” *IEEE Trans. Acoust., Speech, Signal Processing*, vol. 37, no. 5, pp. 720–741, May 1989.
- [133] —, “MUSIC, maximum likelihood, and Cramer-Rao bound: further results and comparisons,” *IEEE Trans. Acoust., Speech, Signal Processing*, vol. 38, no. 12, pp. 2140–2150, Dec. 1990.
- [134] U. Baysal and R. L. Moses, “On the geometry of isotropic arrays,” *IEEE Trans. Signal Processing*, vol. 51, no. 6, pp. 1469–1478, June 2003.
- [135] Y. Hua and T. K. Sarkar, “A note on the Cramer-Rao bound for 2-D direction finding based on 2-D array,” *IEEE Trans. Signal Processing*, vol. 39, no. 5, pp. 1215–1218, May 1991.

- [136] A. N. Mirkin and L. H. Sibul, “Cramer-Rao bounds on angle estimation with a two-dimensional array,” *IEEE Trans. Signal Processing*, vol. 39, no. 2, pp. 515–517, Feb. 1991.
- [137] M. Zatman, “Properties and applications of wideband Cramer-Rao bounds,” in *Proc. Ninth IEEE SP Workshop on Statistical Signal and Array Processing*, Sept. 1998, pp. 41–44.
- [138] L. Yip *et al.*, “Cramer-Rao bound analysis of wideband source localization and DOA estimation,” in *Proc. SPIE*, vol. 4791, 2002, pp. 304–316.
- [139] S. M. Kay, *Fundamentals of statistical signal processing: Estimation theory*. New Jersey: Prentice Hall International Inc, 1993.
- [140] Bird Strike Committee USA. (2004, Mar.) An overview of the bird threat to aircraft. [Online]. Available: <http://www.birdstrike.org/risk/threat.htm>
- [141] C. Kwan, K. C. Ho, and *et al.*, “Phase 1 progress report 3 to the air force,” Intelligent Automation, Incorporated and the University of Missouri at Columbia, Tech. Rep., Apr. 2003.
- [142] Y. Li, K. C. Ho, and C. Kwan, “Beampattern synthesis for concentric circular ring array using MMSE design,” in *Proc. IEEE ISCAS'04*, Vancouver, Canada, May 2004, pp. III 329 – III 332.
- [143] —, “3-D array pattern synthesis with frequency invariant property for concentric ring array,” *IEEE Trans. Signal Processing*, to be published.
- [144] —, “Generalized partially adaptive concentric ring array,” in *Proc. IEEE ISCAS'05*, Kobe, Japan, May 2005.
- [145] Y. Li, K. C. Ho, C. Kwan, and Y. H. Leung, “A study of partially adaptive concentric ring array,” *IEEE Trans. Circuits Syst. II*, submitted for publication.

VITA

Yunhong Li received his BS and MS degree in Electrical Engineering at the Huazhong University of Science and Technology, China in 1997 and 2000 respectively. He then came to the University of Missouri-Columbia to pursue Ph.D. degree in Electrical Engineering and will receive it in 2005.